(12)

AFGL-TR-87-0229

Lg WAVE EXCITATION AND PROPAGATION IN THE PRESENCE OF ONE-, TWO-, and THREE-DIMENSIONAL HETEROGENEITIES

R. B. HERRMANN

SAINT LOUIS UNIVERSITY
221 NORTH GRAND BOULEVARD
ST. LOUIS, MO 63103

15 July 1987

Final Report

1 April 1985 - 31 - March 1987

APPROVED FOR PUBLIC RELEASE; DISTRIBUTION UNLIMITED

AIR FORCE GEOPHYSICS LABORATORY
AIR FORCE SYSTEMS COMMAND
UNITED STATES AIR FORCE
HANSCOM AIR FORCE BASE, MASSACHUSETTS 01731

Unclassified
SECURITY CLASSIFICATION OF THIS PAGE

AD A187 364

REPORT DOCUMENTATION PAGE

1a. REPORT SECURITY CLASSIFICATION unclassified	1b. RESTRICTIVE MARKINGS
2a. SECURITY CLASSIFICATION AUTHORITY	3. DISTRIBUTION/AVAILABILITY OF REPORT Approved for public release; distribution unlimited
2b. DECLASSIFICATION/DOWNGRADING SCHEDULE	
4. PERFORMING ORGANIZATION REPORT NUMBER(S)	5. MONITORING ORGANIZATION REPORT NUMBER(S) AFGL-TR-87-0229
6a. NAME OF PERFORMING ORGANIZATION Saint Louis University	6b. OFFICE SYMBOL (If applicable)
7a. NAME OF MONITORING ORGANIZATION Air Force Geophysics Laboratory	
6c. ADDRESS (City, State and ZIP Code) 221 North Grand Blvd. St. Louis, MO 63103	7b. ADDRESS (City, State and ZIP Code) Hanscon Air Force Base, MA 01731
8a. NAME OF FUNDING/SPONSORING ORGANIZATION DARPA/DSO	8b. OFFICE SYMBOL (If applicable)
9. PROCUREMENT INSTRUMENT IDENTIFICATION NUMBER F19628-85-K-0029	
8c. ADDRESS (City, State and ZIP Code) 1400 Wilson Blvd. Arlington, VA 22209	

10. SOURCE OF FUNDING NOS.

PROGRAM ELEMENT NO.	PROJECT NO.	TASK NO.	WORK UNIT NO.
61101F	5A10	DA	A0

11. TITLE (Include Security Classification)
Lg Wave Excitation and Propagation (over)

12. PERSONAL AUTHOR(S)
R. B. Herrmann

13a. TYPE OF REPORT	13b. TIME COVERED	14. DATE OF REPORT (Yr., Mo., Day)	15. PAGE COUNT
Final Report	FROM 1 APR 85 TO 31 MAR 87	87 JUL 15	82

16. SUPPLEMENTARY NOTATION

17. COSATI CODES

FIELD	GROUP	SUB. GR.

18. SUBJECT TERMS (Continue on reverse if necessary and identify by block number)
Lg wave scattering, Phase matched surface-wave filters.

19. ABSTRACT (Continue on reverse if necessary and identify by block number)

The scattering of Lg waves by point heterogeneities in a crustal waveguide is considered. Computer simulations lead to inferences of the behavior of the scattering mechanism which helps understand observed facts about the shear wave coda, especially the relationship between the lag time at which measurements are made and the inferred coda Q.

A second study reports on problems in some routine processing techniques used for long period surface wave analysis. The influence of spectral shape on inferred spectral amplitudes is discussed. (Keywords:)

20. DISTRIBUTION/AVAILABILITY OF ABSTRACT
UNCLASSIFIED/UNLIMITED ☐ SAME AS RPT. ☐ DTIC USERS ☐

21. ABSTRACT SECURITY CLASSIFICATION
Unclassified

22a. NAME OF RESPONSIBLE INDIVIDUAL	22b. TELEPHONE NUMBER (Include Area Code)	22c. OFFICE SYMBOL
James F. Lewkowicz	(617) 377-3028	AFGL/LWH

DD FORM 1473, 83 APR EDITION OF 1 JAN 73 IS OBSOLETE.

unclassified
SECURITY CLASSIFICATION OF THIS PAGE

Cont of Block 11:

in the Presence of One-, Two-, and Three-Dimensional Heterogeneities

Table of Contents

INTRODUCTION 1

Synthesis of coda waves in layered medium 2

Application of frequency variable filters to surface-wave amplitude analysis 41

FINAL TECHNICAL REPORT

Lg Wave Excitation and Propagation in the Presence of One-, Two- and Three-Dimensional Heterogeneities

INTRODUCTION

This is the final technical report for this contract. Work has been directed both toward understanding seismic wave propagation in the presence of simple point heterogeneities in the medium and also toward the important validation of computational techniques used in analysis and synthesis of time histories. The research performed has been submitted for publication. Two papers have already been published. The papers in this report have been submitted for publication. The paper by Wang and Herrmann has been submitted to *PAGEOPH* for a special volume on scattering and Q edited by Aki and Wu. The paper by Russell, Herrmann and Hwang has been accepted by the *Bulletin, Seismological Society of America*.

PAPERS COMPLETED UNDER THIS CONTRACT

Shin, T.-C. and R. B. Herrmann (1987). Lg attenuation and source studies using 1982 Miramichi data, *Bull. Seism. Soc. Am.* **77**, 384-397.

Herrmann, R. B. and B. Mandal (1986). A study of wavenumber integration techniques, *Earthquake Notes* **57**, 33-40.

Wang, C.-Y. and R B. Herrmann (1987). Synthesis of coda waves in layered medium, *PAGEOPH* (in review).

Russell, D. R., R. B. Herrmann and H.-J. Hwang (1988). Application of frequency variable filters to surface-wave amplitude analysis, *Bull. Seism. Soc. Am.* **78**, (in press).

Synthesis of Coda Waves in Layered Medium

Chien-Ying Wang,[1] and Robert B. Herrmann[2]

[1]National Central University, Department of Geophysics, Chung-Li, Taiwan, Taiwan

[1]Department of Earth and Atmospheric. Sciences, Saint Louis University, PO Box 8099, St. Louis, Missouri 63156, USA

Abstract - Malin's (1980) first-order single scattering theory has been extended to study the scattering of surface waves as well as body waves by distributed point scatterers in a layered medium. The scattered waveform itself is generated and examined instead of its energy envelope. The theory used allows 1) mode conversion 2) wave type conversion 3) finite scatterer distribution, and 4) the effect of attenuation from scattering as well as intrinsic absorption. The cases studied are for elastic or slightly attenuative media with any kind of source and receiver at any place in the layered structure. This direct calculation of coda waves provides us an immediate description of the relation of coda and scattering. The objectives are to find 1) the effect of layering on scattering, 2) the effect of scatterer distribution on recorded vertical and horizontal motion, 3) the relation of scattering Q to intrinsic Q, 4) the scattering behavior of surface and body waves, and 5) the superposition of scattering waves to form the coda. The generation of body waves by 'locked mode' approximation, which makes the body-wave scattering a subset of the 'surface-wave', scattering. Preliminary results explain some observed coda behavior surprisingly well. We find a larger geometrical spreading for near scatterers, which is caused by mode conversion or wavetype conversion because of the wide angle scattering. This makes the spreading correction higher for early part of coda which may account for the low Q observed in early coda of regional earthquakes. This study is of practical value as an effort to understand the complicated coda phases.

Key words: Surface waves, scattering, layered media

1. Introduction

Because of recent interest in the extraction of useful information from the coda, a theoretical study of coda waves is urgently required, especially since the theory lags behind observations. Most of current coda analyzes are based on Aki's (1969) backscattering model. This model treats the coda as a smoothly decaying envelope which is formed by many randomly scattered waves. Since the scattered wave is the result of an averaging process for waves reacting with randomly distributed scatterers, most theories take a stochastic approach and describe the total wavefield by several statistical quantities. Mean power spectral density is frequently used, for instance (Aki, 1969; Sato, 1977). Using such an approach, the analysis of data provides a gross description of the distributed inhomogeneities and the scattering process, but some ambiguities arise. The problem of distinguishing between scattering Q and intrinsic Q is a typical example (Aki, 1982; Dainty, 1984). For our study, we choose a deterministic approach to investigate the effect of scattering on the generation of coda. We will directly examine each individual scattered pulse generated in the layered medium.

Sato (1984) proposed a scattering model which describes on the scatterers. A similar model is also found in Wu and Aki (1985). This model considers wave type conversion, scattering pattern, and scatterer size, but only for body waves in a homogeneous whole space. From another view point, Malin (1980) constructed a scattering model using surface wave normal mode theory. An important feature of this model is that it is able to handle multi-layered medium. The rays scattered by the inhomogeneities in a layered structure, such as the earth's crust, are numerous. It is only by using mode theory that scattering in such a medium can be treated.

In this study, we extend Malin's first-order single scattering model to create the scattering 'pulse' from scatterers situated in the layered structure. A simple review of this method is provided with the derivation largely simplified. Each individual scattered wave is examined in detail rather than its statistical average. The study is directed toward understanding the nature of the scattered waves under different conditions. This enables us to analyze the behavior of each scatterer, and hence makes it easier to isolate important factors which may be lost in an averaging process.

2. First-Order Single Scattering Theory

The model considered is a layered medium (Fig. 1) with inhomogeneities distributed at some restricted regions in it. The inhomogeneous region is assumed to be small compared to the wavelength. We call it a scatterer parcel. If the parcel is not small enough to be thought of as a point, we can divide it into several smaller parts and perform an integration to find the total field. For this study we just consider the point scatterer. This point scatterer generates secondary waves when acted upon by the incident wave. The scattered wave has the form of pulse with limited duration (Fig. 2). The coda is thought to be composed of numerous such scattering pulses.

To satisfy the Born approximation (weak, single scattering), the inhomogeneities are assumed to be small perturbations of the background material:

$$\rho = \rho_0 + \delta\rho$$

$$C_{ijkl} = C_{0\,ijkl} + \delta C_{ijkl}$$

ρ is the density and C_{ijkl} is the elastic constant. For the isotropic elastic medium considered here, the C_{ijkl}'s reduce to the Lame's constant λ or the rigidity μ. Since we just discuss the scattering from a small parcel, the mean behavior of these inhomogeneities is not assumed. These three parameters ρ, λ, and μ can be reduced to a single parameter, if there exists a relation among them. Sato (1984) used the velocity perturbation:

$$\frac{\delta V_P}{V_P} = \frac{\delta V_S}{V_S} = \xi$$

and adopted Birch's law relating the density and wave velocity

$$V_P = a_1\,\rho + a_0 \qquad V_S = b_1\,\rho + b_0$$

(a's and b's are constant). This results in

$$\frac{\delta\rho}{\rho} = v\,\xi \qquad \frac{\delta\lambda}{\lambda} = \frac{\delta\mu}{\mu} = (2 + v)\,\xi$$

The value of v is kept at 0.8 in this report. ξ will be the only parameter needed to describe the inhomogeneity variation under these assumptions. Wu (1984) used different values for density perturbation and elastic constant perturbation which results in two different types of inhomogeneities; impedance type and velocity type, each of which has different scattering properties. To reduce the number of independent parameters, we just use one parameter ξ to represent them.

As indicated by Hudson (1977), the scattered field for any first-order scattering theory can always be expressed using the representation theorem:

$$u_J^{(s)} = \int dV \left\{ \delta\rho\,\omega^2\,G_i^J\,u_i^0 - \delta C_{ijkl}\,\partial_j G_i^J\,\partial_l u_k^0 \right\}$$

For the isotropic elastic case, this is equivalent to

$$u_J^{(s)} = \int dV \left\{ \delta\rho\,\omega^2\,G_i^J\,u_i^0 - \delta\lambda\,\partial_i G_i^J\,\partial_j u_j^0 - \delta\mu\,\partial_j G_i^J\,(\partial_j u_i^0 + \partial_i u_j^0) \right\} \qquad (1)$$

where u_i^0 is the wave field incident on the inhomogeneous body, and G_i^J is the Green's function for the corresponding boundary conditions. For the case of body wave in a homogeneous space, G_i^J has the form as given by equation (4.30) in Aki and Richards (1980), which is used by Sato (1984) and Wu and Aki (1985). For the case of a surface wave in the layered medium, G_i^J can be determined by the normal mode theory (Malin, 1978).

The surface wave case is easy to construct since the incident wave and the scattered wave are trapped in the layers and propagate two dimensionally. From surface wave mode theory (Haskell, 1963; Haskell, 1964; Wang, 1981), the incident wave field, which has mode order m and wave type ν (ν = R for Rayleigh wave and L for Love wave), has the form

$$ {}^{\nu}u_m^0 = \frac{1}{\sqrt{2\pi\, {}^{\nu}k_m x}}\, {}^{\nu}S_m\, {}^{\nu}a_m\, e^{-i\, {}^{\nu}k_m x + i\frac{\pi}{4}}\, {}^{\nu}\mathbf{U}_m \tag{2} $$

$$ {}^{\nu}a_m = \frac{1}{2\, {}^{\nu}c_m\, {}^{\nu}g_m\, {}^{\nu}I_{0m}} $$

$$ {}^{R}\mathbf{U} = \Big[\, U_r\, ,\, 0\, ,\, -iU_z \,\Big]_{\text{at scatterer}} $$

$$ {}^{L}\mathbf{U} = \Big[\, 0\, ,\, U_\phi\, ,\, 0 \,\Big]_{\text{at scatterer}} $$

where
k = wave number,
x = the distance between the source and the scatterer,
a = amplitude factor,
c = phase velocity,
g = group velocity,
I_0 = energy integral of surface waves.
U_r, U_z, U_ϕ = displacement eigenfunctions in the radial,
vertical and tangential direction,

The source term S_m for double-couple and explosive sources is given in the Appendix. Solving equation (1), the Green's function with mode n and wave type η for the wave field after scattering is

$$ {}^{\eta}G_n^J = \frac{1}{\sqrt{2\pi\, {}^{\eta}k_n r}}\, {}^{\eta}\mathbf{U}_n\, {}^{\eta}a_n\, e^{-i\, {}^{\eta}k_n r + i\frac{\pi}{4}}\, {}^{\eta}\mathbf{R}_n^J \tag{3} $$

$$ {}^{R}\mathbf{U} = \Big[\, U_r\cos\theta\, ,\, U_r\sin\theta\, ,\, -iU_z \,\Big]_{\text{at scatterer}} $$

$$ {}^{R}\mathbf{R} = \Big[\, U_r\cos\phi\, ,\, U_r\sin\phi\, ,\, -iU_z \,\Big]_{\text{at receiver}} $$

$$ {}^{L}\mathbf{U} = \Big[\, U_\phi\sin\theta\, ,\, -U_\phi\cos\theta\, ,\, 0 \,\Big]_{\text{at scatterer}} $$

$$ {}^{L}\mathbf{R} = \Big[\, U_\phi\sin\phi\, ,\, -U_\phi\cos\phi\, ,\, 0 \,\Big]_{\text{at receiver}} $$

r is the distance from the scatterer to the receiver. The scattering angle θ and the receiving angle ϕ are defined in Fig. 1. These angles are important since they control the recorded wavefield. Scattered P-SV waves can appear on the receiver horizontal component defined as tangential with respect to the source.

Substituting these functions into the equation (1), the scattered wave field ${}^{\nu\eta}u_{mn}$ which includes the conversion from mode m of wave type ν to mode n of wave type η, is written as

$$ {}^{\nu\eta}u_{mn}^{(s)} = \int dV \frac{1}{2\pi\sqrt{{}^{\nu}k_m x\, {}^{\eta}k_n r}}\, {}^{\nu}a_m\, {}^{\eta}a_n S_m \mathbf{R}_n e^{-i({}^{\nu}k_m x + {}^{\eta}k_n r) + i\frac{\pi}{2}} $$

$$\cdot\left(\delta\rho\omega^2\ {}^{\nu\eta}A_{mn}-\delta\lambda\ {}^{\nu\eta}B_{mn}-\delta\mu\ {}^{\nu\eta}C_{mn}\right) \tag{4}$$

where

$$
\begin{aligned}
{}^{RR}A_{mn} &= U_{rm}\, U_{rn} \cos\theta + U_{zm}\, U_{zn} \\
{}^{RR}B_{mn} &= (\ {}^{R}k_m\ {}^{R}U_{rm} - \partial_z U_{zm})\ (\ {}^{R}k_n\ U_{rn} - \partial_z U_{zn}) \\
{}^{RR}C_{mn} &= 2\ (\ {}^{R}k_m U_{rm}\ {}^{R}k_n U_{rn} \cos^2\theta + \partial_z U_{zm} \partial_z U_{zn}) \\
&\quad + (\ {}^{R}k_m U_{zm} + \partial_z U_{rm})\ (\ {}^{R}k_n U_{zn} + \partial_z U_{rn}) \cos\theta
\end{aligned}
$$

$$
\begin{aligned}
{}^{RL}A_{mn} &= -U_{rm}\, U_{\theta n} \sin\theta \\
{}^{RL}C_{mn} &= -\ {}^{R}k_m U_{rm}\ {}^{L}k_n U_{\theta n} \sin 2\theta \\
&\quad -\partial_z U_{\theta n}\ (\partial_z U_{rm} +\ {}^{R}k_m U_{zm}) \sin\theta
\end{aligned}
$$

$$
\begin{aligned}
{}^{LR}A_{mn} &= U_{\theta m}\, U_{rn} \sin\theta \\
{}^{LR}C_{mn} &= {}^{L}k_m U_{\theta m}\ {}^{R}k_n U_{rn} \sin 2\theta \\
&\quad + \partial_z U_{\theta m}\ (\partial_z U_{rn} +\ {}^{R}k_n U_{zn}) \sin\theta
\end{aligned}
$$

$$
\begin{aligned}
{}^{LL}A_{mn} &= U_{\theta m}\, U_{\theta n} \cos\theta \\
{}^{LL}C_{mn} &= {}^{L}k_m U_{\theta m}\ {}^{L}k_n U_{\theta n} \cos 2\theta + \partial_z U_{\theta m}\ \partial_z U_{\theta n} \cos\theta
\end{aligned}
$$

We also define a scattering term F_{mn} as

$$
\begin{aligned}
{}^{\nu\eta}F_{mn} &= \int dV \left\{ e^{-i(\ {}^{\nu}k_m x +\ {}^{\eta}k_n r) + i\frac{\pi}{2}} \left(\delta\rho\omega^2\ {}^{\nu\eta}A_{mn} - \delta\lambda\ {}^{\nu\eta}B_{mn} - \delta\mu\ {}^{\nu\eta}C_{mn}\right) \right\} \\
&= \int dV \left\{ e^{-i(\ {}^{\nu}k_m x +\ {}^{\eta}k_n r) + i\frac{\pi}{2}} \xi \left[v\rho\omega^2\ {}^{\nu\eta}A_{mn} - (2+v)\lambda\ {}^{\nu\eta}B_{mn} - (2+v)\mu\ {}^{\nu\eta}C_{mn} \right] \right\} \\
&= \int dV \left\{ e^{-i(\ {}^{\nu}k_m x +\ {}^{\eta}k_n r) + i\frac{\pi}{2}}\ \xi\ {}^{\nu\eta}D_{mn} \right\}
\end{aligned} \tag{5}
$$

The final total field solution is the sum over all modes and conversions for all scatterers in the region. The scattering term F corresponds to the 'volume factor' of Wu and Aki (1985) if the Green's function related term D is not included. For a point scatterer, we simply use

$$ {}^{\nu\eta}F_{mn} = \delta V\, e^{-i(\ {}^{\nu}k_m x +\ {}^{\eta}k_n r) + i\frac{\pi}{2}}\ \xi\ {}^{\nu\eta}D_{mn} $$

with δV having the dimension of unit volume.

3. Scattering Q

To include the effect of energy loss due to scattering, Malin (1978) considered a correction which conserves energy to the first order by choosing a specific correlation function for the scattering cross section. Although we are interested in the behavior of each individual point scatterer, the scattering coefficient, or equivalently the cross section, is still needed when defining the scattering Q.

Let us consider a small scatterer parcel containing distributed inhomogeneities. For a single point scatterer, we can use a deterministic scattering formula. However, when a wave is incident on this scatterer parcel, the size of the scatterers within it, the relative distance between individual point scatterers, and the wavelength of the incident wave will determine the partition of energy being scattered. From scattering theory, the parameter describing this property is the 'cross section' (Ishimaru, 1977, *p.10*). Within a unit of the scattering angle, the differential cross section σ_d is defined by

$$\sigma_d = \lim_{r \to \infty} \frac{r\ (\text{ scattered energy flux density})}{(\text{ incident energy flux density})} \tag{6}$$

The total scattering cross section is obtained by integration over all angles:

$$\sigma_s = \int_{2\pi} \sigma_d \, d\theta$$

When scatterers are distributed with the mean density n (particles per unit area at a constant depth for a two dimensional case), the scattering coefficient α which characterizes the intensity of the scattered wave excitation is given by

$$\alpha = n\, \sigma_s$$

The reciprocal of α is usually called the mean free path. The scattering coefficient α thus defined is equivalent to the turbidity in the two dimensional case when compared to Aki and Chouet (1975).

To obtain the energy flux density, the wave field excited in the layered medium should be taken into account:

$$< |u|^2 > = \omega^2 \int dz \rho_0 < \mathbf{u}\mathbf{u}^* >$$

$<>$ means the average over the ensemble. Using equations (2) and (4), it is not difficult to find the scattering coefficient for mode pairs mn, and types $\nu\eta$ by setting r in equation (6) as the distance between the scatterer and the receiver:

$$\begin{aligned}
{}^{\nu\eta}\alpha_{mn} &= n \int_{2\pi} d\theta \frac{r < | {}^{\nu\eta}u_{mn}^{(s)} |^2 >}{< | {}^{\nu}u_m^0 |^2 >} \\
&= \frac{1}{2\pi} \frac{{}^{\eta}a_n{}^2}{{}^{\eta}k_n} \frac{{}^{\eta}I_{0n}}{{}^{\nu}I_{0m}} \int_{2\pi} n < {}^{\nu\eta}F_{mn}^2 > d\theta \\
&= \frac{1}{2\pi} \frac{{}^{\eta}a_n \ {}^{\nu}a_m \ {}^{\nu}g_m}{{}^{\nu}k_m \ {}^{\eta}g_n} \int_{2\pi} n < {}^{\nu\eta}F_{mn}^2 > d\theta \\
&= \frac{1}{2\pi} \ {}^{\eta\nu}A_{mn} \int_{2\pi} n < {}^{\nu\eta}F_{mn}^2 > d\theta
\end{aligned}$$

Now we have the problem of defining the average behavior of the function $< {}^{\nu\eta}F_{mn}^2 >$. Taking a closer look at the scattering region, Fig. 1, the scatterers are distributed over a plane area and the phase term in F_{mn}^2 (equation 5) is actually

$$\begin{aligned}
e^{-i\vec{k}_m \cdot \vec{x} - i\vec{k}_n \cdot \vec{r}} &= e^{-ik_m(x + \vec{e}_x \cdot \vec{\varsigma}) - ik_n(r - \vec{e}_r \cdot \vec{\varsigma})} \\
&= e^{-ik_m x - ik_n r} \, e^{-i\vec{\varsigma}cdot(k_m \vec{e}_x - k_n \vec{e}_r)} \\
&= e^{-ik_m x - ik_n r} \, e^{i \vec{\varsigma} \cdot \vec{k}_B}
\end{aligned}$$

$\vec{k}_B = \vec{k}_n - \vec{k}_m$ is called the Bragg vector. Hence, in evaluating F_{mn} from equation (5),

$$F_{mn} = \int dV \left\{ e^{-ik_m x - ik_n r + i\frac{\pi}{2}} \left[\xi(\vec{\varsigma},z)\, e^{i\vec{\varsigma}\cdot\vec{k}_B} \right] D_{mn}(z) \right\}$$

$$= \int dz \left\{ e^{-ik_m x - ik_n r + i\frac{\pi}{2}}\ \hat{\xi}\,(k_B,z)\, D_{mn}(z) \right\}$$

where we have made a two dimensional Fourier transform for the scatterer distribution spectra in the horizontal direction (Kennett, 1972). The ensemble average of F_{mn} is thus

$$<F_{mn}^2> = \int dz dz' \left\{ <\hat{\xi}(k_B,z)\ \hat{\xi}(k_B,z')> \ D_{mn}(z)\, D_{mn}(z') \right\}$$

$<\hat{\xi}\hat{\xi}'>$, the correlation function of inhomogeneity distribution, is usually given by a form of an exponential function or a Gaussian function (Chernov, 1960). Assuming that this function has a small side lobe, i.e., small correlation distance in the exponential form, we have a simpler form:

$$n<F_{mn}^2> = \left[n\int dz dz' \ <\hat{\xi}(k_B,z)\ \hat{\xi}(k_B,z')> \right] D_{mn}^2(z) = U_{sa}\, D_{mn}^2(z)$$

The term in the bracket, which describes the condition of scatterer distribution around the point considered, will be kept together and called a scattering attenuation unit (U_{sa}) . U_{sa} has the units of km^4. If U_{sa} is maintained as a constant value in the calculations, this is equivalent to stating that the scattering environment is similar for all waves propagating in the layered medium. The expression above is perhaps too simplified. The correlation function must be specified if an accurate scattering cross section is desired. In this study, we just use the simplest form to examine its possible effect.

The scattering coefficient thus has the from:

$$\begin{aligned}
{}^{RR}\alpha &= {}^{RR}A\, U_{sa} \left[\frac{3}{8}\, {}^{RR}\Theta_4 + \frac{1}{2}\, {}^{RR}\Theta_2 + \, {}^{RR}\Theta_0 \right] \\
{}^{RL}\alpha &= {}^{RL}A\, U_{sa} \left[\frac{1}{2}\, {}^{RL}\Theta_4 + \frac{1}{2}\, {}^{RL}\Theta_2 \right] \\
{}^{LR}\alpha &= {}^{LR}A\, U_{sa} \left[\frac{1}{2}\, {}^{LR}\Theta_4 + \frac{1}{2}\, {}^{LR}\Theta_2 \right] \\
{}^{LL}\alpha &= {}^{LL}A\, U_{sa} \left[\frac{1}{2}\, {}^{LL}\Theta_4 + \frac{1}{2}\, {}^{LL}\Theta_2 \right]
\end{aligned} \qquad (7)$$

Θ's are given in the Appendix I. We have used the distance r between the scatterer and the receiver to define the scattering coefficient (equation 6) and to calculate the incident energy flux and the scattered energy flux by fixing the source-scatterer-receiver geometry. The mode pair mn reduces its energy by $e^{-\alpha_{mn}(r+x)}$ after traveling the distance from source to scatterer to receiver. The effect thus caused by the scattering of inhomgeneities is called the scattering attenuation.

4. Numerical Experiment I: Wave type conversion and Mode conversion

With the velocity model chosen (CUS model, see Table 1), we generate the eigenfunctions of surface waves, mainly the Lg wave, up to 5 Hz. Using these, the scattered waves are created by specifying the source (depth, mechanism), the receiver (distance, instrument), the scatterers (location, material variation, and scattering intensity), and the attenuation condition (intrinsic Q and scattering Q). To make the problem easier to follow, we fix the following, except as indicated otherwise:

source depth = 10 km
scatterer depth = 4 km
source time function = parabolic with base 0.4 second.
receiver distance = 100 km
waveform observed = ground velocity
inhomogeneity variation = 5%
mode conversion = up to 10 neighboring modes (due to computer
restriction on speed and storage)
wave type conversion = yes

An arbitrary source mechanism was used and the effect of its radiation pattern is averaged out by distributing several scatterers on the ellipse. In this section, we will discuss the properties of t. e scattered waves under different scattering conditions but ignore the problem of scattering and intrinsic attenuation at this moment. The so called 'diagonal selection' rule (Malin, 1980) which states that a particular mode of surface wave mainly scatters into the same mode without significant conversion will be examined first. Scattering from different locations, e.g., distances, depths, scattering angle, etc., are also discussed.

Malin (1980) used the scattering coefficient of vertical component from an acoustic model to justify the diagonal selection rule. Since the scattered wave instead of its energy envelope is generated here, this rule will be discussed by examining the resultant waveforms. Two cases are studied; one is for the wave type conversion (from R to L and L to R), and the other for the mode conversion. Fig. 2 shows the waveforms of signals directly from the source (surface wave) or from a scatterer (scattered waves) after traveling the same distances as indicated at the ends of seismograms. Both the source depth and the scatterer depth are kept at 10 km. Scattered waves have more high frequencies and are of shorter duration than the direct surface waves. The major difference is in the excitation of the fundamental mode. The fundamental mode excited by the source does not excite the scatterers as well at high frequencies as do the higher modes. This is a result of the eigenfunction distribution with depth.

Fig. 3 examines the effect of wave type conversion on scattering. In this figure and those that follow, the number of kilometers indicates the total scattering distance, i.e. the distance from the source to the scatterer plus the distance from the scatterer to the receiver. The distance from the source to the receiver is fixed at 100 km. The angle in degrees is the location of the scatterer on an ellipse which has the source and the receiver at its foci and the coordinate origin at its center. Zero degrees indicates that the scatterer is behind the receiver, and 90 degrees indicate that the scatterer is equidistant from the source and receiver. Three different components of motion are plotted: vertical Z, radial R and the tangential T with respect to the source-receiver coordinates. In each pair of traces of Fig. 3, the lower one includes the wave type conversion and the upper one does not. No mode conversion is involved. From this comparison, we find that the wave type conversion is not obvious except at short distances for wide angle scattering. The Z component seems to be more independent of this effect than the other components. Thus it is concluded that wave type conversion is important only for the horizontal components at short distances. It is at these distances that wide angle scattering occurs. For large scattering distances relative to the source-receiver distance, backscattering is all that occurs from the geometry.

Fig. 4 illustrates the effect of mode conversion. Three cases are displayed in which the number of modes permitted to be converted to other near neighboring modes are 1, 5 and 10. In addition, the effects of wavetype conversion are also shown. The scattered waveforms are created by combining the effect of seven scatterers evenly distributed on the ellipse defined by the scattering distances. The amplitude scale of plotting for every scattering distance is the same. As in Fig. 3, the Z component seems stable and does not accumulate as much contribution from other modes except at the short distance where mode conversion must still be considered. On the other hand, the R and T components, Fig. 4(b) and 4(c), are sensitive to the number of modes allowed to convert each other and to the wave type conversion. These results do not support the diagonal selection rule, although the use of it alone will not cause major differences in the coda excitation. For an elastic medium, the energy exchange by mode conversion is important especially for the two horizontal components and for short distances. The mode conversion can be looked upon as being similar to a change of incident angle on the layered medium after scattering. This is an effect similar to the scattering pattern for body wave illustrated in Aki and Richards (1980, Chap 13). At short scatterer distances, because of the variation of scattered angle, the mode conversion must play an important role, affecting the energy of scattered waves.

We next examine the effect at different scatterer depths. A result is shown in Fig. 5 for a scattering distance of 200 km and a source depth of 25 km.. A Q model 10U0.5Q, which will be defined later, is also applied. It is found that the scatterer at greater depth preferentially excites the scattered waves with the higher phase velocities. The scatterer in the upper sedimentary layer (0.5 km) is capable of generating well dispersed, long duration scattered waves. Because of the dissipative attenuation included, the shallow scatterers yield waveforms that lose their energy and frequency content faster with increasing distance, which can make them similar to the waveforms of deeper scatterers. At larger propagation distances, the difference between scattered waves at different depths is gradually reduced, although the effect of attenuation may still be seen. Our studies indicate that a scatterer at any depth in the crust generates a similar scattered signal, as long as the propagation distance in large.

5. *Numerical experiment II: Scattering Q and Intrinsic Q*

As shown in the previous section, the scattering coefficient is a function of the correlation between scatterers, the inhomogeneity size, and the incident wave length. To make the problem easier to solve, we defined a scattering attenuation unit (U_{sa}) from which we obtained the scattering coefficient α after taking into account the angular scattering variation. The amplitude decay is given by $e^{-\alpha r/2}$ where r is the total scattering distance. In fact, this is a definition of turbidity which is used to describe the scattering energy loss mechanism (Dainty, 1981). In our model, the scattering attenuation is assumed the same for different scatterers which are distributed randomly and uniformly along scattering wave path passing through them. We will examine the effect of scattering on the wave energy loss and compare this with the attenuation due to anelastic absorption. The anelastic attenuation is calculated by perturbing the elastic constants and combining with the intrinsic Q values using surface-wave variational techniques.

Fig. 6 shows an example with scattering distance at 300 km and a scatterer depth of 0.5km. The uppermost trace in this figure is the reference trace which does not involve any Q effect. Other traces are named by the symbol pUqQ which is read as scattering Q having p U_{sa} and intrinsic Q having values from the model q. The basic Q model used is $Q_\beta = 300$ for upper 20 km and 2000 for the rest in the CUS model. 2Q indicates twice as much attenuation as 1Q, e.g., $Q_\beta=150$. It is obvious that the scattering Q reduces the high frequency energy less than intrinsic Q. This means that the scattering Q is not too sensitive to the scattering environment. If the anelastic part of structure does not dissipate all high frequency signal, the scattering Q may not reduce it even under strong scattering conditions. Furthermore the scattering Q reduces the scattered pulse amplitude but does not affect its frequency content much as can be seen from the traces in 10U0Q and 40U0Q. We also find that the scattering Q seems to suppress the lower mode signals and enhance the high frequency higher modes. However, this feature probably depends on the velocity model used From this test, we conclude that the effect of scattering Q and intrinsic Q are apparently different

If the scattered arrivals from different distances constitute the coda at different lapse times, the frequency content of these pulses may indicate the effect of Q at different places of coda. To examine this effect, we generate the scattered pulses at a distance of 500 km under different Q conditions. These are shown in Fig. 7. The Parts a and b are for the scatterer depths at 5 km and 15 km at these depths the Q_β values are different. The spectra of the traces are also plotted, shifted by a factor of ten for clarity. One thing revealed from this test at different distances is that the scattering attenuation absorbs the high frequency signal equally well irrespective of the scattering distance or the scatterer depth. This is due to the fact that a similar scattering environment is assumed when calculating scattering coefficient α. The intrinsic Q, on the other hand, attenuates the high frequency signals rapidly for a shallower scatterer where intrinsic Q is low. Fig. 7(a) and 7(b) can be thought of as two extreme cases: in 7(a) intrinsic Q dominates, and in 7(b) scattering Q dominates. The final Q value must result from the interaction of these two attenuation mechanisms. If the data show a strong frequency dependence at high frequency range, it is possible this is the attenuation from deep structure and the effect of scattering Q prevails. At the low frequency (<1 Hz), it is difficult to tell the difference between these two mechanisms.

6. Numerical Experiment III: Geometrical Spreading

Aki (1969) proposed a scattering theory which describes the coda waves of a local event as being composed of backscattered waves from many random distributed inhomogeneities in the lithosphere. A relation from his model, which has been widely used in the literature, is

$$A(\omega \mid t) = C(\omega) t^{-\nu} e^{-\omega t/2Q_c}$$

where $A(\omega \mid t)$ is the average peak-to-peak amplitude around the frequency ω and the time t, $C(\omega)$ is the coda shape function which includes the scattered wave excitation term and a dispersion correction, $t^{-\nu}$ is for geometrical spreading, and the exponential term describes the dissipative attenuation. The value of ν is taken as 1.0 for body waves, 0.5 for surface waves, and 0.75 for a diffusion model (Aki and Chouet 1975). Treating coda of local earthquakes (distance < 100 km), the source and the receiver are set at the same place to simplify the calculation of backscattering time in this model. Sato (1977) proposed a modification of the geometrical spreading factor for near scatterers which create waves arriving at the receiver just after the direct wave. This modification takes into account the separation between the source and the receiver and is used for regional earthquakes (Pulli, 1984). Kopnichev (1977) also derived a similar correction by considering the ellipticity of the scatterer surface for arrivals at a given time. In fact, this correction represents a geometrical change of the scatterer distribution ranging from a flattened ellipsoid to a shape similar to a sphere at large scatterer distances (from an ellipse to a circle for surface waves as illustrated in Fig. 1. It is purely a geometrical adjustment. However, as discussed in preceding sections, the scatterers at the near distances yield significant mode conversion and wave type conversion. A more complicated nature of scattered waves is expected there. Similarly, because of the importance of scattering angle in controlling the scattering mechanism (Wu, 1984), its effect must be significant at short distances where the scattering angle changes abruptly. In this section, we will measure this effect from simple numerical studies. The result indicates that the so called 'Sato's correction' which gives a heavier geometrical spreading correction in the early part of coda than Aki's formula is still too small as the scattered wave energy changes rapidly between modes and wavetypes at near distances.

In order to see the variation of geometrical spreading factor, we generate many scattered pulses at different scattering distances, ignoring dissipative attenuation, both of intrinsic and scattering. (In fact four distributed scatters are used for each scattering distance, and resulting amplitudes are increased by the square root of the distance to approximate a uniform distribution of scatterers). An averaged peak-to-peak amplitude is then measured, with narrow band filtering if needed, and plotted on log-log scale with the distance. One of the results is shown in Fig. 8(a). The scattering distance is spaced by 10 km up to 600 km and the receiver is kept at 100 km from the source. It is obvious that there exist two slopes. A steeper slope with amplitude dropping rapidly with the distance is seen in the front part. A similar tendency is also observed for the tangential component, Fig. 8(b). In these figures, the unfiltered scattered wave (upper one) and the filtered scattered wave all follow similar trends. This is due to a similar frequency response for scattered wave even traveling over different distances.

Fig. 9 shows a similar amplitude decay for a western United States model (Table 2). Here we have set the source-receiver distance at 300 km, Fig. 9(a), and at 100 km, Fig. 9(b). The rapid amplitude decay happens at the scatterer distances smaller than about 600 km and 200 km respectively. Hence, we may define an 'unstable region' corresponding to scattering distances smaller than twice the source-receiver distance, which has a rapid decrease in amplitude, and a 'stable region' at larger distances which has a spreading factor close to unity. This distance separation agrees with that of 'Sato correction' of twice the source-receiver distance. Note that the decay exponent in unstable region is greater than that in stable region by 0.5-1.0. This value is larger in WUS model than in CUS model (Table 1) for the Z component. Taking this into account, we propose a geometrical spreading correction to the RMS coda amplitude based on an extension of Sato's (1977) model to the surface wave:

$$\left|\frac{1}{\sqrt{\alpha^2-1}}\right|^{\frac{1}{2}} * \left(\frac{1}{\alpha^a}-\frac{1}{2^a}+1\right) \qquad \text{for } \alpha<2$$

$$\left|\frac{1}{\sqrt{\alpha^2-1}}\right|^{\frac{1}{2}} * \qquad \text{for } \alpha\geq 2$$

where α is the ratio of lapse time on the coda to the Lg wave propagation time and a is between 0.5 and 1.0. At larger lapse times, the geometrical spreading correction is proportional to α^{-1}. This correction is plotted in Fig. 10. The factor involving the square roots is obtained by an extension to the body-wave derivation of Sato (1977). The term following represents a correction based on the numerical experiments.

In propagating in a layered medium, not only does the amplitude of the scattered pulses decay with the distance but its duration also increases because of surface wave dispersion. We generated a set of waveforms at scattering distances of 110 to 450 km, measured the signal duration. Fig. 11 is a linear regression which shows the increase of measured duration with propagation distance. The CUS model exhibits an approximate increase in duration of 0.05 sec/km while WUS model exhibits an increase of 0.5 sec/km. Because a thicker sedimentary layer, the WUS model is to be more dispersive. This dispersion induced pulse duration expansion must be considered when summing all pulses to form the coda.

7. Numerical Experiment IV: Superposition of Scattered Pulses

We have discussed the properties of a single scattered pulse. The next question is how these pulses are combined to form the coda. In this section, we will conduct a numerical experiment using the parameters determined in the preceding sections to synthesize the coda envelope. From recent studies of coda Q of regional earthquakes, Pulli (1984) and Shin (1985) both observed lower coda Q values from the early part of coda. Der *et al.* (1984) also mentioned an obvious coherence difference in early and later coda. This section will attempt to propose an explanation to these observations.

From the study of scattered pulses just discussed, we make the following assumptions; 1) the shape of scattered pulse can be approximated by an exponential function te^{-at}; 2) the width of the pulse depends on its traveling distance with duration = a_o*distance; 3) the maximum amplitude of the pulse decays as $e^{-\pi ft/Q}\, t^{-m}$, where the exponential term describes the effect of attenuation including intrinsic or scattering Q, and t^{-m} is the geometrical spreading factor; 4) the pulses arrive at the receiver in a random manner, thus the number of pulses in a time interval at any time of seismogram is assumed to be approximately constant. To take into account reasonable variation, we also allow a 10% random variation for the parameters: m (spreading factor), a_o (duration expansion) and dtp (pulse interval). We will discuss the pulse at 1 Hz with the propagation velocity 3.5 km/sec.

With each pulse defined, the coda is then synthesized by summation of many pulses. One example of synthetic coda thus formed can be seen from Fig. 12 where every individual pulse and the coda envelope after summation are plotted assuming different parameters. Since the energy of random arrivals is mixed, we use a root-mean-square rule to form the coda envelope. After constructing the coda, we then apply the Aki-Chouet's (1975) model with surface-wave spreading correction, i.e., $t^{-0.5}$ to calculate the coda Q value. This corresponds to an $m = 1.0$ for the geometrical spreading factor of the individual scattering pulses. The objective here is to see how the coda Q estimate is affected if the actual geometrical spreading in the early part of the coda is actually more rapid. The Q values at two regions, first 100 seconds and the rest, are calculated separately. Here a sliding window with 10 seconds length (Pulli, 1984) is also used when taking points from the coda shape. The cases for different values of m, a_0 and dtp, which represent different scattering conditions, are examined.

One interesting result revealed by this simple test is that the pulse spreading factor, m, is the most important factor which controls the coda shape decay. The duration factor and the pulse density, on the other hand, only have limited effect on the coda formation if the pulses are crowded together enough to make a smoothly decaying coda shape as usually observed. The dispersion of scattered pulses in the layered medium, which causes the duration increase, does not affect the coda as much as first expected (Dainty, 1984). We also found that for a low Q region the coda decays rapidly, thus not too many pulses are needed and its Q value comes out fairly stably. The coda is said to be 'saturated' by attenuation. For a high Q region, different pulse parameter will play an important role on the coda formation.

As a result of repeating the above experiment for different combination of parameters m, a_0, and dtp, we obtained a preliminary understanding of the constitution of coda by the summation of scattering waves:

1) For a high Q region, such as the eastern United States, the manner the scattered pulse decays with the distance, because of geometric spreading or mode conversion, controls the value of Q determined from coda shape. A large m value in the early part of coda (unstable region) has a major effect on Q value. This is the case predicted in Fig. 12(a).

2) For a low Q region, such as the western United States, the pulses which arrive at the receiver to form the coda are strongly affected by the attenuation and thus the coda shape is a stable estimator of Q. This is shown in Fig. 12(b).

3) The pulses with longer duration yield a longer tail which in turn leads to a higher Q estimate, but this effect is not as strong as expected.

4) If the pulses do mix to form the coda, the density of pulse arrivals is not very important with respect to the final coda Q values. This is due to the fact that the pulses are superimposed by means of the energy which reduces the difference in the number of pulses.

5) Estimation of coda Q using only earlier parts of the coda requires knowledge of the rate of correct geometrical spreading term there.

The summation of pulses as mentioned above is confirmed by actually summing the scattered pulses generated in the layered model. Fig. 13 is the result. 100 scatterers are distributed randomly with the scattering distance between 300 km and 400 km in the CUS model. A Q model 10U0Q is also used. The slope from this synthetic coda is very close to that predicted the first trace in Fig. 12. At these scattering distances, the ratio of the coda lapse time to the Lg propagation time is greater than 2.

8. Numerical Experiment V: Body Wave Scattering

The theory of body-wave scattering in the earth has been widely discussed from the points of view of scattering from a discrete volume (Knopoff, 1959; Wu, 1984) or as superposition of scattered body-waves (Sato, 1984). These theories, however, use a plane wave reacting with the scatterer in a whole space or at most a halfspace. In this section, we will discuss body-wave scattering in the layered medium. The layered earth structure is an important factor which provides a circumstance for waves to react with inhomogeneities by trapping waves in the layers. We will simply extend the theory developed for surface-waves, i.e., Lg waves, to body-waves by using 'locked mode' approximation (Harvey, 1981). This is done by adding a rigid cap layer at great depth in the original model to trap the body-waves. In doing this, the body-waves become a subset of the surface-wave field. Hence, we can easily extend the first-order scattering theory to cover this part of scattering signals.

If care is taken in the choice of the cap layer properties, the body-wave scattering waveform will be generated as shown in Fig. 14. The second trace in this figure is an exaggeration of the body-wave part from the first trace which is the scattering wave generated by the locked mode approximation using WUS model. The third trace is the scattering wave from surface-wave mode only. Body-wave scattering is strong around the P and S arrivals. We can also see some body-wave and surface-wave scattering interaction.

From their spectra plots, we can see that the scattered pulses contain similar frequencies if there is no attenuation. However, the attenuation makes the difference. Fig. 14(b) and 14(c) shows the effects of intrinsic Q and the scattering Q, respectively. It is interesting to see that the body-wave scattering suffers much less attenuation than surface-wave scattering especially in high frequency range. This can be seen more apparently in Fig. 15 where spectra under different Q conditions are plotted for surface and body-wave scattering respectively for a scattering distance of 250 km.. The high frequency spectrum slopes do not show as much variation for body-wave scattering as for surface-wave scattering. This implies that the body-wave scattering retains more high frequencies than the surface-wave scattering after attenuation. This makes the body-wave scattering dominant at high frequencies as observed by Shin (1985).

9. Conclusion

After examing the behavior of scattered pulses generated in a layered medium, we have the following conclusions:

1) The 'diagonal selection' rule which predicts no mode conversion is not proper for scattering in the layered elastic medium. Mode conversion must be considered especially for the horizontal components or at short distances.

2) The wave type conversion between Rayleigh and Love waves, on the other hand, can be ignored except at short distances.

3) The scatterers near the surface can generate well dispersed scattered waves, but they also lose energy faster because of dissipative attenuation. The combined effect of attenuation and layering makes the scatterer depth dependence less significant.

4) The variation of scattering Q does not affect the value of apparent Q as much as the intrinsic Q. For the same scattering environment, the attenuation of high frequencies from scattering Q does not seem to depend much on the scattering location.

5) It is difficult to make a distinction between the effect of scattering Q and intrinsic Q on the final Q value.

6) Larger geometrical spreading decay is found in the early part of coda. It falls off by a factor of $t^{-0.5}$ to t^{-1} faster than the later part. The geometrical correction in the early unstable region of coda is suggested to be larger than the simple Sato's correction. This is caused mainly by rapid mode or wave type conversion from scatterers at near distances.

7) If the scattering pulses which constitute the coda are dense enough, which is required to make a smooth decaying coda envelope, the geometrical correction factor will control the value of coda Q.

8) The body-wave scattering suffers less attenuative absorption than the slower surface wave scattering.

9) The effect of layering on the coda formation is very important. Because of wave trapping in the layers, even a weak scatterer distribution may create observerable coda. This layering is the same reason that makes the Lg phase the most dominant phase in regional

earthquakes seismograms.

Acknowledgments

This work was supported in part by the National Science Foundation under Grant No. CEE-8406577 and by the AFSC under Contract F19628-85-K-0029.

References

Aki, K. (1969). *Analysis of the seismic coda of local earthquakes as scattered waves.* J. Geophys. Res. *74*, 615-631.

Aki, K. (1982). *Scattering and attenuation.* Bull. Seism. Soc. Am. *72*, S319-S330.

Aki, K. and Chouet, B. (1975). *Origin of coda waves: source attenuation and scattering effects.* J. Geophys. Res. *80*, 3322-3343.

Aki, K. and Richards, P., *Quantitative Seismology: Theory and Method, Vol. I.* (W. H. Freeman and Company, San Francisco 1980).

Chernov, L. A., *Wave Propagation in a Random Medium,* (McGraw-Hill, New York 1960).

Dainty, A. M. (1981). *A scattering model to explain seismic Q observations in the lithosphere between 1 and 30 Hz.* Geophys. Res. Letters 11, 1126-1128.

Dainty, A. M. (1984). *Influence of Scattering on Q in the Lithosphere.* Final report to the AFSOR, Georgia Institute of Technology, Atlanta, Georgia.

Der, Z. A., Marshall, M. E., O'Donnell, A. and McElfresh, T. W. (1984). *Spatial coherence structure and attenuation of the Lg phase, site effects, and the interpretation of the Lg coda.* Bull. Seism. Soc. Am. *74*, 1125-1147.

Harvey, D. J. (1981). *Seismogram synthesis using normal mode superposition: locked mode approximation.* Geophys. J. R. Astr. Soc. *66*, 37-69.

Haskell, N. A. (1963). *Radiation pattern of Rayleigh waves from a fault of arbitrary dip and direction of motion in a homogeneous medium* Bull. Seism. Soc. Am. *53*, 619-642.

Haskell, N. A. (1964). *Radiation pattern of surface waves from point sources in a multi-layered medium.* Bull. Seism. Soc. Am. *54*, 377-393.

Hudson, J. (1977). *Scattering waves in the coda of P.* Geophys. J. R. Astr. Soc. *48*, 359-374.

Ishimaru, A., *Wave Propagation and Scattering in Random Media,* (Academic Press, New York 1977).

Kennett, B. L. N. (1972). *Seismic waves in laterally inhomogeneous media.* Geophys. J. R. Astr. Soc. *27*, 301-325.

Knopoff, L. (1959). *Scattering of compressional waves by spherical obstacles.* Geophysics *24*, 30-39.

Kopnichev, Y. F. (1977). *Models for the formation of the coda of the longitudinal wave.* Proc. (Dokl.) Acad. Sci. USSR *234*, 13-15.

Malin, P. E. (1978). *A first order scattering solution for modeling lunar and terrestrial seismic codas. Ph.D. Dissertation*, Princeton University.

Malin, P. E. (1980). *A first-order scattering solution for modelling elastic wave codas - I. The acoustic case.* Geophys. J. R. Astr. Soc. *63*, 361-380.

Pulli, J. J. (1984). *Attenuation of coda waves in New England.* Bull. Seism. Soc. Am. *74*, 1149-1166.

Sato, H. (1977). *Energy propagation including scattering effect; single isotropic scattering.* J. Phys. Earth **25,** 27-41.

Sato, H. (1984). *Attenuation and envelope formation of three-component seismograms of small local earthquakes in randomly inhomogeneous lithosphere.* J. Geophys. Res. *89*, 1221-1241.

Shin, T.-C. (1985). *Lg and coda wave studies of Eastern Canada.* Ph. D. Dissertation, Saint Louis University.

Wang, C. Y. (1981). *Wave theory for seismogram synthesis* Ph.D. Dissertation, Saint Louis University, St. Louis, Missouri.

Wu, R. S. (1984). *Seismic wave scattering and the small scale inhomogeneities in the lithosphere.* Ph.D. Dissertation, Massachusetts Institute of Technology.

Wu, R.S. and Aki, K. (1985). *Scattering characteristics of elastic waves by an elasteic heterogeneity.* Geophysics *50*, 582-595.

Appendix

I. Source Function:

For a double couple source, the source mechanism can be determined by the dip d , slip s, and strike ϕ in the following forms:

$$ {}^{R}S = {}^{R}k\, U_r R_{ss} + \left(\frac{dU_z}{dz} + \frac{1}{2}\, {}^{R}k\, U_r\right) R_{dd} + i\left({}^{R}k\, U_z + \frac{dU_r}{dz}\right) R_{ds} $$

$$ {}^{L}S = {}^{L}k\, U_\phi R'_{ss} - i\frac{dU_\phi}{dz} R'_{ds} $$

where

$$ R_{ss} = -\text{sind cos}s\ \sin 2\phi - \frac{1}{2}\sin 2d\ \text{sins}\ \cos 2\phi $$

$$ R_{dd} = \text{sins}\ \sin 2d $$

$$ R_{ds} = \cos 2d\ \text{sins}\ \sin\phi - \text{cosd cos}s\ \cos\phi $$

$$ R'_{ss} = \text{sind cos}s\ \cos 2\phi - \frac{1}{2}\sin 2d\ \text{sins}\ \sin 2\phi $$

$$ R'_{ds} = \text{cosd cos}s\ \sin\phi + \cos 2d\ \text{sins}\ \cos\phi $$

For an explosive source, only the Rayleigh wave has a source function:

$$ {}^{R}S = \frac{dU_z}{dz} - {}^{R}k\, U_r $$

${}^{L}S = 0.$

II. Scattering angular integration:

The angular integrations for determining the scattering coefficient (Equation 7) are

$$\Theta_4 = C_0 c_2^2$$

$$\Theta_2 = A_0 a_1^2 + C_0 c_1^2 + 2C_0 c_2 c_0 + E_0(a_1 c_1 + a_0 c_2) + F_0 b_0 c_2$$

$$\Theta_0 = A_0 a_0^2 + B_0 b_0^2 + C_0 c_0^2 + D_0 a_0 b_0 + E_0 a_0 C_0 + F_0 b_0 c_0$$

where

$$A_0 = (v\rho\omega^2)^2 \qquad B_0 = ((2+v)\lambda)^2 \qquad C_0 = ((2+v)\mu)^2$$

$$D_0 = -2v(2+v)\rho\lambda\omega^2 \qquad E_0 = -2v(2+v)\rho\mu\omega^2 \qquad F_0 = 2(2+v)^2\lambda\mu$$

And a's, b's, and c's for RR conversion are

$$a_1 = U_{rm} U_{rn} \qquad a_0 = U_{zm} U_{zn}$$

$$b_0 = (k_m U_{rm} - \partial_z U_{zm})\,(k_n U_{rn} - \partial_z U_{zm})$$

$$c_2 = 2k_m U_{rm}\, k_n U_{rn} \qquad c_1 = (k_m U_{zm} + \partial_z U_{rm})(k_n U_{zn} + \partial_z U_{rn})$$

$$c_0 = 2\partial_z U_{zn} \partial_z U_{zn}$$

for RL,

$$a_1 = U_{rm} U_{\phi n} \qquad a_0 = 0$$

$$b_0 = 0$$

$$c_2 = k_m U_{rm} k_n U_{\phi n} \qquad c_1 = \partial_z U_{rm} \partial_z U_{\phi n} + k_m U_{zm} \partial_z U_{\phi n} \qquad c_0 = 0$$

for LR,

$$a_1 = U_{\phi m} U_{rn} \qquad a_0 = 0$$

$$b_0 = 0$$

$$c_2 = k_m U_{\phi m} k_n U_{rn} \qquad c_1 = \partial_z U_{\phi m} \partial_z U_{rn} + k_m U_{\phi m} \partial_z U_{zn} \qquad c_0 = 0$$

and for LL,

$$a_1 = U_{\phi m} U_{\phi sn} \qquad a_0 = 0$$

$$b_0 = 0$$

$$c_2 = k_m U_{\phi m} k_n U_{\phi n} \qquad c_1 = \partial_z U_{\phi m} \partial_z U_{\phi n} \qquad c_0 = 0$$

Table 1
Central United States Model (CUS)

d	α	β	ρ	Q_α	Q_β
1	5.00	2.89	2.5	600	300
9	6.10	3.52	2.7	600	300
10	6.40	3.70	2.9	600	300
20	6.70	3.87	3.0	4000	2000
	8.15	4.70	3.4	4000	2000

Table 2
West United States Model (WUS)

d	α	β	ρ	Q_α	Q_β
2	3.55	2.06	2.20	170	85
3	6.15	3.27	2.79	300	150
18	6.15	3.57	2.79	300	150
8	6.70	3.93	2.97	1000	500
8	6.70	3.73	2.97	1000	500
	7.80	4.41	3.35	2000	1000

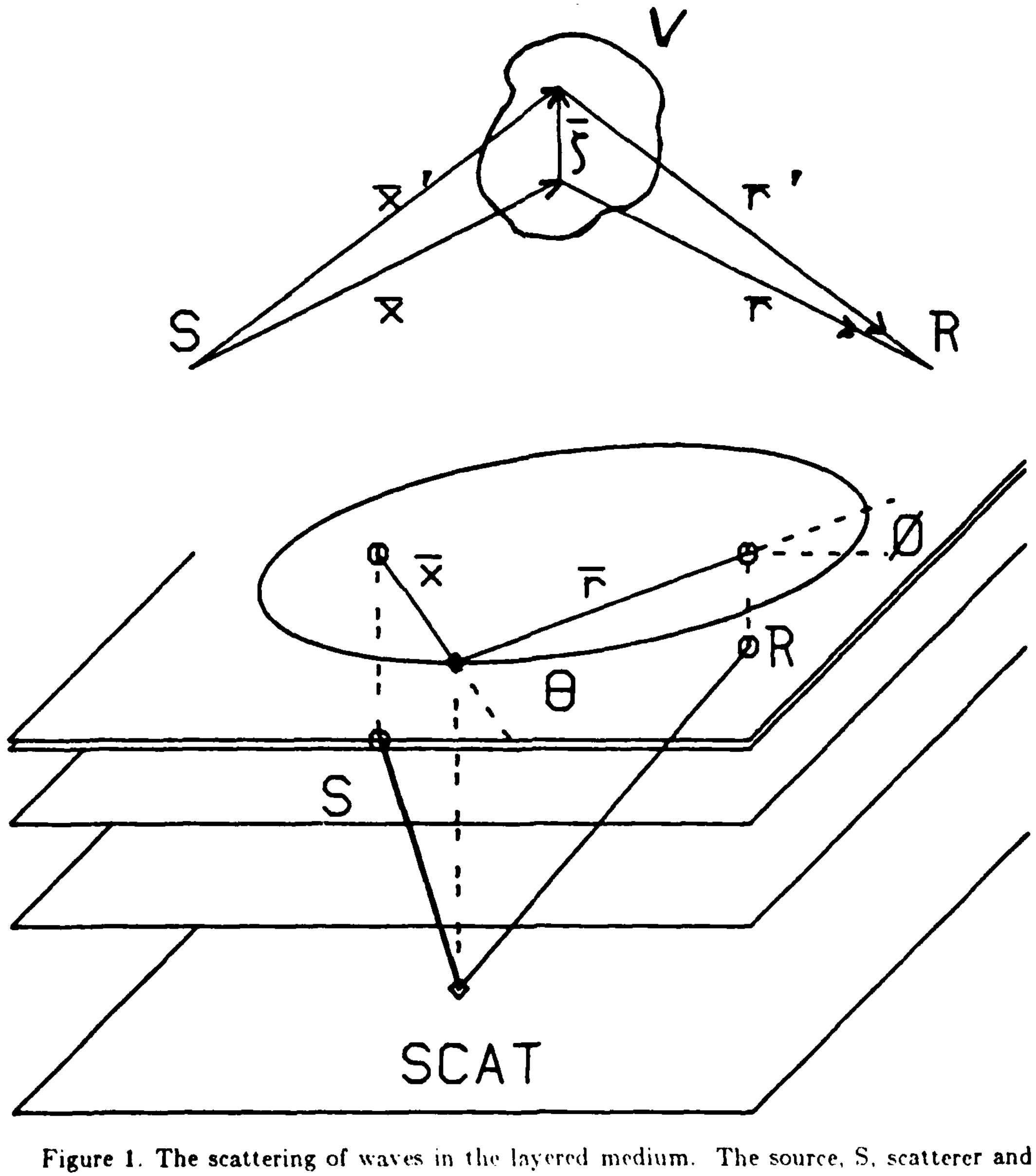

Figure 1. The scattering of waves in the layered medium. The source, S, scatterer and receiver R are shown. For a given source-receiver distance, the locus of all scatterers at a given depth forms an ellipse, which is displayed at the surface.

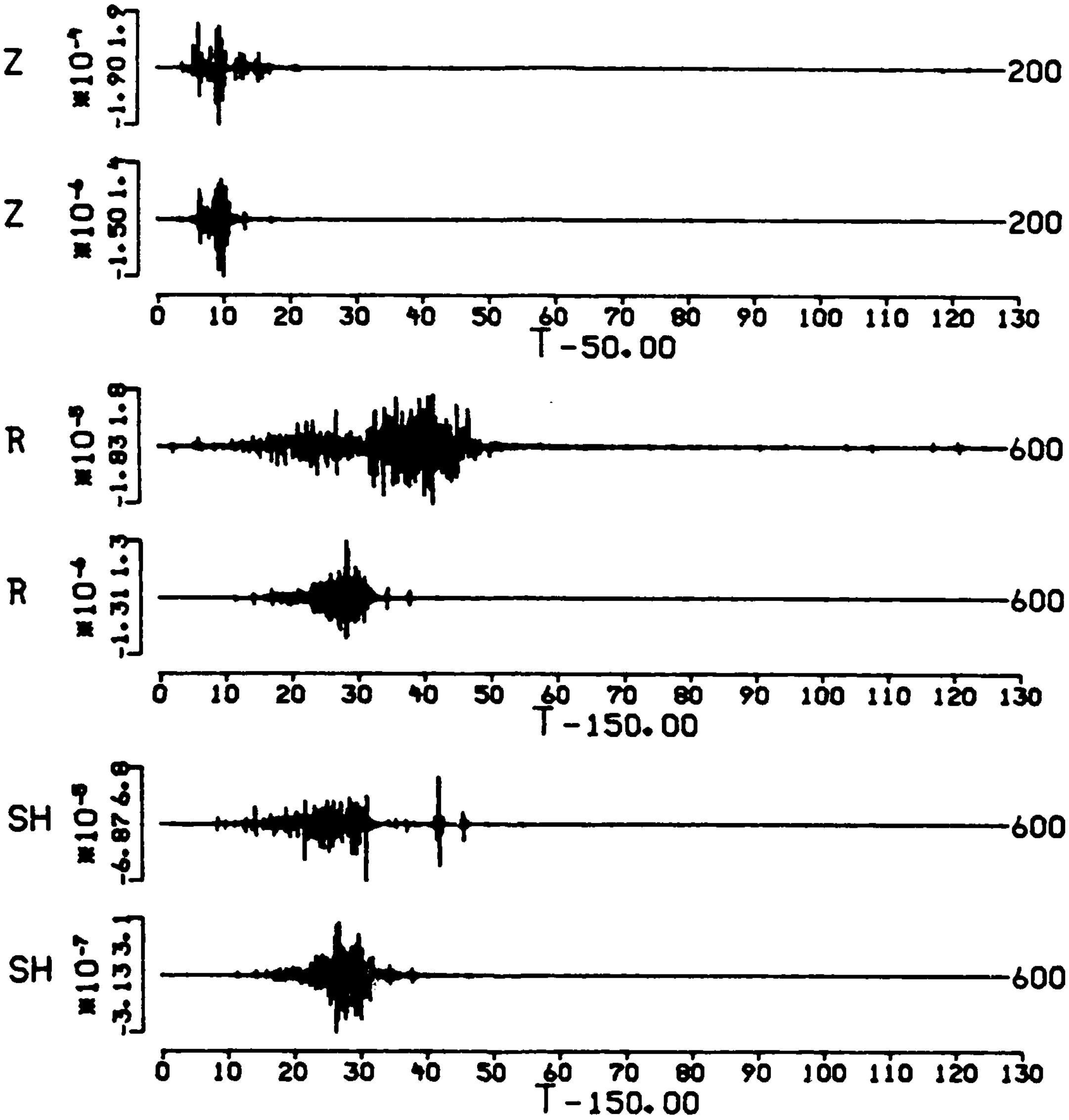

Figure 2. A comparison of waveforms of direct surface waves and the scattered waves. The numbers at the end of each seismogram indicates the source-receiver distance for surface-waves and the source- scatterer-receiver distance for the scattered waves. The scattered waveform is much more concentrated than the direct wave.

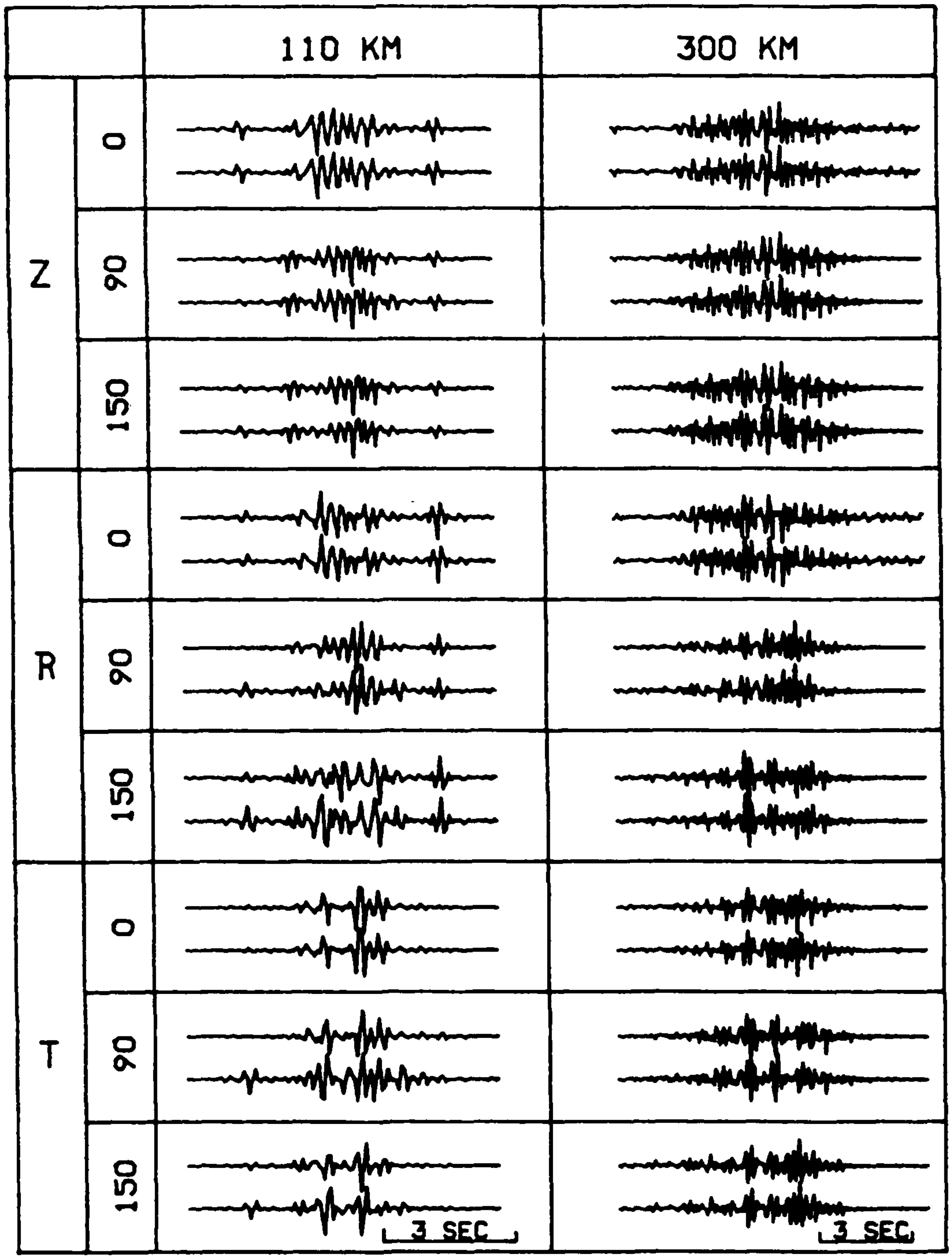

Figure 3. Wave type conversion test. The upper trace in each pair of seismograms does not include wave type conversion and the lower one does. The tests are for scatterers at the distances of 110 km and 300 km, and at the angles 0, 90 and 150 degrees on an ellipse. Note the waveform difference in wide angle scattering (90 or 150) for the short distance (110 km).

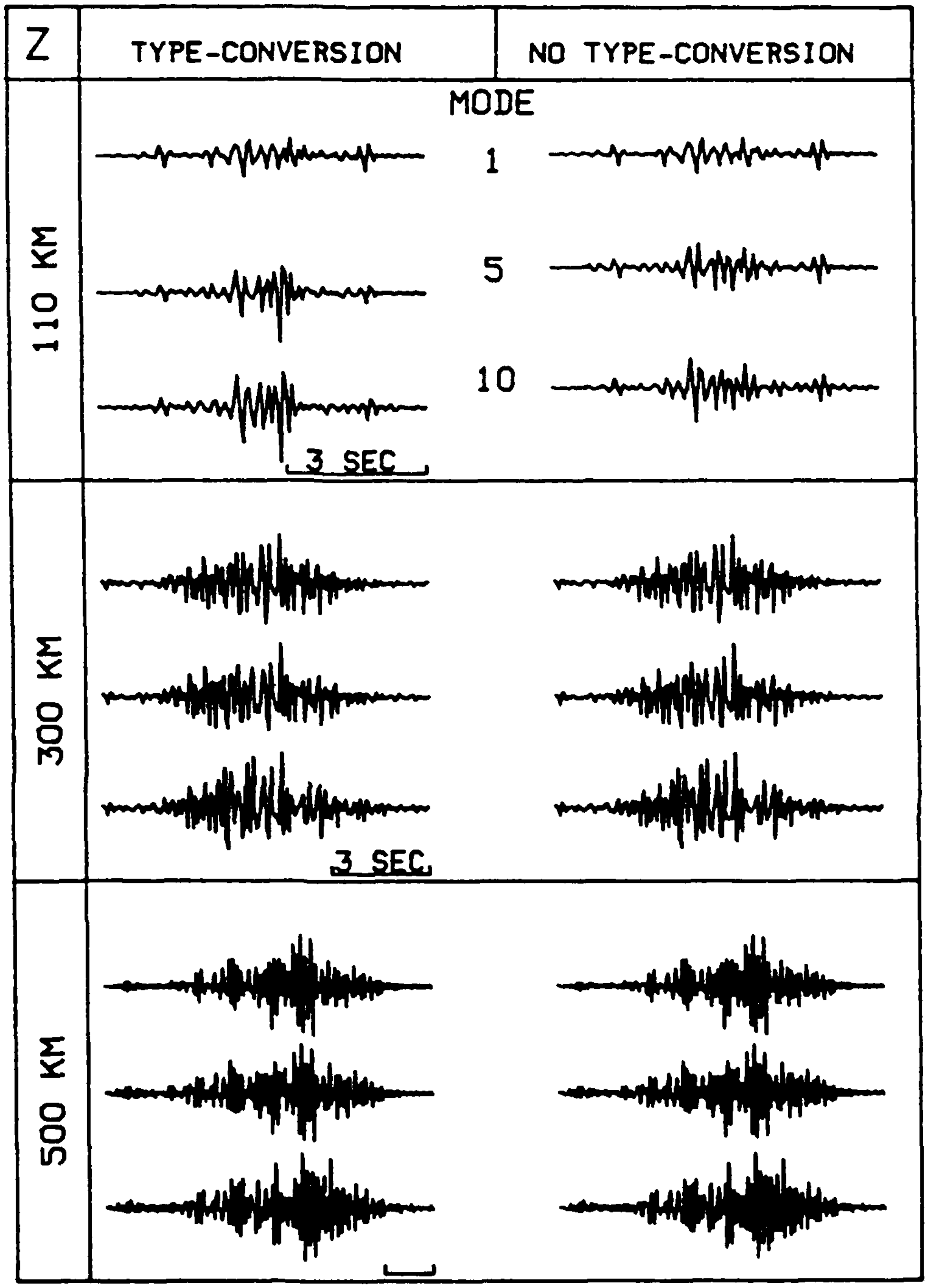

Figure 4. Mode conversion test. Cases discussed are for mode conversion permitted for up to 1, 5 and 10 neighboring modes. Three scattering distances 110 km, 300 km and 500 km are included. Two columns correspond to cases with or without wave type conversion respectively. Plots a, b and c are for three different components for the horizontal components. Obvious mode conversion occurs for the short distance scattering (110 km).

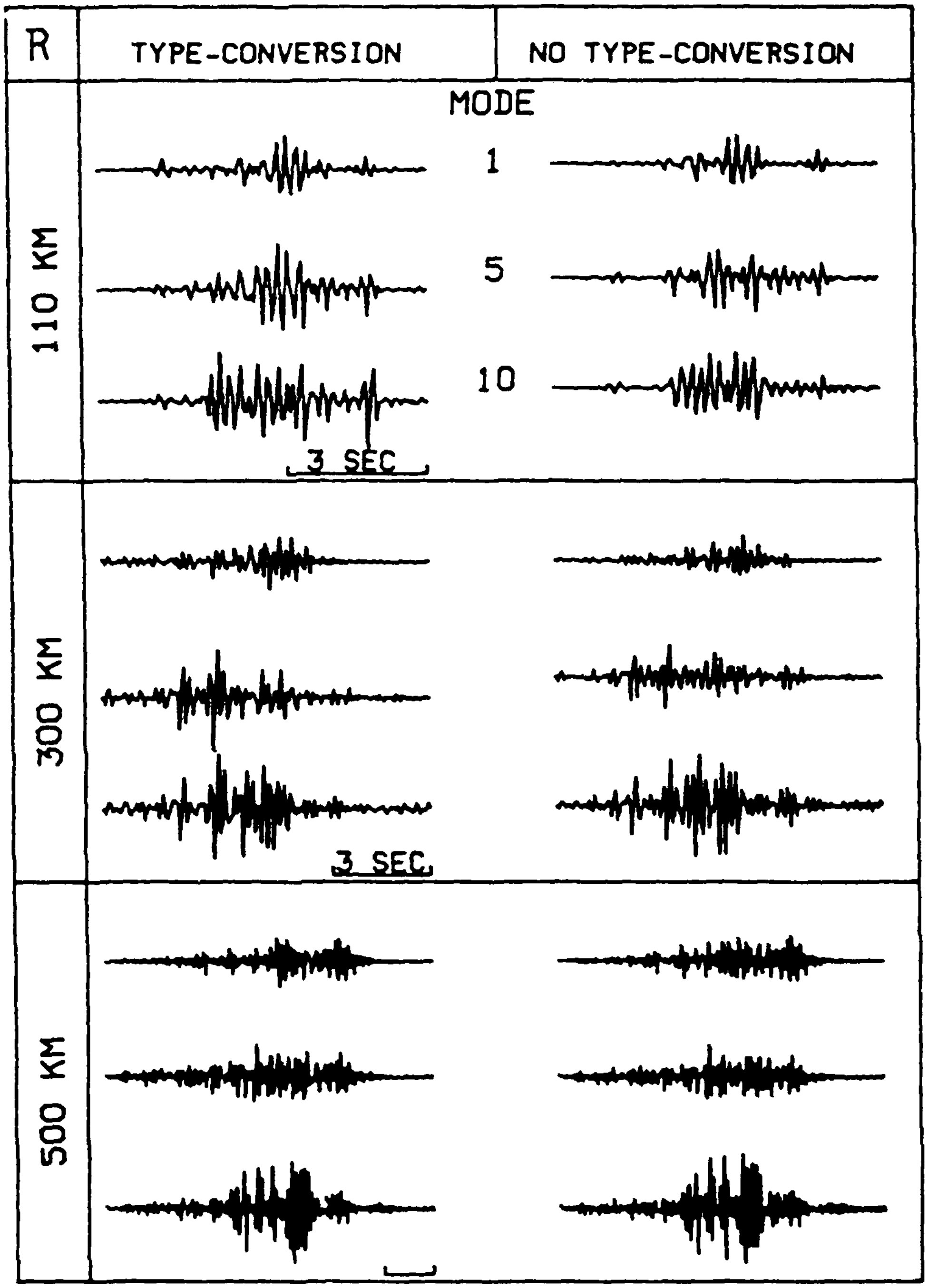
R
TYPE-CONVERSION
NO TYPE-CONVERSION
MODE
1
5
10
110 KM
3 SEC
300 KM
3 SEC
500 KM

Figure 4b.

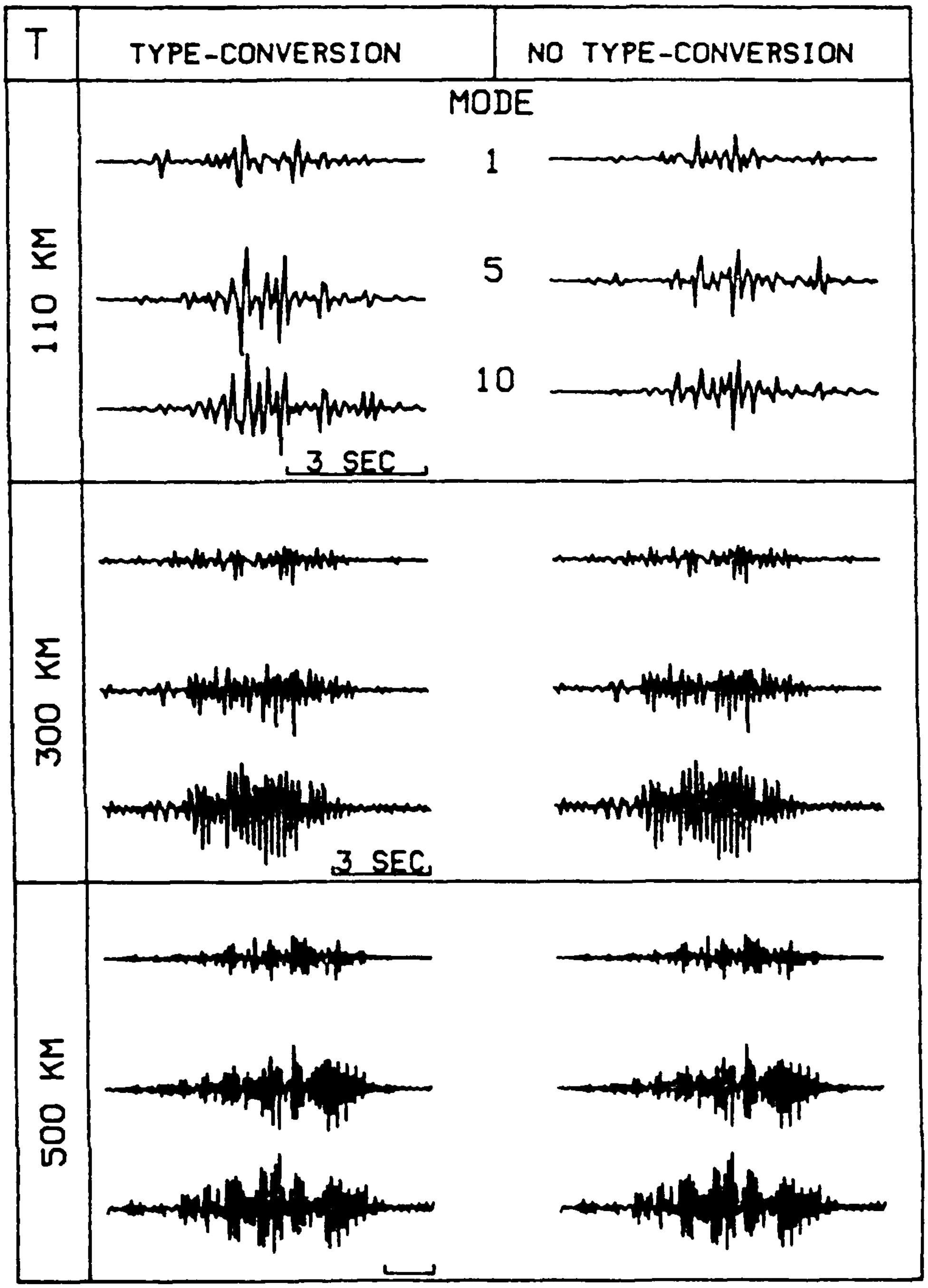
T
TYPE-CONVERSION
NO TYPE-CONVERSION
MODE
1
5
10
110 KM
3 SEC
300 KM
3 SEC
500 KM

Figure 4c.

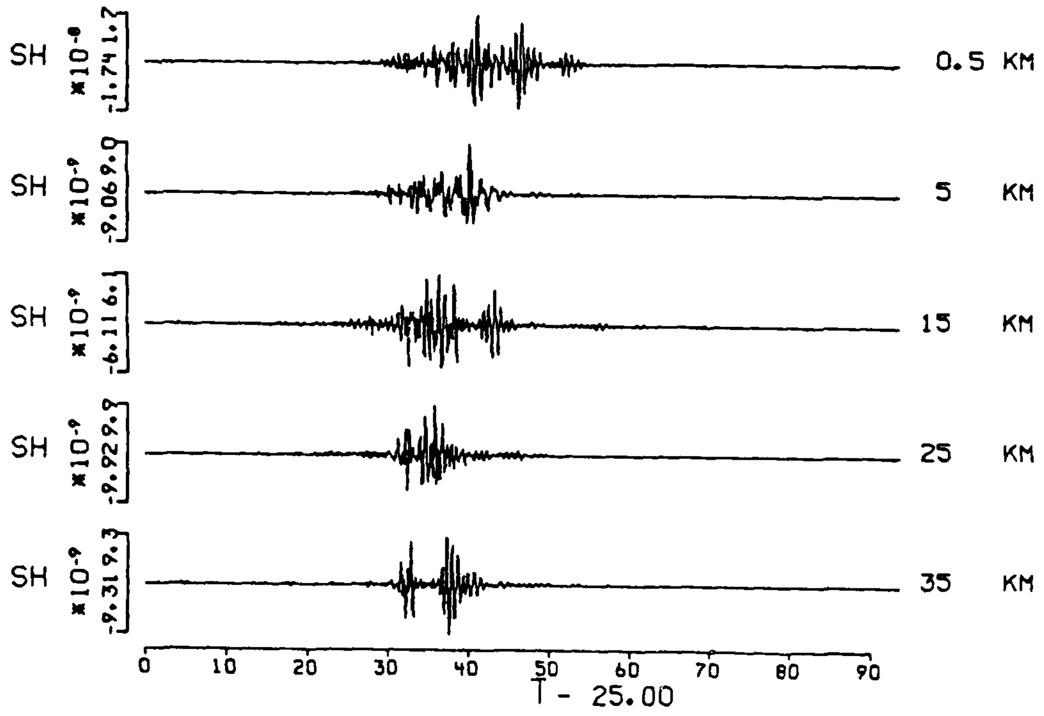

Figure 5. The effect of scatterer depth. The source depth is at 25 km, the sacttering distance is 200 km, and the the scatterer depth is indicated at the end of each seismogram. A Q model 10U'1Q is also applied.

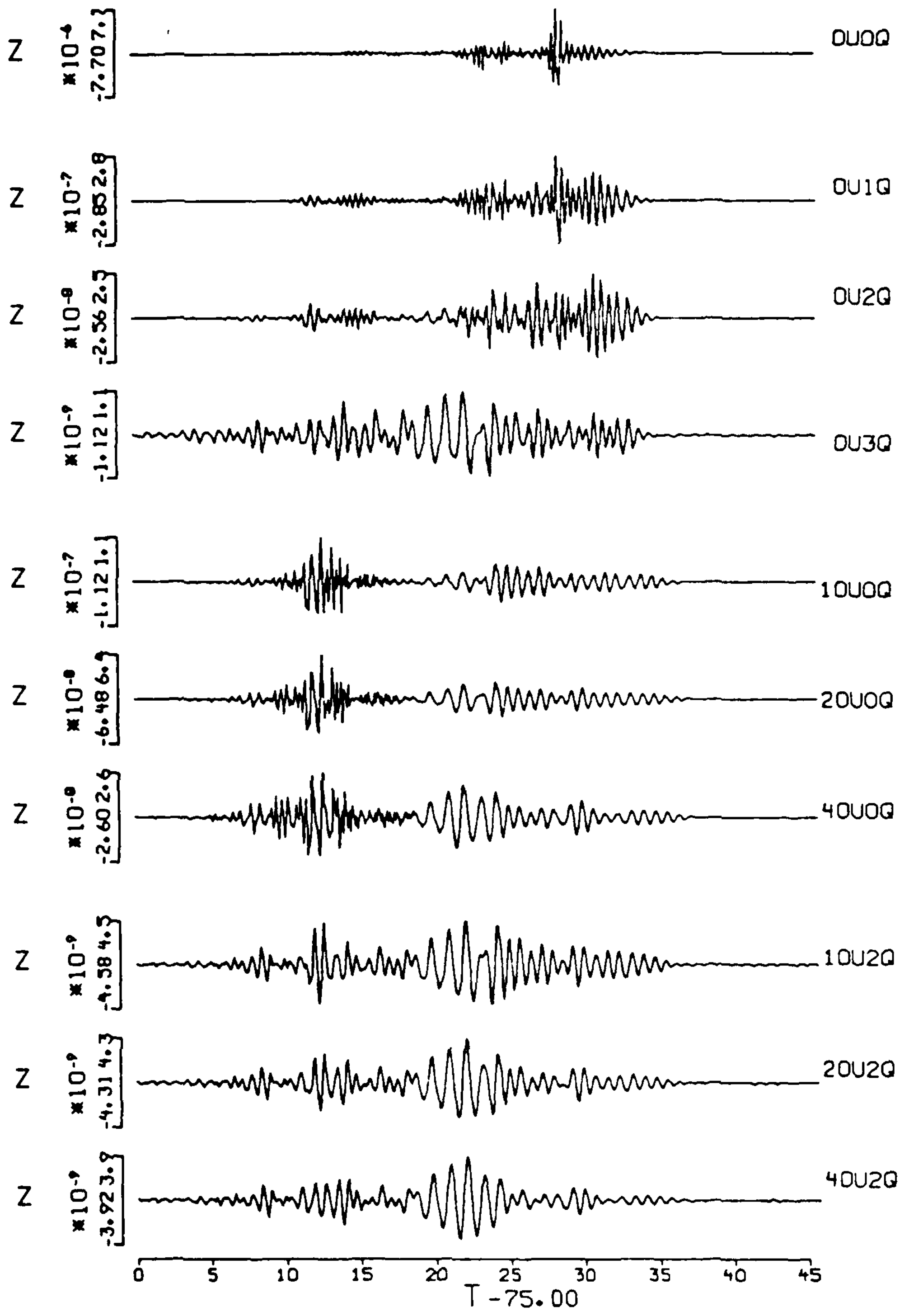

Figure 6. A comparison of the effect of scattering Q and intrinsic Q. The scatterers are at the depth of 0.5 km and the scattering distance is 300 km. 10U2Q means 10 scattering attenuation unit (U_{sa}) and double anelastic attenuation as given by Q model in Table 1. Note that the frequency content of the nU0Q cases is very similar. The effect of scattering Q seems to enhance the high frequency and higher mode signals

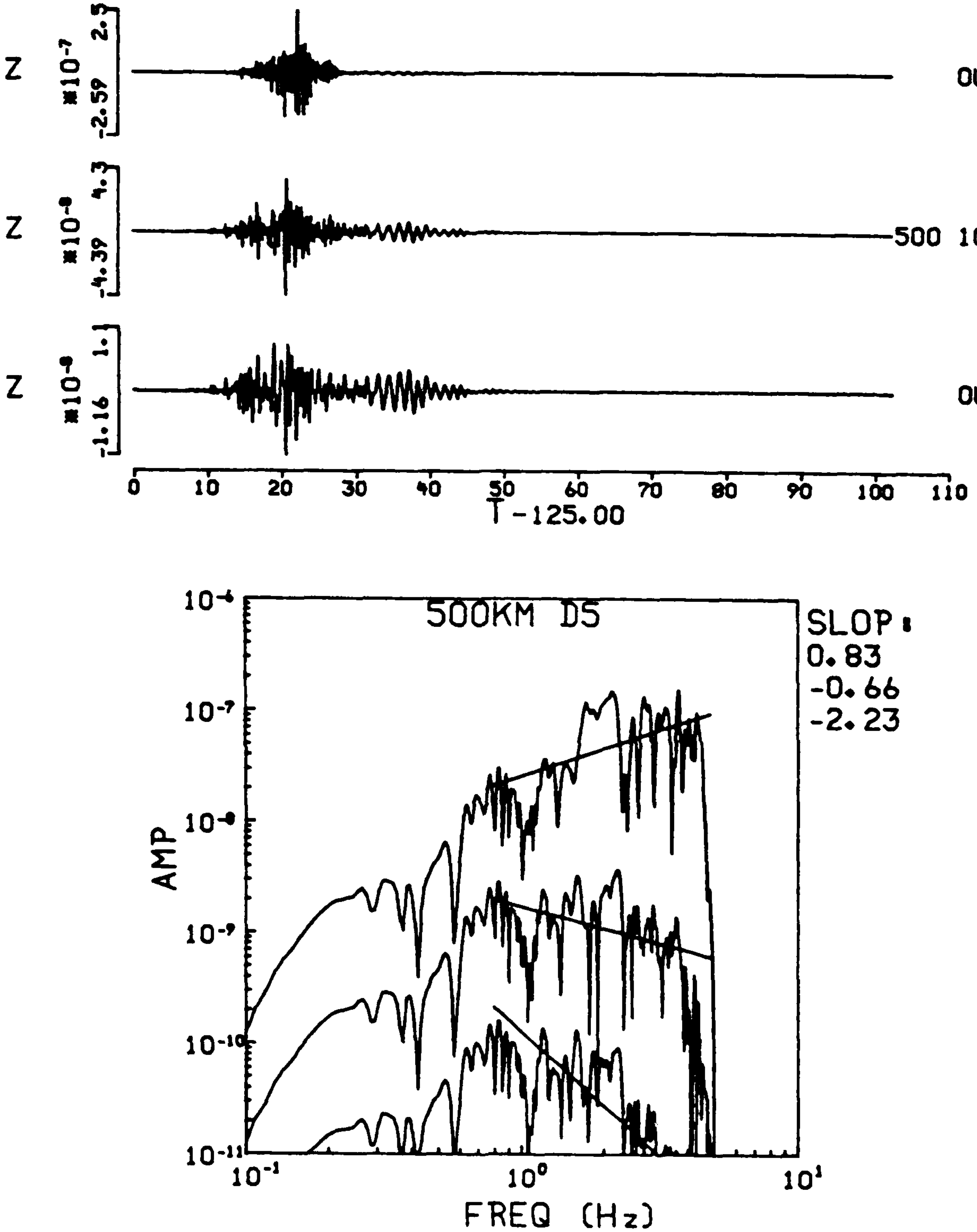

Figure 7. The scattering waveforms and their spectra under different attenuation conditions. The scattering distance is 500 km and the scatterer is at the depth of 5 km (a) and 15 km (b) in CUS model. The spectra plotted are in the same sequence as the seismograms but shifted by a factor of ten for clarity. Their high frequency spectra slopes are also indicated. After traveling large distances, the high frequencies are absorbed due to scattering and anelastic absorption. The scattering Q seems to have similar effect for scatterers from different depths, however, intrinsic Q affects the shallower scatterer more since the intrinsic Q value is low near the surface. In case (a), the anelastic Q controls the decay of wave energy. On the other hand, in case (b) the scattering Q is dominant in controlling the frequency decay.

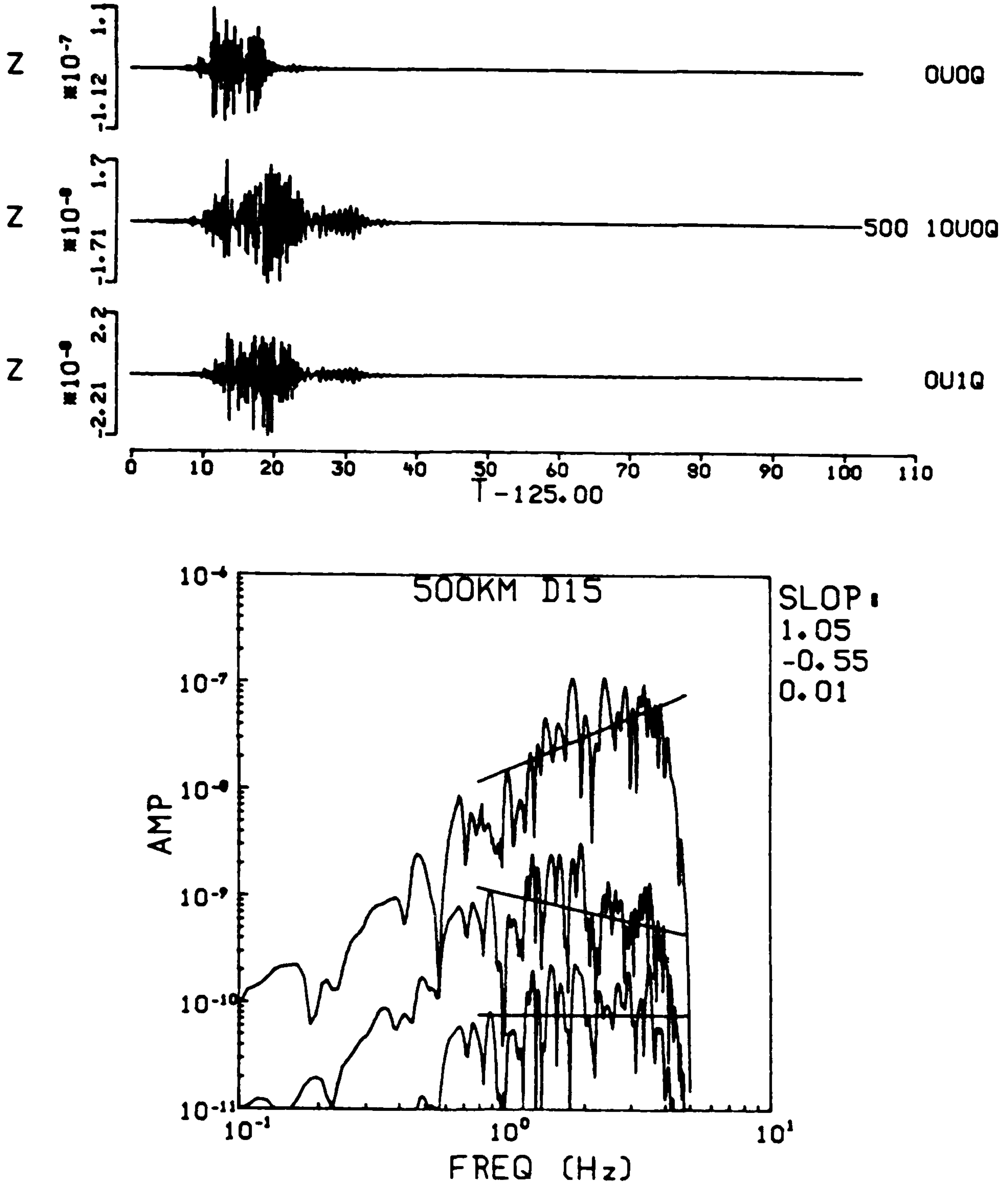
Z
x10-7
1.1
-1.12
0U0Q
Z
x10-8
1.7
-1.71
500 10U0Q
Z
x10-8
2.2
-2.21
0U1Q
0
10
20
30
40
50
60
70
80
90
100
110
T-125.00
500KM D15
SLOP:
1.05
-0.55
0.01
AMP
10-6
10-7
10-8
10-9
10-10
10-11
10-1
10^0
10^1
FREQ (Hz)

Figure 7b.

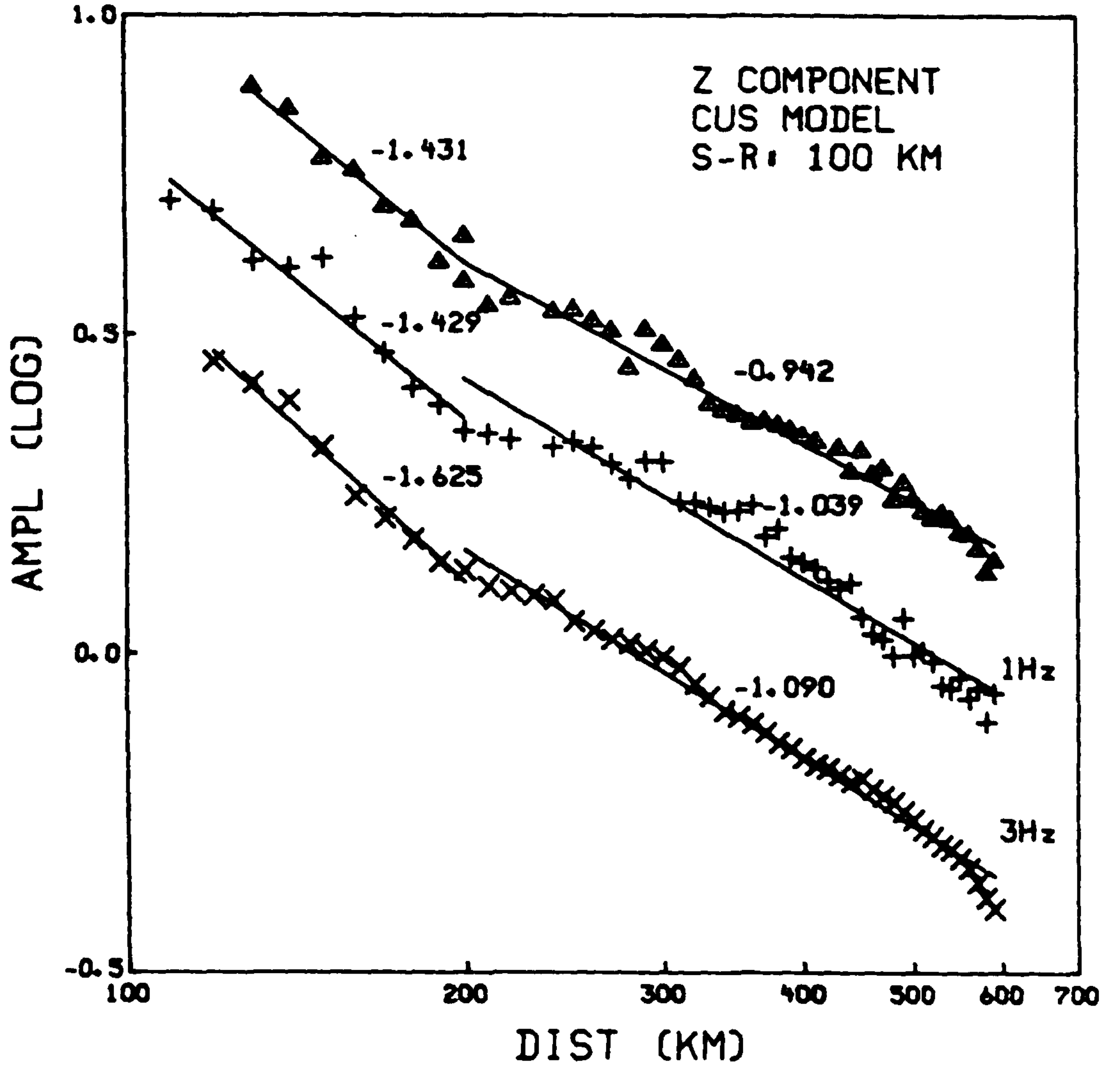

Figures 8. The geometrical spreading factor for scattering waves in the layered medium. Displays are for Z component (a) and SH component (b) with epicentral distance at 100 km in CUS model. The scattering distance varies from 110 km to 600 km. The top curve is from the average peak-to-peak amplitude of composed scattering waveforms, and the lower two curves are for amplitudes after narrow bandpass filtering at at 1 Hz and 3 Hz respectively. No Q has been applied. Because of mode conversion, we can see much faster amplitude decay in the front part (<200km). The slopes of piecewise linear segments fit to the data are shown.

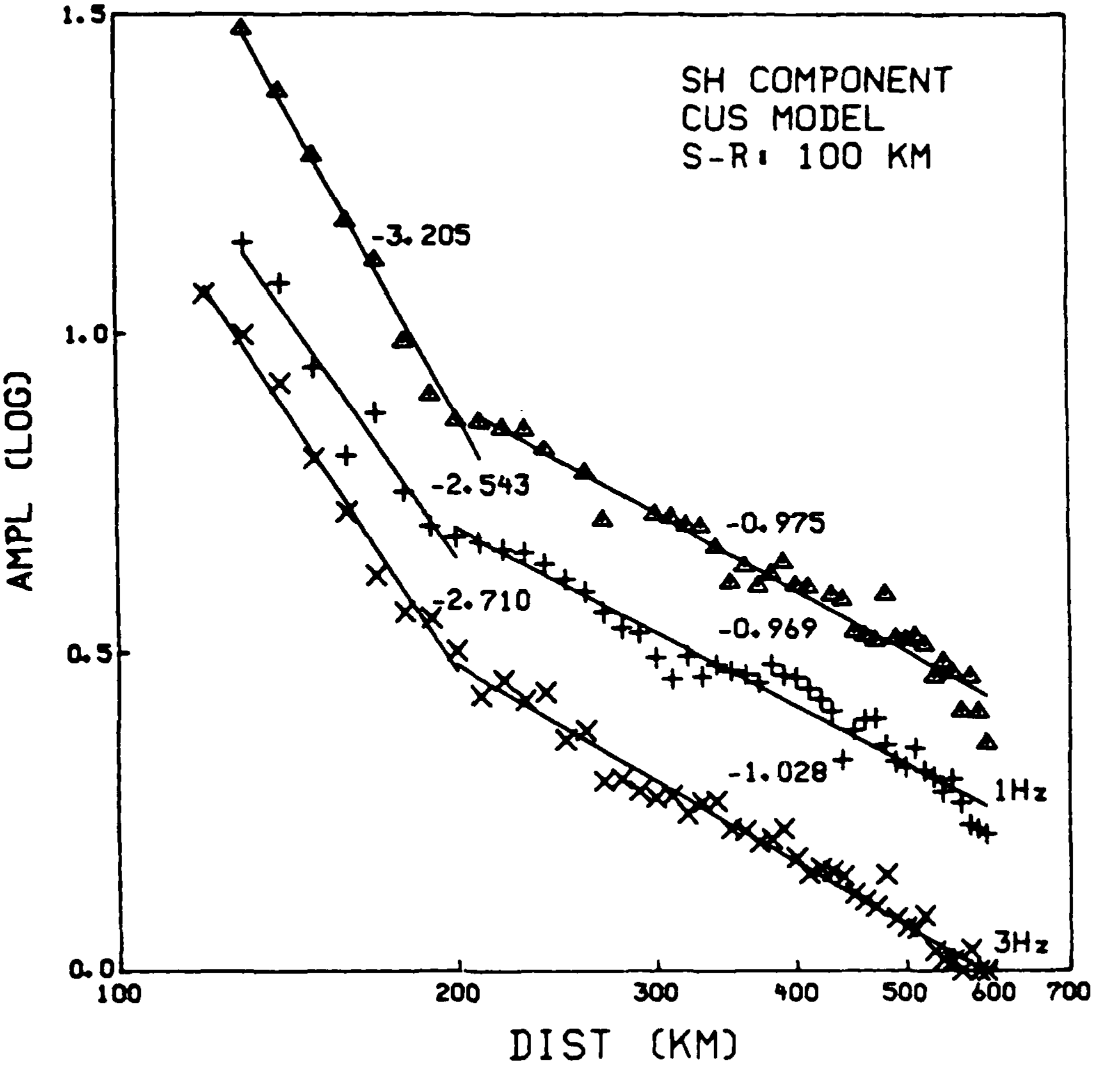
SH COMPONENT
CUS MODEL
S-R: 100 KM
-3.205
-2.543
-2.710
-0.975
-0.969
-1.028
1Hz
3Hz
AMPL (LOG)
DIST (KM)
1.5
1.0
0.5
0.0
100
200
300
400
500
600
700

Figure 8b.

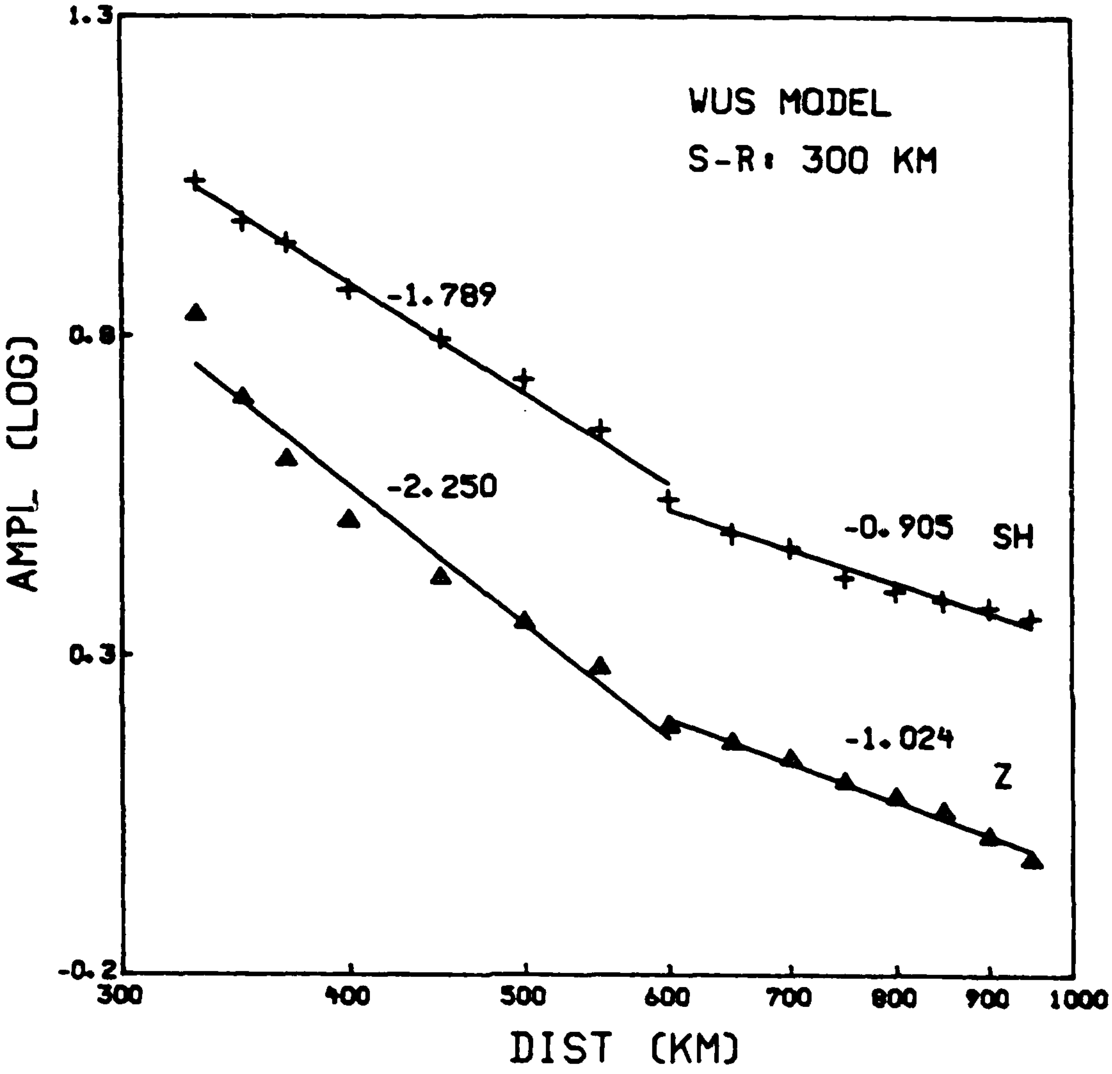
WUS MODEL
S-R: 300 KM
-1.789
-2.250
-0.905
SH
-1.024
Z
1.3
0.8
0.3
-0.2
300
400
500
600
700
800
900
1000
AMPL (LOG)
DIST (KM)

Figure 8c.

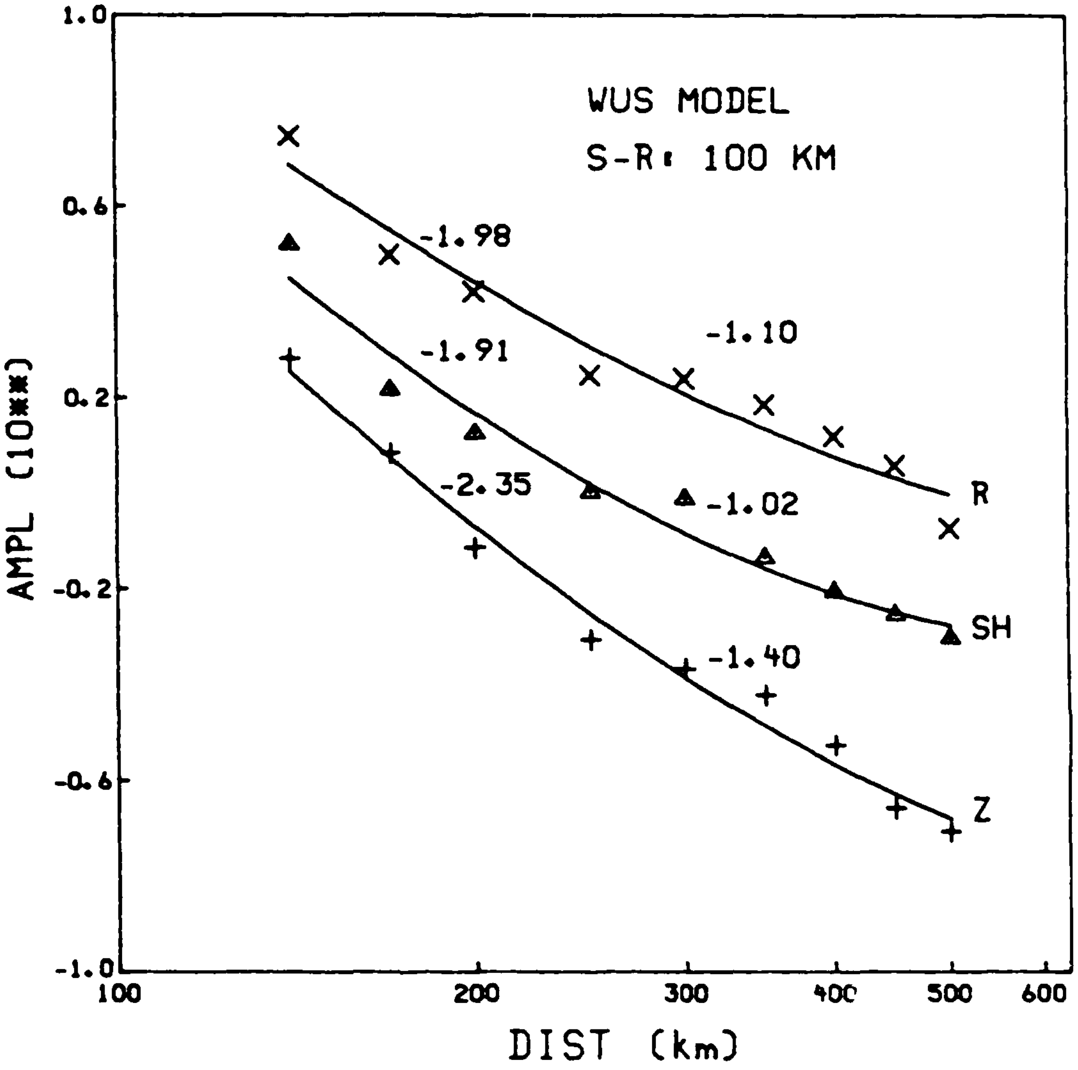

Figure 9. Scattering geometrical spreading in the WUS model. Two components, vertical and tangential, are displayed. (a) is for source -receiver distance at 300 km and (b) at 100 km. Note that the slope changes at 600 km for (a) and at 200 km for (b). The WUS model has more rapid geometrical decay rate than the CUS model. The slope difference between the two regions is also larger.

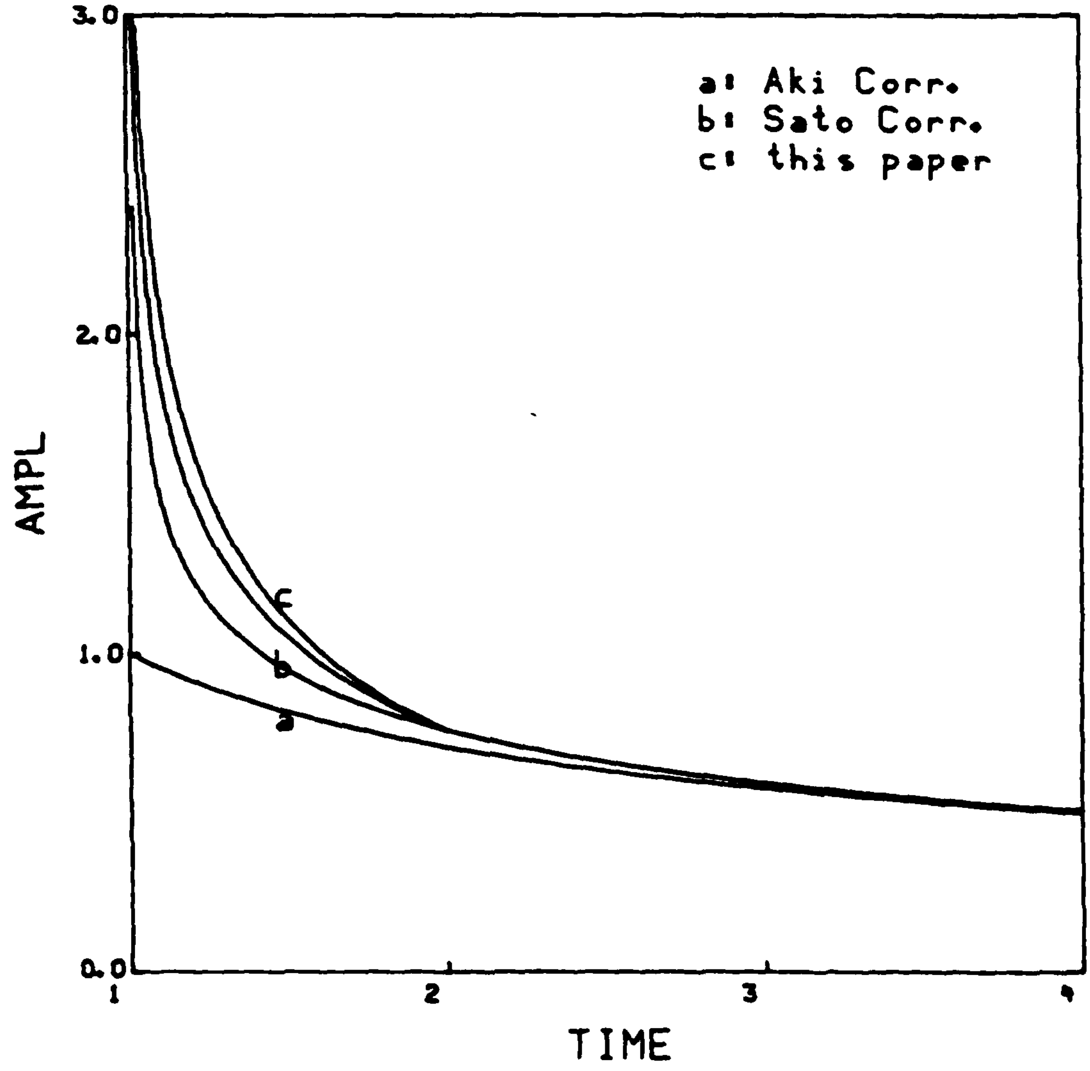

Figure 10. A modification of geometrical spreading correction of Sato's surface-wave scattering model. A higher decay rate of $t^{-0.5}$ to t^{-1} due to mode conversion and wave-type conversion is assumed for the lapse time ratio smaller than 2.

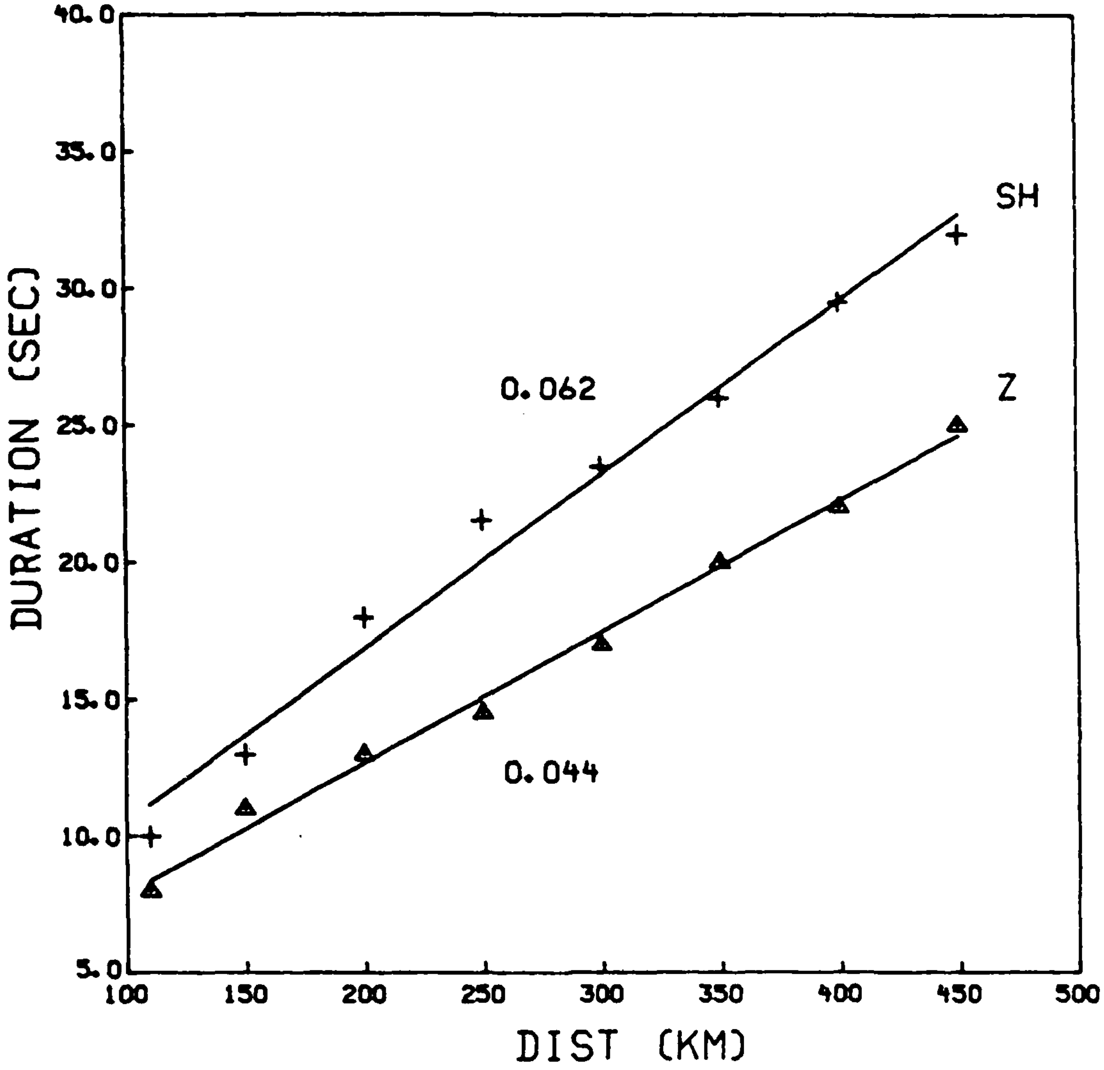

Figure 11. Duration of scattering pulse at different distances. A Q model 10U1Q in CUS model has been applied. The upper and lower sets of data are from SH and Z synthetics, respectively. An average duration expansion rate 0.05 with distance is obtained.

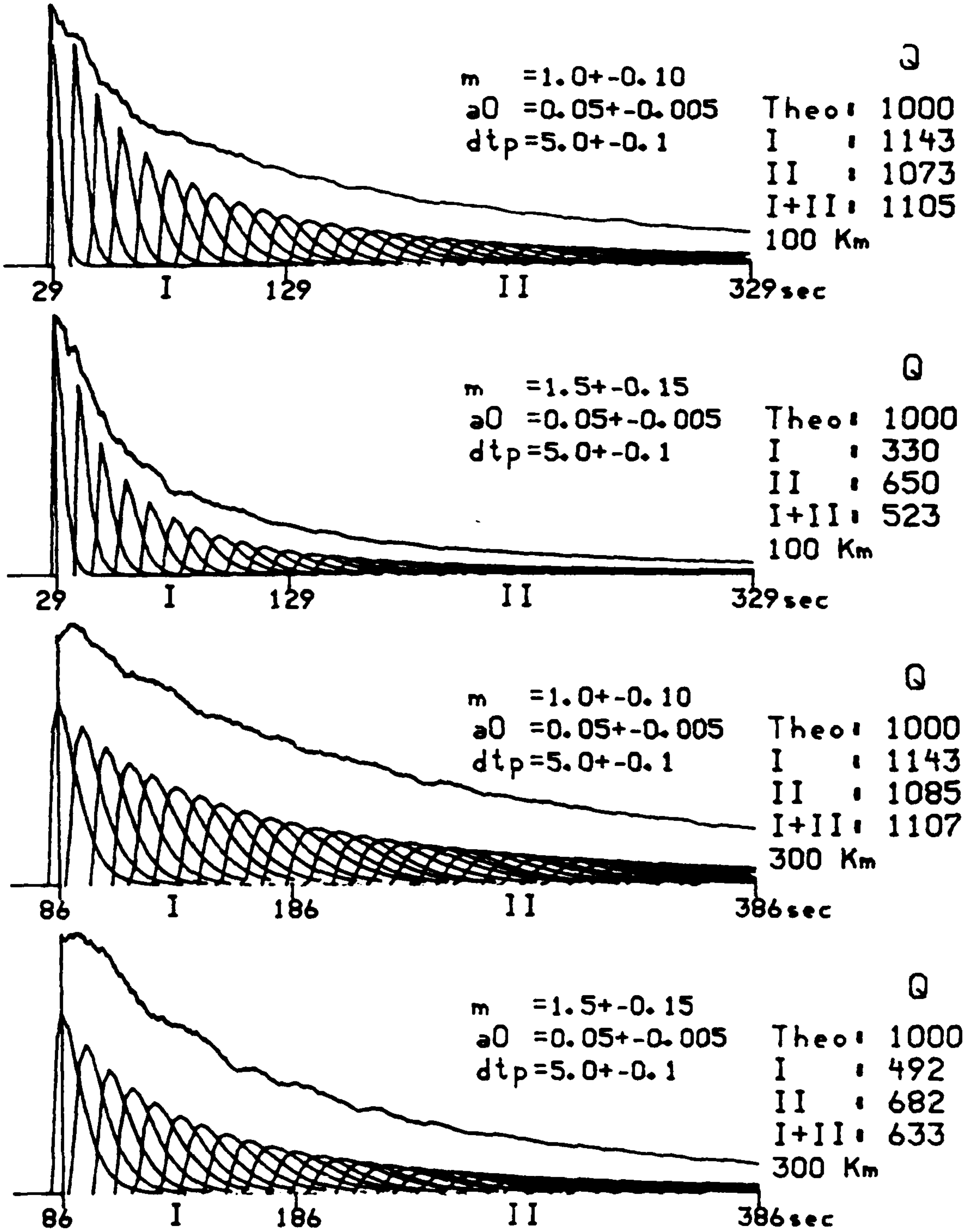

Figure 12. Superposition of scattering pulses to form the coda envelope. The part (a) simulates the eastern United States case. Spreading factor m largely affects the coda decay. Also note that the analysis of first part (I) and the rest (II) yields different apparent Q values. The part (b) simulates the western United States case. Since the pulse superposition has been saturated by the rapid decay due to Q, the inferred Q is not dependent upon the shape factors of the individual scattered pulses much.

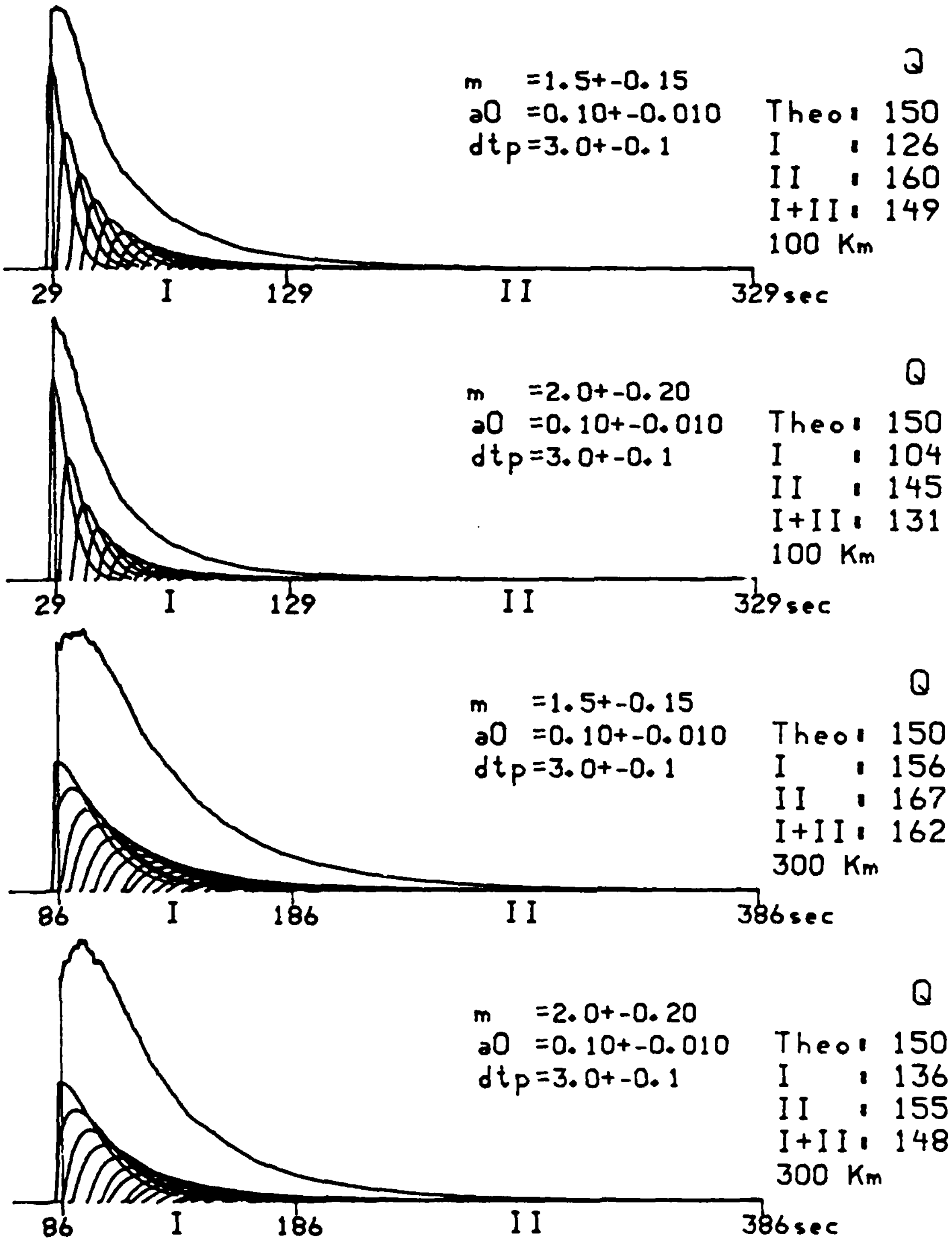
m =1.5+-0.15
a0 =0.10+-0.010
dtp=3.0+-0.1
Q
Theo: 150
I : 126
II : 160
I+II: 149
100 Km
29
I
129
II
329sec
m =2.0+-0.20
a0 =0.10+-0.010
dtp=3.0+-0.1
Q
Theo: 150
I : 104
II : 145
I+II: 131
100 Km
29
I
129
II
329sec
m =1.5+-0.15
a0 =0.10+-0.010
dtp=3.0+-0.1
Q
Theo: 150
I : 156
II : 167
I+II: 162
300 Km
86
I
186
II
386sec
m =2.0+-0.20
a0 =0.10+-0.010
dtp=3.0+-0.1
Q
Theo: 150
I : 136
II : 155
I+II: 148
300 Km
86
I
186
II
386sec

Figure 12b.

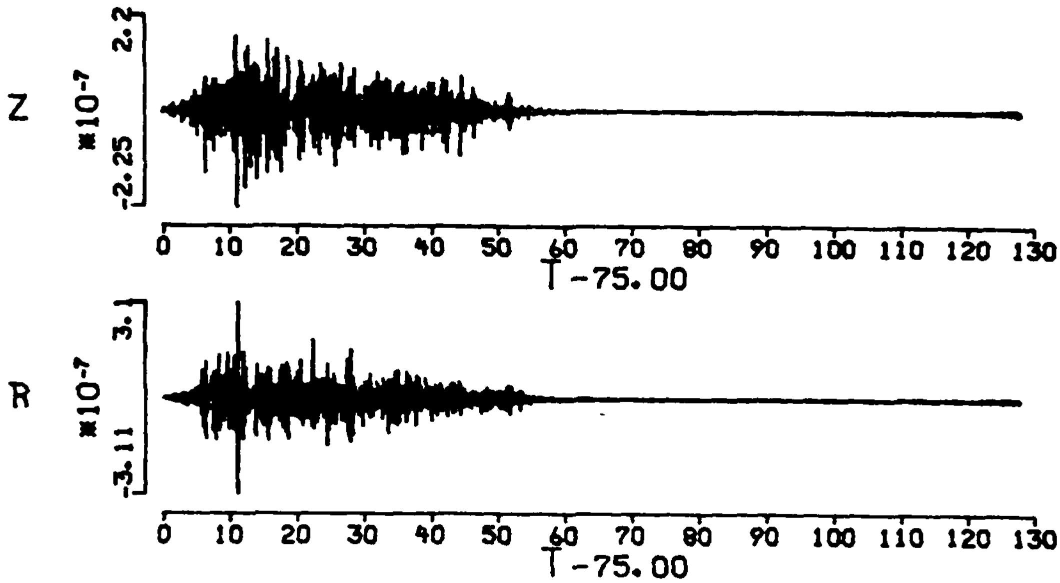

Figure 13. Coda synthetics after summing over 100 scattered pulses which are from scatterers distributed evenly between scatterer distances 300 km and 400 km. A Q model 10U1Q has been applied. The decay of the coda follows the shape predicted by the pulse summation.

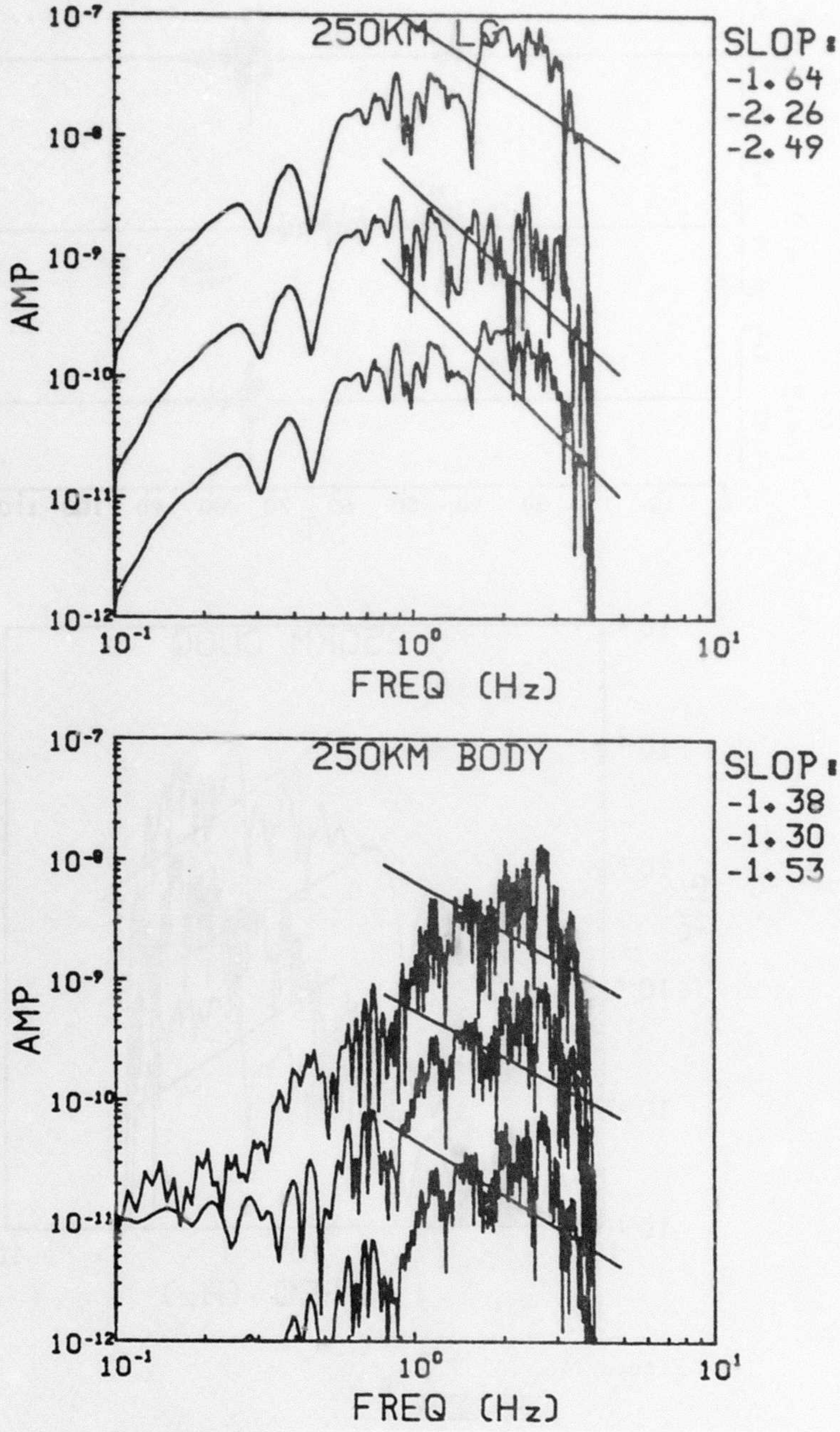

Figure 14. The spectra of body-wave and surface-wave scattered pulses. (a), (b), and (c) are for three different attenuation conditions. Three traces in each plot are for complete, body-wave only, and surface-wave only. The spectra of surface-wave only is shifted down by a factor of 100 for clarity. Note that the frequency content is similar (see (a)) for body- or surface-wave scattering if no Q effect is included. (b) shows the case under scattering attenuation. The attenuation of body-wave scattered waveforms is less than the surface-wave scattered arrivals. (c) is for the intrinsic Q. Again, the body wave scattering shows stronger resistance to attenuation.

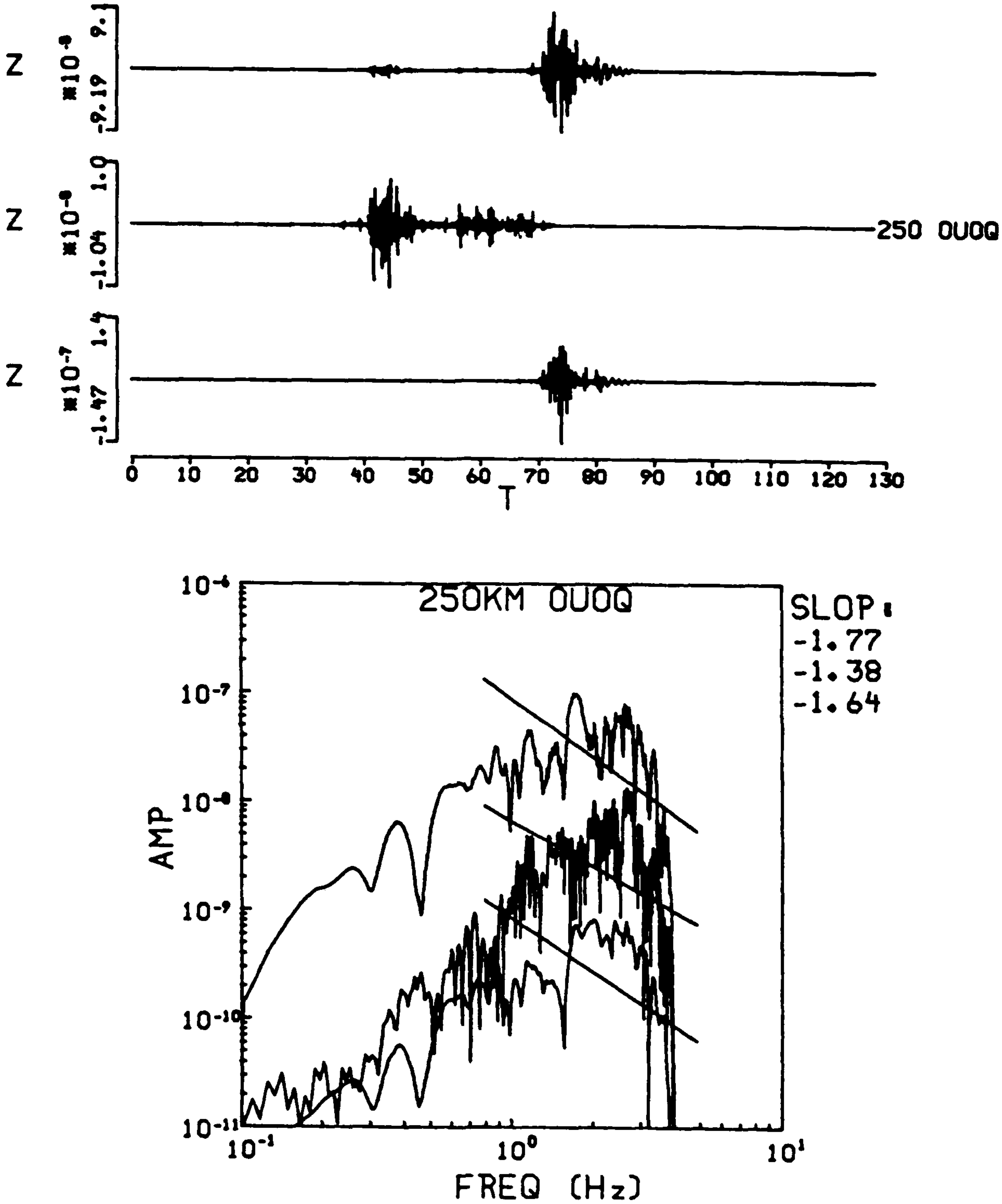
Z
*10-8
9.1
-9.19
Z
*10-8
1.0
-1.04
250 OUOQ
Z
*10-7
1.4
-1.47
0
10
20
30
40
50
60
70
80
90
100
110
120
130
T
250KM OUOQ
SLOP:
-1.77
-1.38
-1.64
AMP
10-6
10-7
10-8
10-9
10-10
10-11
10-1
10^0
10^1
FREQ (Hz)

Figure 14b.

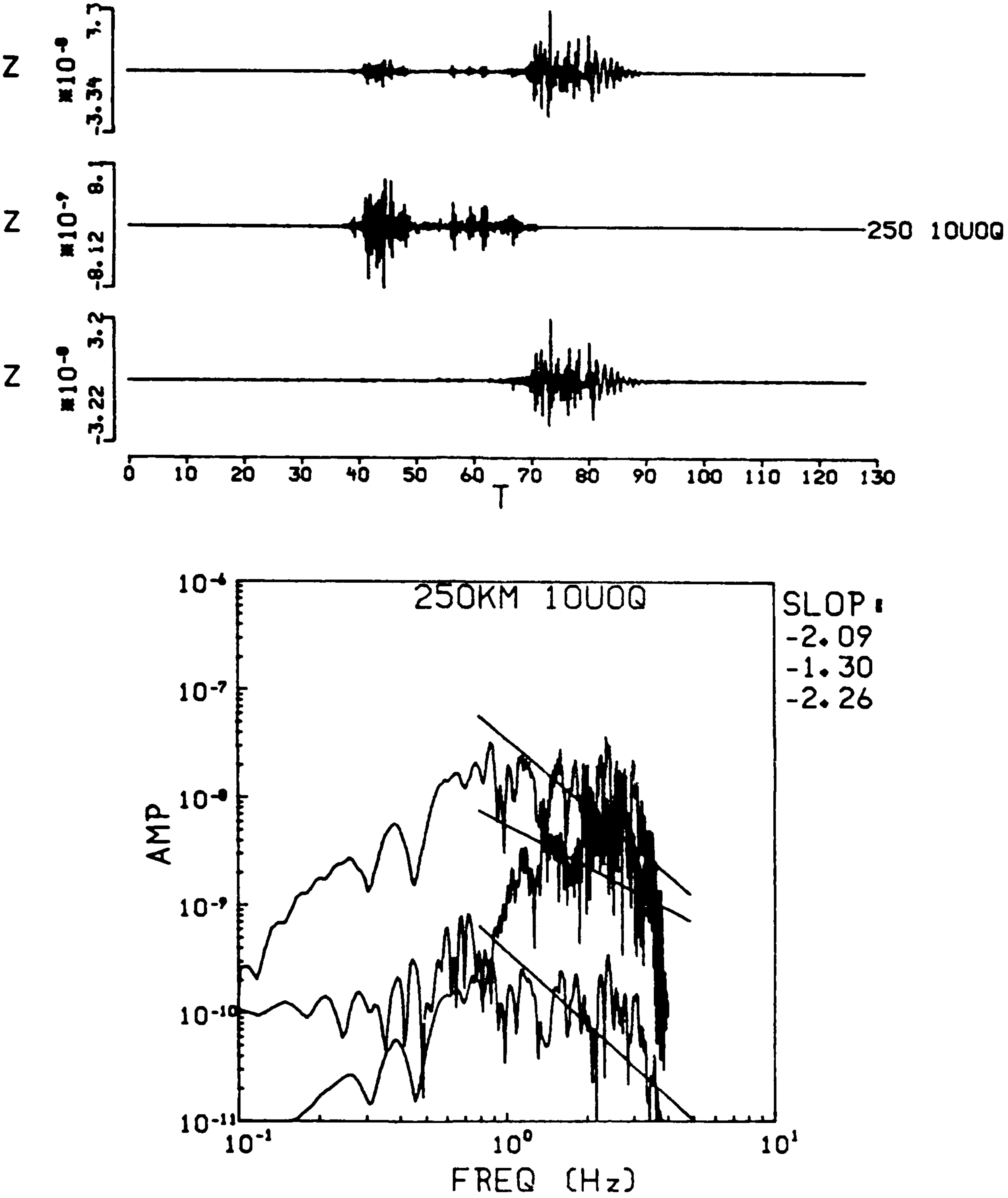
Z
×10-8
-3.34
7.
Z
×10-9
-8.12
8.1
250 10UOQ
Z
×10-8
-3.22
3.2
0
10
20
30
40
50
60
70
80
90
100
110
120
130
T
250KM 10UOQ
SLOP:
-2.09
-1.30
-2.26
AMP
10-6
10-7
10-8
10-9
10-10
10-11
10-1
100
101
FREQ (Hz)

Figure 14c.

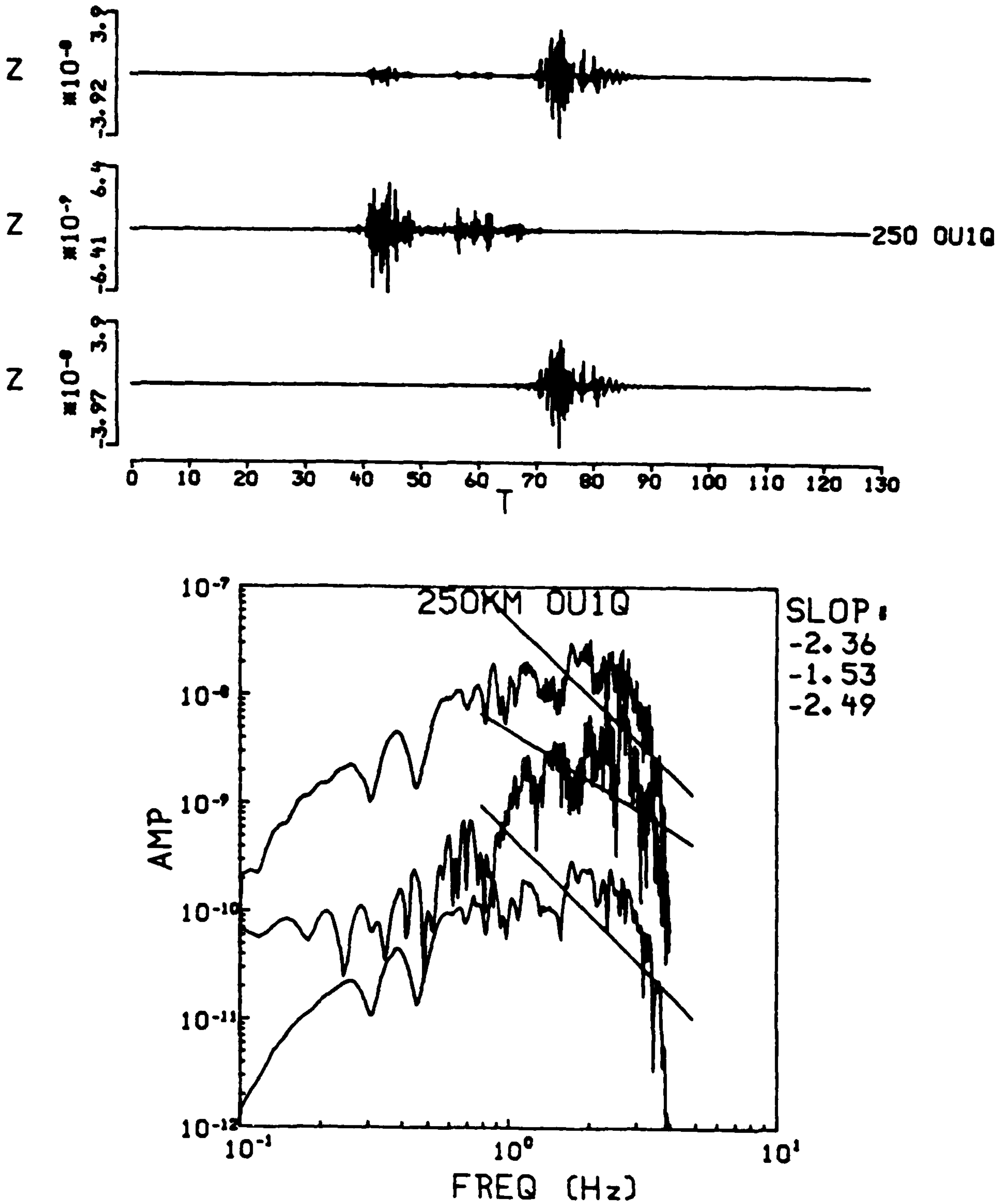

Figure 15. The decay of high frequency component under different attenuation conditions for surface-wave and body-wave scattering for a scattering distance of 250 km.. The body-wave scattering shows much smaller attenuation compared to surface-wave scattering attenuation. This may explain much higher frequencies are observed from P-coda or S-coda. Each spectrum has been shifted by a factor of ten for clarity.

APPLICATION OF FREQUENCY VARIABLE FILTERS TO SURFACE-WAVE AMPLITUDE ANALYSIS

By David R. Russell, Robert B. Herrmann, and Horng-Jye Hwang

ABSTRACT

The problem of spectral biasing due to frequency domain filtering of surface-wave seismograms is investigated, and the method of frequency variable filters (FVF) is developed to compensate for this bias. As a result, the FVF can significantly improve signal to noise in the filtering process, except at points which require increased frequency domain resolution due to biasing. A detailed comparison of some currently accepted surface-wave filters is made, in order to clarify the development of the FVF algorithm. Three long period surface-wave seismograms are tested with FVF and compared to two other methods, the multiple filter technique (MFT) and the phase matched filter (PMF). Emphasis is placed on finding limitations in all the methods, not on routine processing. Results of the tests show that the FVF and PMF are an improvement over MFT, in that the results of processing can be diagnosed in both the time and frequency domains. In addition, the FVF is more successful than PMF in removing higher mode contamination from fundamental mode Rayleigh waves. Another conclusion is that care must be taken in defining the limits of frequency domain resolution for the FVF. Some bias due to convolutional smoothing must be accepted, or the FVF becomes a simple all-pass filter. MFT and PMF have a similar problem, which is due fundamentally to the uncertainty principle between time and frequency.

Introduction

Recently, attention has been focused on the problem of filtering seismograms to isolate propagating normal modes, especially in the context of determining spectral amplitudes for nuclear yield estimation. Using the multiple filter technique (MFT) (Dziewonski *et al.*, 1969), Yacoub (1983) determined average spectral amplitudes around the 20 second period. Herrin and Goforth (1977) developed the phase-matched filter (PMF) to refine group and phase velocities of normal modes, and Stevens (1986a) used this method to isolate fundamental mode spectra across the entire observed bandwidth. Hwang and Mitchell (1986) used the time-variable filter (TVF) developed by Landisman *et al.* (1969) to isolate spectral amplitudes for inter-station Green's functions. Russell *et al.* (1986) combined the PMF and TVF methods to form a frequency-variable filter (FVF), in order to improve spectral amplitude estimates of explosion generated waveforms.

This paper will extend the FVF method in order to reduce problems of spectral biasing, and will discuss in some detail relationships between the above filters.

General theory

For surface-wave studies, the objective is to process s(t), the raw surface-wave time history, by a series of convolutional filters designed for modal isolation. In the context of this discussion, the definition of "convolution" is extended to include the general case of frequency varying filters, which have a changing bandwidth during the convolution operation. This will produce a time trace (or frequency spectrum) which can be used for further analysis.

Most surface-wave filters can be expressed by the following relations:

$$\psi(t) = \frac{1}{2\pi} \int_{-\infty}^{\infty} P_j(\omega)\, W_\tau(t,\omega)\, S(\omega)\, e^{i\omega t} d\omega \tag{1}$$

$$h(t) = \frac{1}{2\pi} \int_{-\infty}^{\infty} H(\omega-\omega_0)\, \Psi(\omega)\, e^{i\omega t} d\omega \tag{2}$$

$$s_j(t) = \frac{1}{2\pi} \int_{-\infty}^{\infty} P_j^{-1}(\omega)\, \Psi(\omega)\, e^{i\omega t} d\omega \tag{3}$$

where $\Psi(\omega) =$ Fourier transform of $\psi(t)$.

$$S(\omega) = \sum_j |S_j(\omega)|\, e^{-ik_j(\omega)x} + N(\omega)$$

$$P_j(\omega) = e^{i\tilde{k}_j(\omega)x}, \quad P_j^{-1}(\omega) = e^{-i\tilde{k}_j(\omega)x}$$

$S(\omega)$ is the total spectrum of the seismogram, composed of a sum of normal modes and an additive component $N(\omega)$, corresponding to multi-pathed signals, interfering events, and incoherent noise. The purpose of the above filters is to isolate the j'th mode of interest so the amplitude spectrum $|S_j(\omega)|$ and wavenumber spectrum $k_j(\omega)$ can be recovered, with the understanding that the spectra may contain both source and path contributions. This is probably too idealistic a goal in some cases, as pointed out by Der (1986). Due to scattering and reflections, there may not be a pure isolated mode to recover. A more accurate statement is that the purpose of such filters is to isolate seismic energy propagating in the vicinity of desired modes of interest.

$P_j(\omega)$ is a phase-matched filter. The wavenumber estimate $\tilde{k}_j$ should be near the true modal wavenumber, in order to compress the energy of the desired signal about zero-lag in the time domain, forming a "pseudo-autocorrelation function" $\psi(t)$. Herrin and Goforth (1977) discussed this in detail.

$W_\tau(t,\omega)$ is a time and frequency variable window used to isolate modes of interest and improve signal to noise ratios. It is symmetric about position τ in the time domain, with a width controlled by the frequency ω.

$H(\omega-\omega_0)$ is a frequency domain convolution filter, used to isolate the energy of propagating normal modes in multiple filter analysis.

Review of surface-wave applications

Various combinations of the above filters have been used for modal isolation, four of which will be discussed in detail below.

Case 1: $P(\omega) \equiv 1$, $W_\tau(t,\omega) \equiv 1$. This is the basis for the multiple filter technique (MFT) (Dziewonski *et al.* , 1969). In this case $\Psi(\omega) = S(\omega)$, so the raw spectrum $S(\omega)$ is input into (2), which is the MFT evaluated at ω_0. $H(\omega-\omega_0)$ is a narrow bandpass filter (usually a band-limited Gaussian), symmetric about ω_0. The symmetry about positive frequencies causes the time signal $h(t)$ to be complex, with the modulus having maxima at the group velocities of the signal modes. Herrmann (1973) showed that under the condition of an approximately flat amplitude spectrum and linear phase delay of the j'th mode across the width of $H(\omega-\omega_0)$,

$$h(t) = \frac{\omega_0 \pi^{1/2}}{2\pi\alpha^{1/2}} \sum_j |S_j(\omega_0)| \exp[i(\omega_0 t - k_j(\omega_0)x)] \exp\left[-\frac{\omega_0^2}{4\alpha}(t-t_j)^2\right] \tag{4}$$

where α is a constant controlling the width of the Gaussian filter, and t_j is the group delay of the j'th mode. Evaluating (4) at multiple frequencies will extract the spectrum of the j'th mode, if it is suitably smooth.

Case 2: $W_\tau(t,\omega) \equiv 1$. This is the basis for the "residual dispersion" technique of Dziewonski *et al.* (1972). The MFT is first applied to determine wavenumber estimates from the instantaneous phases of (4), in order to construct the phase-matched filter $P(\omega)$.

Equation (1) now represents the seismogram with the dispersion removed from the j'th mode. The signal is Fourier transformed and the MFT applied again (2). This method was introduced to remove biasing caused by the signal phase in MFT due to dispersion.

Case 3: $P(\omega) \equiv 1$, $W_r(t,\omega) = W_{t_j(\omega)}(t,\omega)$. This is the time-variable filter due to Landisman *et al.* (1969). MFT is performed first to determine group delays $t_j(\omega)$, and the window W_r is symmetrically centered about the group delay in equation (1). The width of the window is a multiple of the period of interest. ψ (t) should therefore contain only energy associated with the mode of interest, and so (1) will be equivalent to the time domain signal of the isolated mode.

Case 4: $W_r(t,\omega) = W_0(t)$. This is the phase-matched filter method of Herrin and Goforth (1977). MFT is performed first to estimate wavenumbers for the phase-matched filter $P(\omega)$. This differs from the residual dispersion technique (case 2), in that the phase of the signal is found by integrating the group delay calculated in MFT. The window $W_0(t)$ is no longer frequency dependent, so it can be factored from the integral in (1). In the time domain $W_0(t)$ is centered about zero-lag, and should isolate the energy of the desired mode of interest. In the frequency domain, (1) will be a true convolution of the pseudo-autocorrelation spectrum with the frequency equivalent of $W_0(t)$. Equation (3) is the time domain signal of the isolated mode.

All of the above methods attempt to isolate spectral modes of interest via frequency domain convolutions. As Dziewonski and Hales (1972) pointed out, the process of convolution will distort the signal spectrum unless the prescribed filters are Dirac impulses in the frequency domain. The process of residual dispersion (case 2), or phase-matched filtering (case 4) can minimize phase distortion, but they do not address the problem of amplitude distortion, or bias due to the convolution operation.

FVF theory

Let $W_r(t,\omega) = W_0(t,\omega)$. This defines the method of frequency variable filtering (FVF). It combines the beneficial aspects of a time-variable filter (TVF) and a phase-matched filter (PMF), and allows the analyst to place maximum error bounds on the amount of tolerable amplitude bias. The raw spectrum $S(\omega)$ is phase-matched filtered to compress the energy of the signal of interest about zero-lag in the time domain. Then, each harmonic component of this pseudo-autocorrelation function is windowed about zero-lag with $W_0(t,\omega)$, with the width of the window proportional to the period of the individual harmonic. These operations are done in equation (1), which is then Fourier transformed for the phase-matched spectrum of interest. Equation (3) replaces the phase removed in (1) to give the time domain signal of the isolated mode. The technique is quite similar to the time-variable filter (case 3), except that the phase of the mode of interest is first removed to minimize spectral distortions due to phase fluctuations. It should be noted that in the context of residual dispersion measurements, this method was first recommended by Dziewonski and Hales (1972).

An advantage of FVF is that the time window $W_0(t,\omega)$ can be constructed at each frequency to control the amount of bias due to windowing. The exact form of the window will be defined below, but first a discussion of the problem of biasing is presented.

In calculating equation (1), it is assumed that the window $W_r(t,\omega)$ does not distort the spectrum of the j'th mode. This is not true in practice, and the purpose of this section is to approximately calculate the bias in the frequency domain due to time domain windowing. The analysis is similar to Jenkins and Watts (1968, p. 247). From equation (1), define the signal pseudo-autocorrelation function as a phase-matched single-mode signal uncontaminated by noise:

$$\psi_j(t) = \frac{1}{2\pi} \int_{-\infty}^{\infty} |S_j(\omega)| \, e^{i\delta k(\omega) x} \, e^{-i\omega t} d\omega \tag{5}$$

where

$$\delta k(\omega) = \hat{k}_j(\omega) - k_j(\omega)$$

is the residual wavenumber left from the phase-matched filter process. The bias in the frequency domain will be the transformed difference between the windowed signal pseudo-autocorrelation function and (5):

$$B(\omega) = \int_{-\infty}^{\infty} [W_0(t) - 1]\, \psi_j(t)\, e^{-i\omega t} dt. \tag{6}$$

Two windows are examined for bias: the cosine and Parzen (also called de la Valle - Poisson) windows. The cosine window is defined as:

$$W_0^c(t) = \begin{cases} \cos(\pi t/2T) & |t| \leq T \\ 0 & |t| > T \end{cases} \tag{7}$$

where T is the one-sided width of the cosine window. The maximum sidelobe level for the cosine window is -23 dB (7 percent) of the main lobe (Harris, 1978). The Parzen window is defined as:

$$W_0^p(t) = \begin{cases} 1 - 6(t/T)^2 + 6(|t|/T)^3 & |t| \leq T/2 \\ 2(1 - |t|/T)^3 & T/2 < |t| \leq T \\ 0 & |t| > T \end{cases} \tag{8}$$

where T is the one-sided width of the Parzen window. The maximum sidelobe level for the Parzen window is -53 dB (0.2 percent) of the main lobe (Harris, 1978). For a given width T, the Parzen window is a much smoother convolutional filter in the frequency domain due to low sidelobes.

To calculate the approximate bias, substitute the windows into (6) and keep terms only on the order of $1/T^2$ or more. For the cosine window,

$$B^c(\omega) = \frac{\pi^2}{8T^2} \int_{-\infty}^{\infty} -t^2\, \psi_j(t)\, e^{-i\omega t}\, dt \quad + \quad O(1/T^4) \tag{9}$$

and the Parzen window,

$$B^p(\omega) = \frac{6}{T^2} \int_{-\infty}^{\infty} -t^2\, \psi_j(t)\, e^{-i\omega t}\, dt \quad + \quad O(1/T^3)\,.$$

Notice that the infinite limits are kept for the integrals. This is under the assumption that T is wide enough to insure an insignificant truncation of the signal pseudo-autocorrelation function, resulting in a negligible signal outside the limits +T, −T . Making use of Fourier transform properties of differentiation (Papoulis, 1962, p. 16) gives

$$B^c(\omega) = \frac{\pi^2}{8T^2} \Psi_j''(\omega)\,, \quad B^p(\omega) = \frac{6}{T^2} \Psi_j''(\omega) \tag{10}$$

where the double primes indicate the second derivative with respect to angular frequency of the signal pseudo-autocorrelation spectrum. Taking the ratio of B^p to B^c shows that the Parzen window has almost five times the bias of the cosine window, which suggests that it may be a poor choice for a windowing function. However, further investigation of the spectral second derivative yields interesting results.

From equation (5), the spectrum of the signal pseudo-autocorrelation function is

$$\Psi_j(\omega) = |S_j(\omega)| \, e^{i\delta k(\omega) x} = \alpha e^{i\theta} . \tag{11}$$

The terms α and θ are chosen for notational convenience. Calculating the second derivative of the signal pseudo-autocorrelation spectrum gives

$$\Psi_j''(\omega) = [\alpha'' - \alpha(\theta')^2]e^{i\theta} + [\alpha\theta'' + 2\alpha'\theta']e^{i(\theta + \pi/2)} . \tag{12}$$

If the phase-matched filter is successful, the difference between the estimate and true wavenumber (δk) should approach zero. Therefore, keeping only first order residual phase terms for θ, θ', and θ'', the Parzen window amplitude bias is

$$B^{p\alpha} = \frac{6}{T^2} \alpha'' \tag{13}$$

and the phase bias is

$$B^{p\theta} = \frac{6(\alpha\theta'' + 2\alpha'\theta')}{T^2\alpha + 6\alpha''} . \tag{14}$$

A similar expression for the cosine window amplitude bias is

$$B^{c\alpha} = \frac{\pi^2}{8T^2} \alpha'' \tag{15}$$

and for phase bias,

$$B^{c\theta} = \frac{\pi^2(\alpha\theta'' + 2\alpha'\theta')}{8T^2\alpha + \pi^2\alpha''} . \tag{16}$$

Equation (14) and (16) show that the bias in phase is independent of constant phase values, and that if the first and second derivatives are small, the phase bias will also be small. Therefore, it is advisable to use smooth (low sidelobe) windows such as the Parzen for calculating residual phases in the matched filtering process. However, it should be clear that spectral amplitudes may be quite biased when there is significant curvature in the amplitude spectrum, corresponding to a large spectral second derivative, α''. Examples of this are narrow band spectra and the vicinity of sharply changing band edges. The fact that phase-matched filtering is an iterative process can reduce residual bias in phase, but this will not help the bias in the amplitude spectrum, since it is to first order independent of phase.

To implement the FVF algorithm, first note that the Ψ_j'' term in equation (10) corresponds to the true signal pseudo-autocorrelation function, which is unknown. However, with the same analysis used to calculate (9), it can be directly shown that

$$B^c(\omega) = \frac{\pi^2}{8T^2} \Psi_j^{p\,''}(\omega) + O(1/T^4) \tag{17}$$

where the superscript " p " indicates the second derivative of the Parzen windowed pseudo-autocorrelation function defined by (1). This is under the assumption that the effect of noise on the windowed function is negligible, which is not unreasonable since the Parzen window width used for phase processing can be relatively narrow (see (14) above). However, care should be taken in using the algorithm for seismograms with extremely high random noise levels.

Define the maximum tolerable bias error relative to the maximum signal amplitude as

$$E_{max} = \frac{|B|_{max}}{|\Psi_j^p|_{max}} \, . \tag{18}$$

For the cosine window, substitute (18) into (17) and solve for T, the one-sided width of the window:

$$T(\omega) = \left[\frac{\pi^2}{8E_{max}} \; \frac{|\Psi_j^{p\,\prime\prime}(\omega)|}{|\Psi_j^p|_{max}} \right]^{\frac{1}{2}} \tag{19}$$

Notice that the width is now frequency dependent. Equation (19) defines the "curvature correction" for reducing bias in the FVF. To account for zero-crossings of the second derivative, let

$$T^c(\omega) = \max\left\{ \frac{2\pi C}{\omega} \, , \, T(\omega) \right\} \tag{20}$$

where C is a constant multiple of the period of interest. Using equations (7) and (20), the instantaneous cosine window for the FVF algorithm is defined as

$$W_o^c(t,\omega) = \begin{cases} \cos\left[\pi t / 2T^c(\omega)\right] & |t| \le T^c(\omega) \\ 0 & |t| > T^c(\omega) \, . \end{cases} \tag{21}$$

The FVF algorithm can now be formally developed as follows.

FVF algorithm

Step 1. Using Herrin and Goforth's iterative phase-matched filter process (1977), isolate the mode of interest with a Parzen windowed pseudo-autocorrelation function

$$\psi_j^p(t) = \frac{1}{2\pi} \int_{-\infty}^{\infty} P_j(\omega) \, W_o^p(t) \, S(\omega) \, e^{i\omega t} d\omega \; . \tag{22}$$

and save the final wavenumber estimate used in the phase-matched filter

$$P_j(\omega) = e^{ik_j(\omega)x} \; . \tag{23}$$

Step 2. From equation (22), calculate the spectrum of the windowed mode

$$\Psi_j^p(\omega) = \int_{-\infty}^{\infty} \psi_j^p(t) \, e^{-i\omega t} dt \tag{24}$$

and its second derivative

$$\Psi_j^{p\,\prime\prime}(\omega) = \int_{-\infty}^{\infty} -t^2 \, \psi_j^p(t) \, e^{-i\omega t} dt \tag{25}$$

Substitute equations (24) and (25) into (19) for the instantaneous window width $T^c(\omega)$.

Step 3. Calculate the corrected pseudo-autocorrelation function and its spectrum, using the phase-matched filter (23) and the instantaneous cosine window (21):

$$\psi_j(t) = \frac{1}{2\pi} \int_{-\infty}^{\infty} P_j(\omega)\, W_0^c(t,\omega)\, S(\omega)\, e^{i\omega t} d\omega \tag{26}$$

$$\Psi_j(\omega) = \int_{-\infty}^{\infty} \psi_j(t)\, e^{-i\omega t} d\omega \ . \tag{27}$$

Step 4. Using the phase-matched filter (23) and the corrected pseudo-autocorrelation spectrum (27), calculate the corrected spectrum of the isolated mode:

$$S_j(\omega) = \Psi_j(\omega)\, e^{-i\tilde{k}_j(\omega)\, x} \ . \tag{28}$$

Taking the inverse Fourier transform of (28) gives the isolated mode in the time domain, as in equation (3).

Examples and discussion

Three seismic events were chosen to illustrate various aspects of the FVF algorithm and its relation to other convolutional type filters. For comparison, MFT and PMF were also applied to the events. The MFT (3) was constructed with a Gaussian filter

$$H(\omega) = \begin{cases} \exp(-\alpha\, \omega^2/\omega_0^2) & |\omega| \le \omega_c \\ 0 & |\omega| > \omega_c \end{cases} .$$

The Gaussian cutoff frequency ω_c and the filter width parameter α were constructed with values found in Dziewonski *et al.* (1969) and Herrmann (1973),

$$\omega_c = \omega_0/4 \qquad \alpha = 16\pi \ .$$

The residual dispersion method (Case 2) was not incorporated into the MFT, in order to illustrate the effects of phase distortion.

The PMF was implemented using the algorithm developed by Herrin and Goforth (1977). The Parzen window (8) was used for phase processing, and the cosine window (7) was used to extract the amplitude spectrum. The one-sided window width was set to a default value of 1.5 times the maximum period found by MFT analysis.

The FVF was constructed using the algorithm developed above. Parameters E_{max} and C in (18) and (20) were set to

$$E_{max} = .035 \qquad C = 2.5 \ .$$

This defines a minimum one-sided cosine window width of 2.5 times the period of interest, and a maximum bias error of 3.5% . As stated above, some error must be tolerated in the filtering process. Setting $E_{max} = 0$ would simply turn the FVF into an allpass filter. The problem of bias error is also inherent in both PMF and MFT filters, as will be shown. The advantage of FVF is that the bias can be controlled.

The sample seismograms were chosen to illustrate and contrast the above filters, and should not be considered as "typical" events for processing. The seismograms were generated by earthquake sources, and no attempt was made to remove the spectral effects of the source mechanism or the source time function from the events. However, instrument deconvolution was performed.

Event I is a synthetic seismogram recorded at a distance of 1000 kilometers from a 45 degree pure dip-slip source mechanism at a depth of 50 kilometers. The seismogram is composed of vertical component fundamental and first higher mode Rayleigh waves. Figure 1 (top) is the amplitude spectrum of the signal, showing clear spectral contamination of the fundamental mode by the first higher mode at periods less than 20 seconds. The bottom figure is the multiple filter contour map (Dziewonski *et al.* , 1969) giving the distribution of seismic energy as a function of period and group velocity.

For MFT processing, maximum values on the contour map were picked for the fundamental mode, and spectral amplitudes were calculated using equation (4). Group velocities were picked from the maximum amplitude points on the contour map and used as input for PMF and FVF processing.

Figure 2(a) shows the final pseudo-autocorrelation functions for PMF and FVF processing. A cosine window with a one-sided width of 22 seconds was required to exclude the higher mode in the PMF, and this width was also used for processing bias estimates in FVF. Notice that the width of the FVF pseudo-autocorrelation function appears to be slightly wider than the PMF in Figure 2(a). Figure 12 shows the actual window width as a function of period. The FVF window changes as a multiple of the period of interest (20), and in this case, no curvature correction (19) was necessary.

Figure 2(b) shows the time domain results of PMF and FVF, respectively. The isolated fundamental mode for each process appears almost identical. Figure 3 is more informative, contrasting the difference between the theoretical fundamental mode and the filtered amplitude spectra for the three processes. The MFT and FVF are almost identical to the theoretical spectrum, while PMF exhibits biasing over the entire spectrum. It is most pronounced at 30 seconds, which corresponds to the region of highest curvature.

Event I is somewhat extreme, in that the presence of the higher mode forces a narrow bandwidth for the PMF window, causing a large bias as predicted by equation (10). In practice, when dealing with smoothly varying amplitude spectra due to shallow depth explosions, higher modes may not be significantly excited, and the PMF can be constructed with time windows exceeding 100 seconds. This was graphically demonstrated in Stevens (1986b). Long period spectral curvature was slight for the event Stevens chose, and there was no apparent long period bias for two-sided window widths varying from 50 to 1000 seconds. This indicates that in that case, PMF was justified for spectral amplitude determination.

To demonstrate the effect of sharply varying curvature on the filters, events II and III, with pronounced spectral nulls due to double-couple source mechanisms, were picked. Both seismograms are actual events recorded on long period WWSSN vertical component seismometers. Event II was recorded at station SHI in Iran, from a source located in the Gulf of Aden, with the signal propagating across the southeastern Arabian Plate.

This seismogram is composed of two superimposed events, the initial earthquake and a stronger event occurring approximately 175 seconds after the original. The multiple filter contour map in Figure 4 separates the superimposed events into two distinct energy bands, which are almost identical in shape, indicating a similar source mechanism and propagation path.

Pseudo-autocorrelation functions for PMF and FVF analysis are given in Figure 5. The windowed results are almost identical, so only the FVF isolated mode is shown in Figure 6. This figure graphically demonstrates the power of matched filters to effectively separate superimposed signals, in addition to improving the signal to noise ratio.

Since there is no theoretical reference spectrum, the filtered amplitude spectra were simply superimposed on each other in Figure 7 for comparison. The most significant difference is in the MFT spectrum, at 9 seconds and between 30-40 seconds. At 9 seconds, the Gaussian filter (29) has approximate half-amplitude values ($e^{-.7}$) at 8 and 10.2 seconds. From Figure 7, it is clear that the spectrum has approximately the same bandwidth as the Gaussian filter at this point, which violates the requirement for a flat amplitude spectrum across the passband in equation (4). This results in the observed low amplitude. Between 30 and 40 seconds, applying Dziewonski's residual dispersion method (case 2) causes the discrepancy in this period range to disappear, indicating that there is enough slope in the group velocity (see Figure 4) to introduce significant phase distortion into MFT amplitude analysis.

The effect of curvature corrections (19) in the FVF can be seen in Figure 12. There is an increase in window width at 9, 12, and 17 seconds, corresponding to the spectral peaks and nulls of Figure 7. It should be noted that the FVF behaves as poorly as the MFT at 9 seconds, if curvature corrections are not incorporated.

Event III was recorded at U.S. west coast station COR, from an earthquake occurring in the Aleutian Islands. The distance between source and receiver is 4005 kilometers, and the propagation path is oceanic, as seen on the MFT group velocity contour plot (Figure 10). The spectral plot in Figure 8 exhibits two distinct nulls in the signal passband, at 18 and 25 seconds. The null at 18 seconds results in a strong, narrowband spectral peak at 17 seconds, shown by the arrow on the spectral plot in Figure 8. This occurs in the period range where the group velocity slope is almost vertical, resulting in a strongly dispersed, sinusoidal time domain signal. This can be seen on the MFT contour map by comparing the energy of the signal at 17 seconds with the corresponding time domain signal on the right.

The event was picked to illustrate how all of the above filtering methods can fail, if the entire passband is considered to be the desired signal. This is demonstrated by the PMF and FVF pseudo-autocorrelation functions in Figure 9. The windowed functions delete a considerable portion of the signal energy, seen to the left of zero-lag on the raw pseudo-autocorrelation function. This energy corresponds to the 17 second peak found in the original spectrum. The reason for the misalignment is due to the initial estimate of group velocities from the MFT. At the 18 second null, there is a zero crossing in the complex spectrum, resulting in an instantaneous phase change of π radians. The group delay at this point should be impulsive, since it is the derivative of the phase with respect to angular frequency (Papoulis, 1962, p. 134), and this should be seen as an impulse in group velocity. However, the Gaussian MFT filter smooths the impulse, causing a distortion of the group delay in the adjacent 17 second peak. As a result, the PMF is constructed incorrectly on the first iteration, with the 17 second energy to the left of zero-lag.

It is possible for the PMF to correct the signal phase, but as seen from Figure 9, this would require the time window to be at least twice as wide as shown, reducing considerably the ability of the filter to distinguish signal from noise. Figure 10 shows the effect of losing the 17 second peak on the isolated PMF and FVF modes, using the given windows.

Figure 11 shows the filtered spectra superimposed on the original spectrum, with the residuals between the two plotted below. Since all three methods lost the 17 second peak, the residual plots start at the 18 second null. The MFT shows the effect of phase distortion on the amplitude spectrum, with the large residual occurring at 20 seconds. This can be confirmed by observing the near vertical slope to the group velocity dispersion in Figure 8. This again points out the necessity for the residual dispersion method in MFT amplitude analysis.

The effect of curvature corrections (19) on the FVF cosine windows can be seen in Figure 12. Maximum widths at 18, 20, and 25 seconds correspond to the peaks and nulls of the spectrum in Figure 8. It would seem that the largest width should correspond to the point of sharpest curvature in the spectrum, at 17 seconds. However, a review of equation (17) shows that the bias estimates are constructed from the Parzen windowed pseudo-autocorrelation function. Examination of Figure 11 again shows that the window would have to be widened considerably to extract this portion of the spectrum.

Conclusion

The method of frequency variable filters (FVF) is a viable alternative to both the MFT and PMF techniques of extracting normal mode amplitudes from propagating multi-mode surface-waves. It has the advantage of explicitly addressing the problem of spectral bias, which is an unavoidable side effect of any type of convolutional smoothing in the frequency domain. FVF will not be successful on all types of surface-wave spectra, as indicated by event III. This particular case illustrates the fundamental tradeoff between frequency and time domain resolution. To successfully extract the 17 second peak, the time windows would have to be so wide that the filters would be essentially allpass. Both MFT and PMF had the same problem with this type of event.

FVF and PMF have an advantage over MFT, in that the results of processing can be seen both in the time and frequency domain. The pseudo-autocorrelation functions can be used as diagnostic tools, and the final isolated mode can be compared to the original seismogram. In addition, phase distortion can have a significant effect on the MFT, requiring application of a phase-matched filter in the form of the residual dispersion method (case 2). Both PMF and FVF remove the phase as an automatic part of processing. For the above reasons, it is recommended that the FVF, and in some cases the PMF, be preferred over the MFT as filters for isolating surface-wave normal mode amplitude spectra.

Acknowledgements

The authors are grateful to Hafidh A. A. Ghalib and Hanan Al-Khatib for bringing the WWSSN seismograms used in this paper to our attention. This work was supported by the AFSC under Contract F19628-85-K-0029.

References

Der, Z. A. (1986). Comments on the paper "Estimation of scalar moments from explosion-generated surface waves" by Jeffry L. Stevens, *Bull. Seism. Soc. Am. 76,* 1822-1824.

Dziewonski, A., S. Bloch, and M. Landisman (1969). A technique for the analysis of transient seismic signals, *Bull. Seism. Soc. Am. 59,* 427-444.

Dziewonski, A., and A. Hales (1972). Numerical analysis of dispersed seismic waves, *in* B. A. Bolt (editor), *Methods of computational physics, vol. 11,* Academic Press, New York, 39-85.

Dziewonski, A., J. Mills, and S. Bloch (1972). Residual dispersion measurement - a new method of surface-wave analysis, *Bull. Seism. Soc. Am. 62,* 129-139.

Harris, F. J. (1978). On the use of windows for harmonic analysis with the discrete Fourier transform, *Proceedings of the IEEE 66,* 51-83.

Herrin, E. and T. Goforth (1977). Phase-matched filters: application to the study of Rayleigh waves, *Bull. Seis. Soc. Am. 67,* 1259-1275.

Herrmann, R. B. (1973). Some aspects of band-pass filtering of surface waves, *Bull. Seism. Soc. Am. 63,* 663-671.

Hwang, H. J. and B. J. Mitchell (1986). Interstation surface wave analysis by frequency-domain Wiener deconvolution and modal isolation, *Bull. Seism. Soc. Am. 76*, 847-864.

Jenkins, Gwilym M., and D. G. Watts (1968). *Spectral Analysis and Its Applications*, Holden Day, San Francisco.

Landisman, M., A. Dziewonski, and Y. Sato (1969). Recent improvements in the analysis of surface wave observations, *Geophys. J. 17*, 369-403.

Papoulis, A. (1962). *The Fourier Integral and its Applications*, McGraw-Hill, New York.

Russell, D R., H. J. Hwang, and R. B. Herrmann (1986). Matched filters vs. time variable filters, Abstract for the AFGL/DARPA Review of Nuclear Test Monitoring Research, U.S. Air Force Academy, Colorado Springs, Colorado, May 6-8 1986.

Stevens, J. L. (1986a). Estimation of scalar moments from explosion-generated surface waves, *Bull. Seism. Soc. Am. 76*, 123-151.

Stevens, J. L. (1986b). Reply to Z. Der's "Comments on the Paper 'Estimation of Scalar Moments from Explosion-Generated Surface Waves'," *Bull. Seism. Soc. Am. 76*, 1825-1829.

Yacoub, N. K. (1983). "Instantaneous Amplitudes": a new method to measure seismic magnitude, *Bull. Seism. Soc. Am. 73*, 1345-1355.

Department of Earth and Atmospheric Sciences
Saint Louis University
P.O. Box 8099, Laclede Station
St. Louis, Missouri 63156

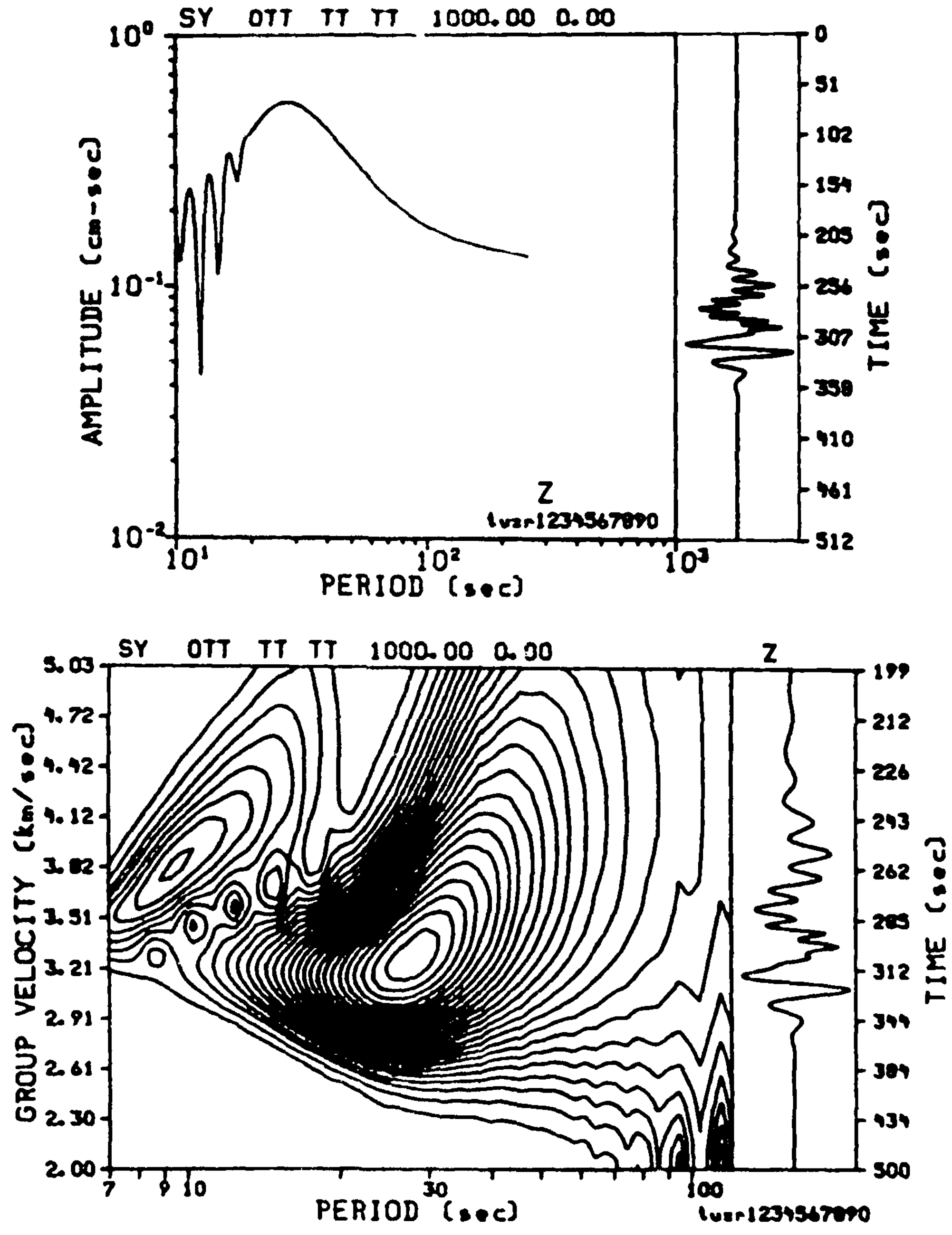

FIG. 1. Event I spectrum (top) and MFT group velocity contour plot (bottom). Time domain seismograms are plotted to the right. Notice the non-linear time scale for the MFT plot.

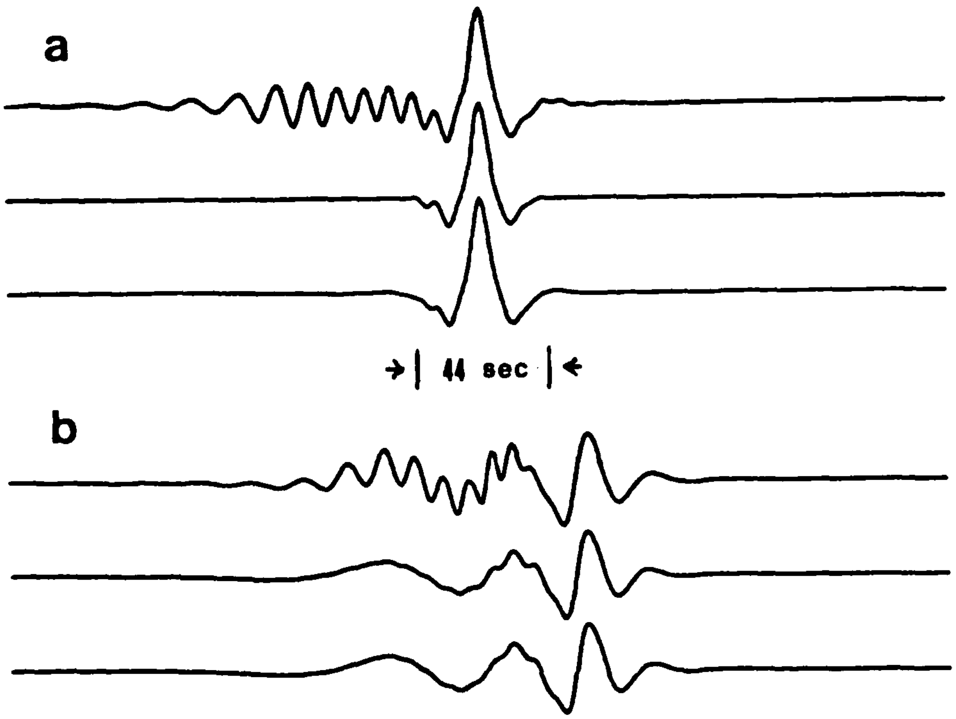

FIG. 2 Event I time-domain functions. a): raw pseudo-autocorrelation function; final pseudo-autocorrelation functions for PMF and FVF, respectively. b): original seismogram; isolated fundamental modes for PMF and FVF, respectively. The time marks indicate the two-sided window width.

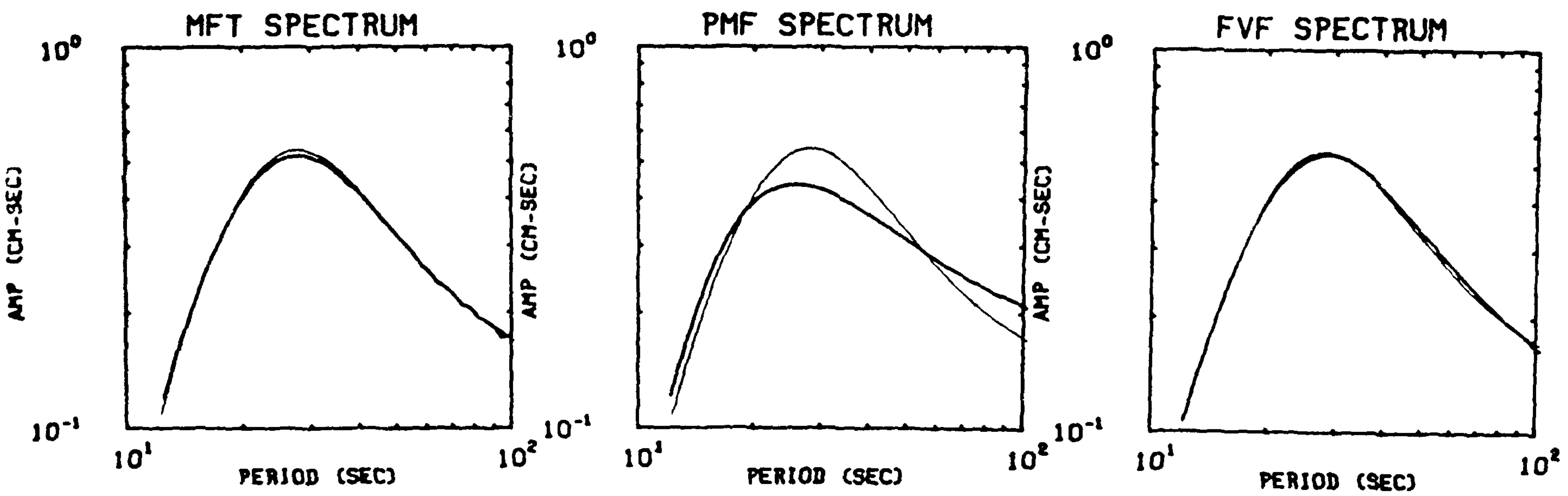

FIG. 3. Comparison of the amplitude spectra for the isolated fundamental modes. HEAVY LINE: filtered fundamental modes. LIGHT LINE: theoretical fundamental mode.

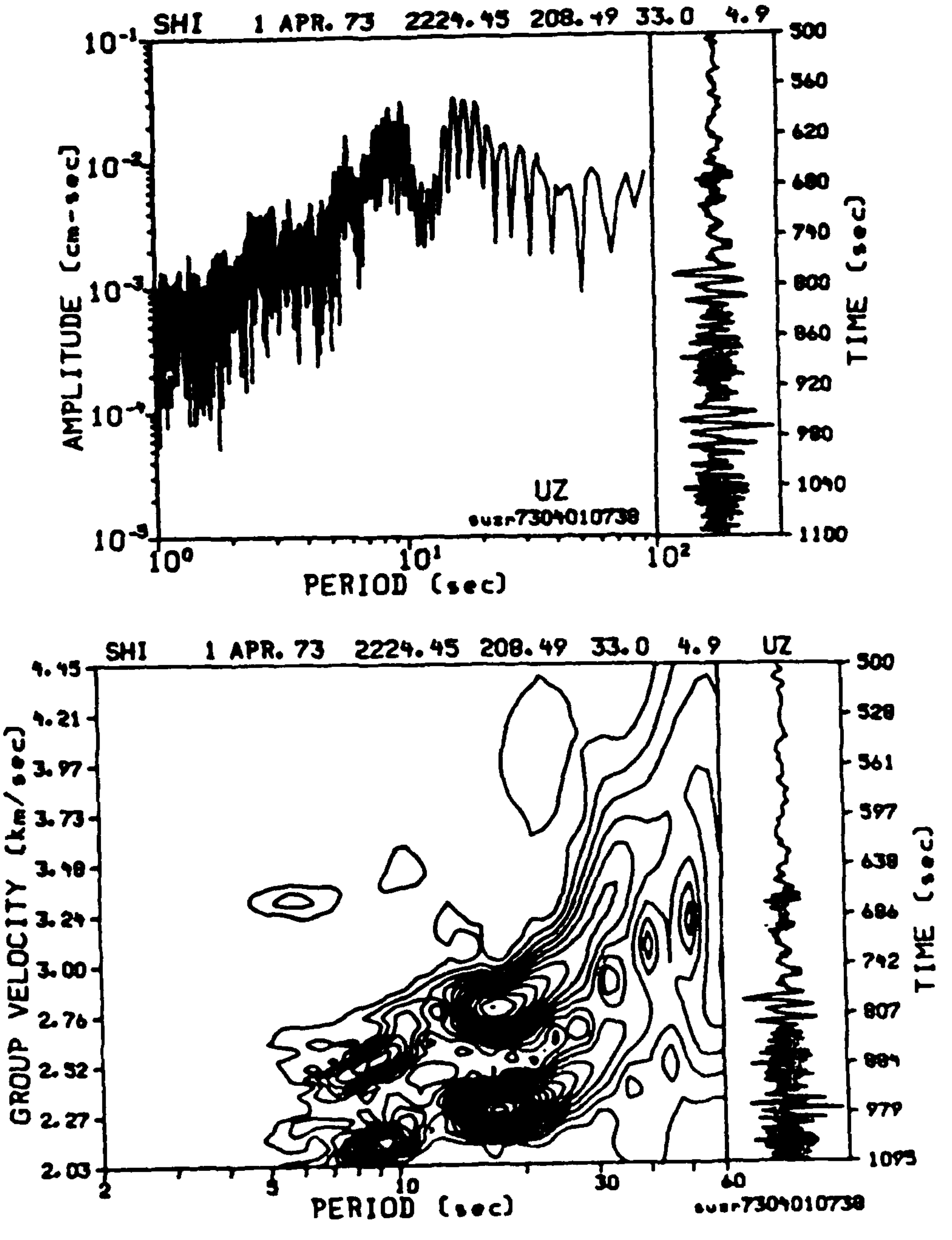

FIG. 4. Event II spectrum (top) and MFT contour plot (bottom). Time domain seismograms are plotted to the right. Notice the non-linear time scale for the MFT plot.

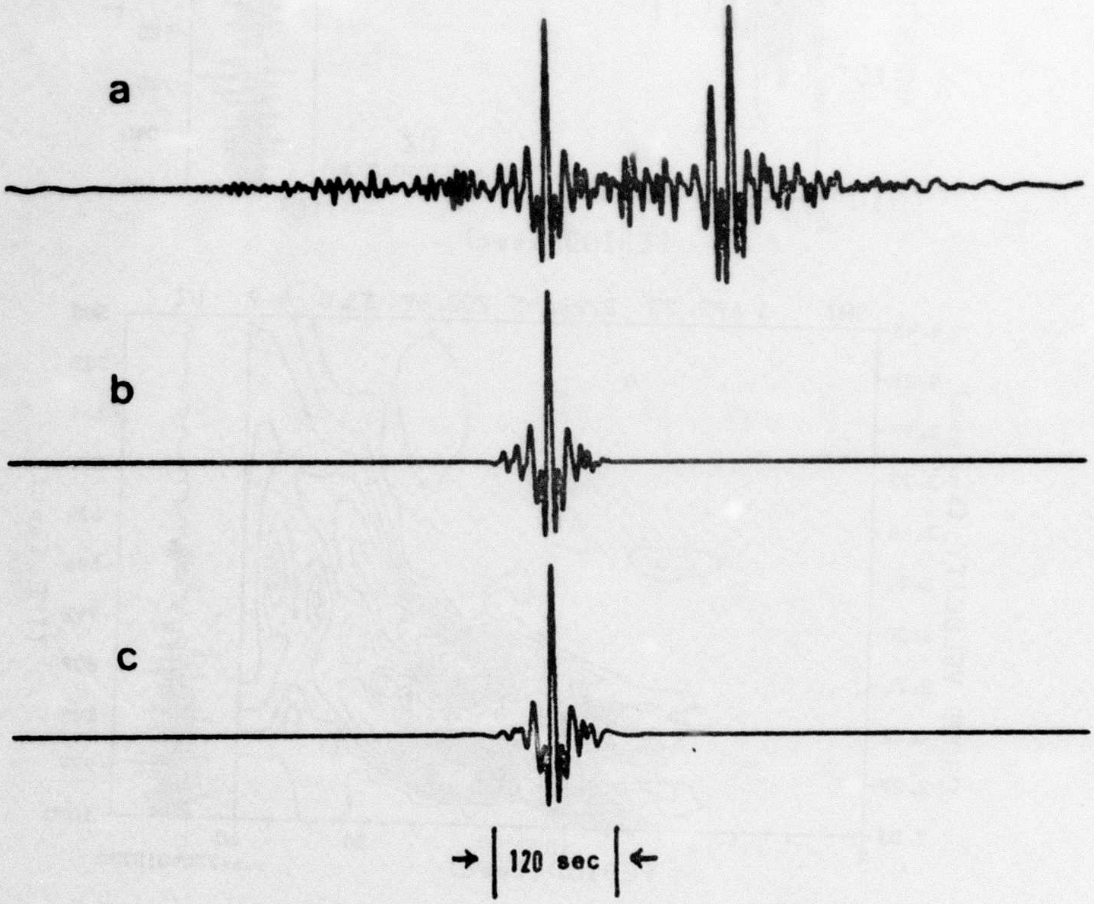

FIG. 5. Event II pseudo-autocorrelation functions. a): raw pseudo-autocorrelation function. b): final pseudo-autocorrelation function for PMF. c): final pseudo-autocorrelation function for FVF. The time marks indicate the two-sided window width.

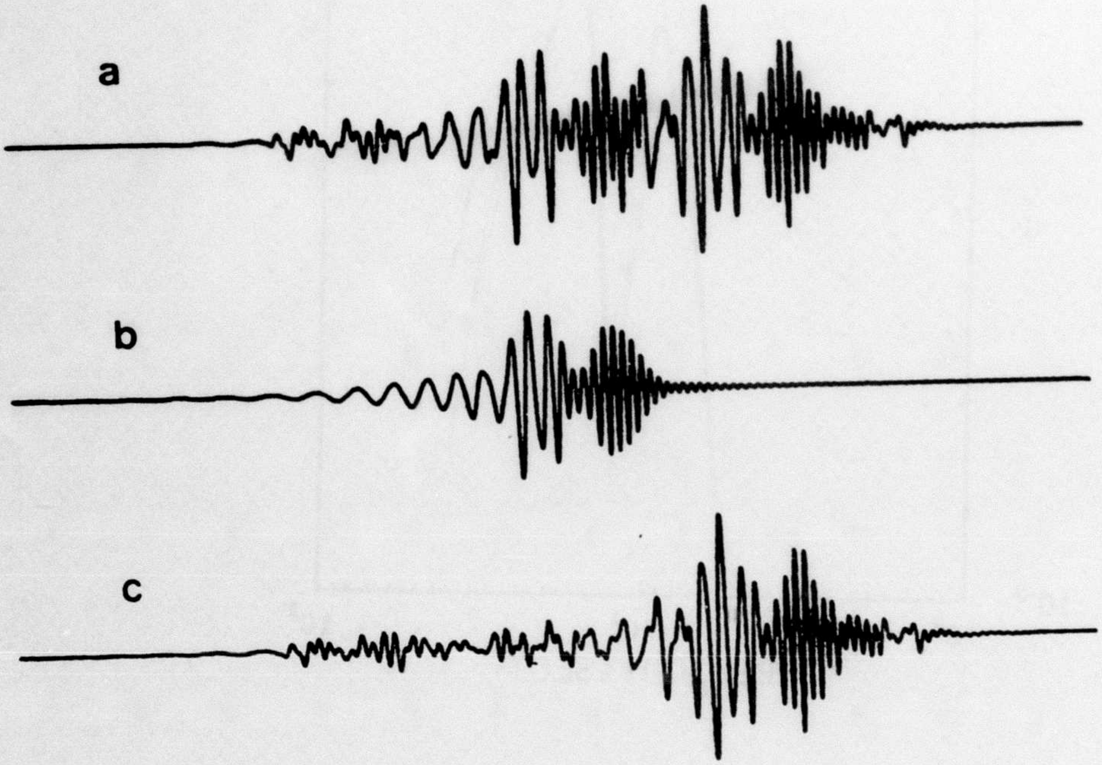

FIG. 6. Event II FVF seismograms. a): raw seismogram. b): fundamental mode isolated by FVF. c): residual obtained by subtracting the fundamental mode from the original seismogram.

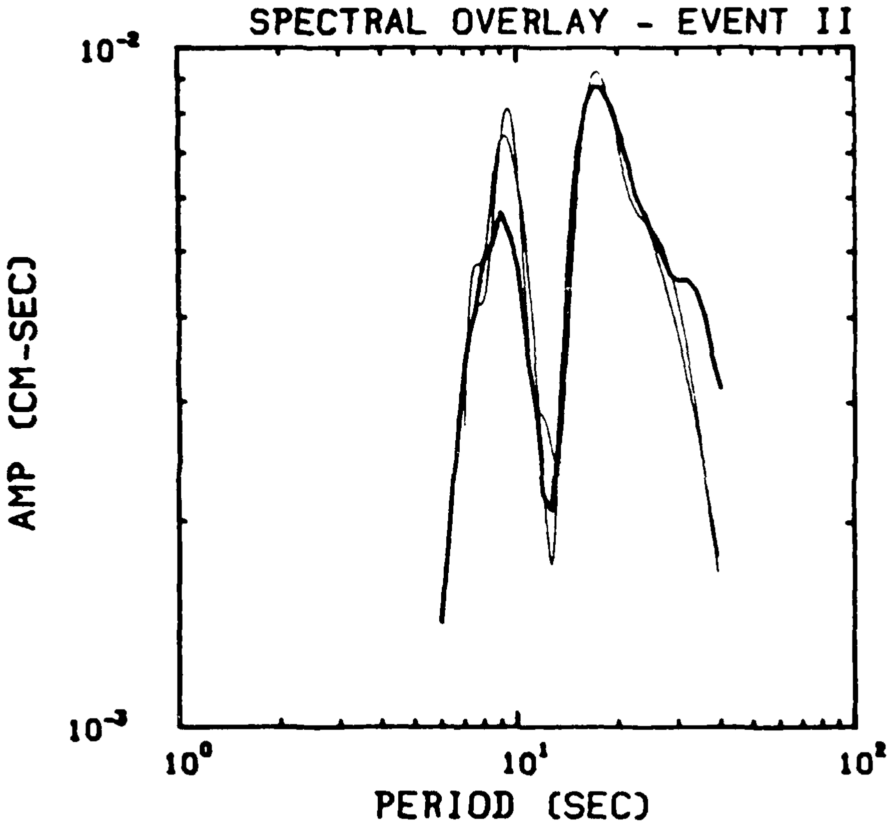

FIG. 7. Event II amplitude spectra for isolated fundamental modes. HEAVY LINE: MFT fundamental mode. LIGHT LINES: PMF and FVF fundamental modes.

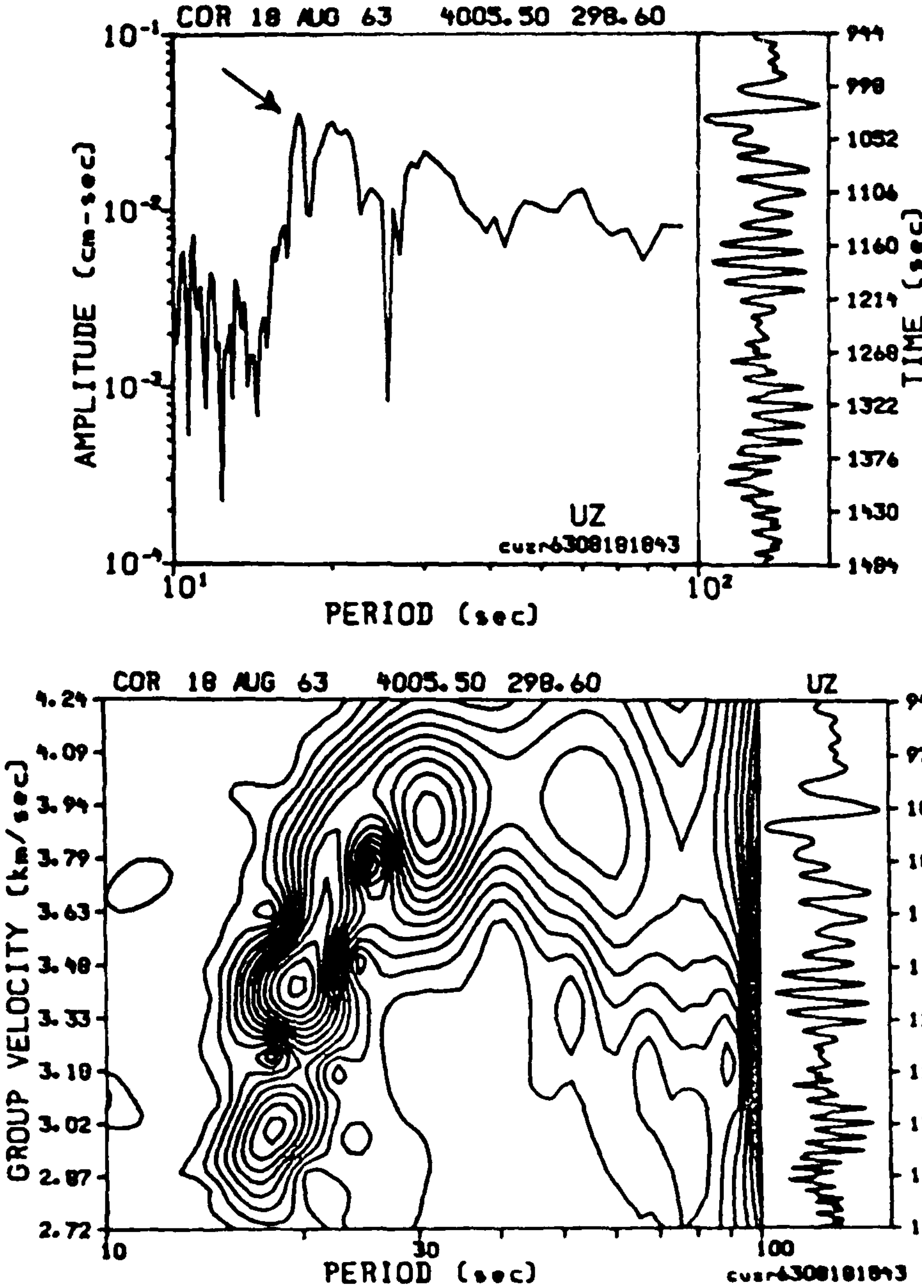

FIG. 8. Event III spectrum (top) and MFT contour plot (bottom). Time domain seismograms are plotted to the right. Notice the non-linear time scale for the MFT plot. The arrow in the upper left corner points out the location of the 17 second spectral peak referred to in the text.

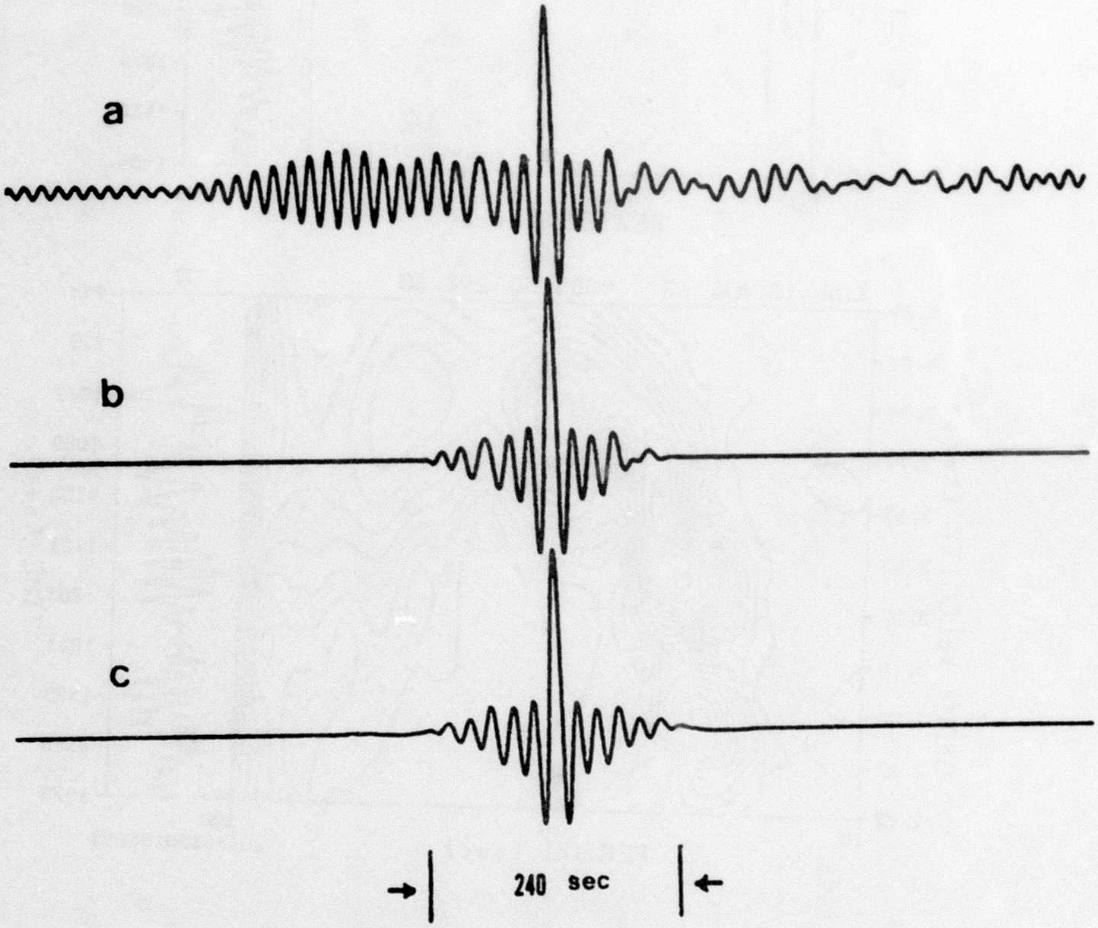

FIG. 9. Event III pseudo-autocorrelation functions. a): raw pseudo-autocorrelation function. b): final pseudo-autocorrelation function for PMF. c): final pseudo-autocorrelation function for FVF. The time marks indicate the two-sided window width.

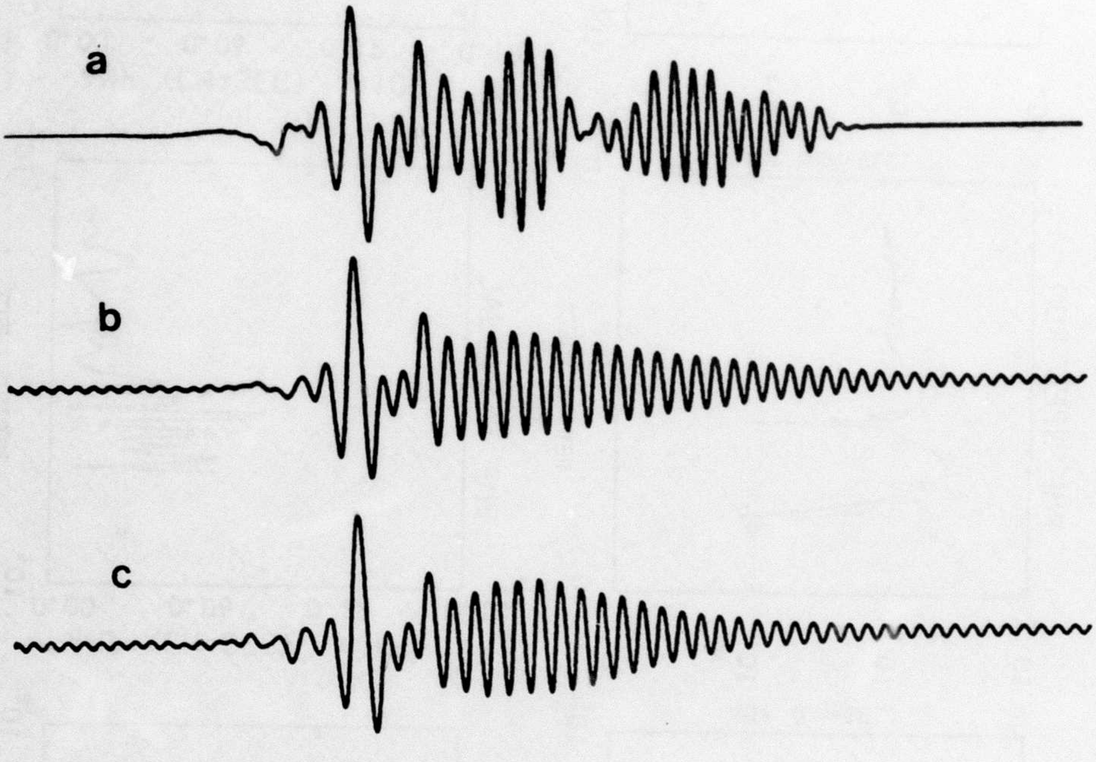

FIG. 10. Event III seismograms. a): raw seismogram. b): fundamental mode isolated by PMF. c): fundamental mode isolated by FVF.

FIG 11. Event III amplitude spectra. TOP: comparison of the original amplitude spectrum with the filtered fundamental modes. LIGHT lines correspond to the original amplitude spectrum, and HEAVY lines are the filtered modes. BOTTOM: residuals between the original spectrum and the filtered modes. Notice that the vertical amplitude scale on these plots is linear.

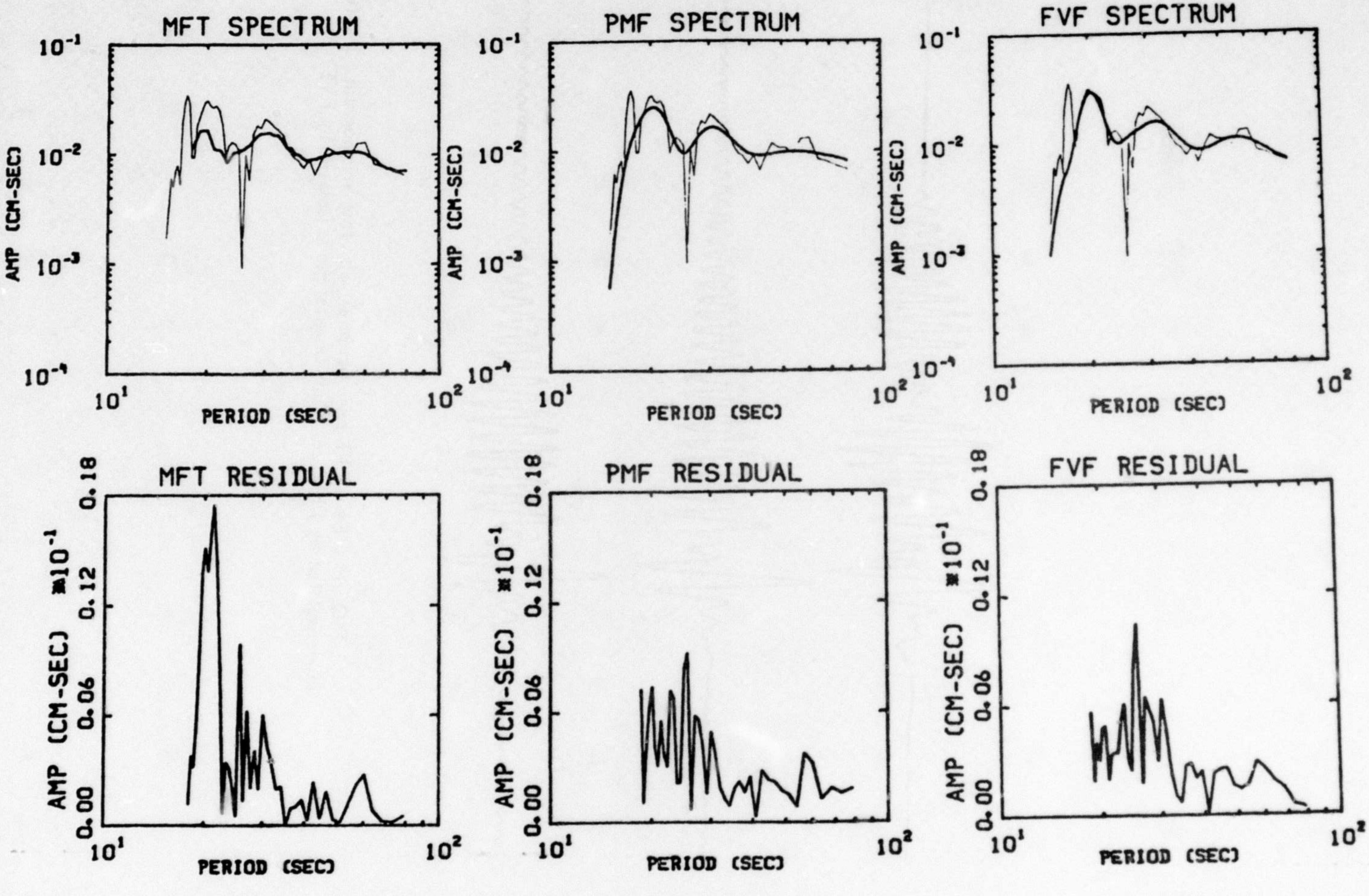

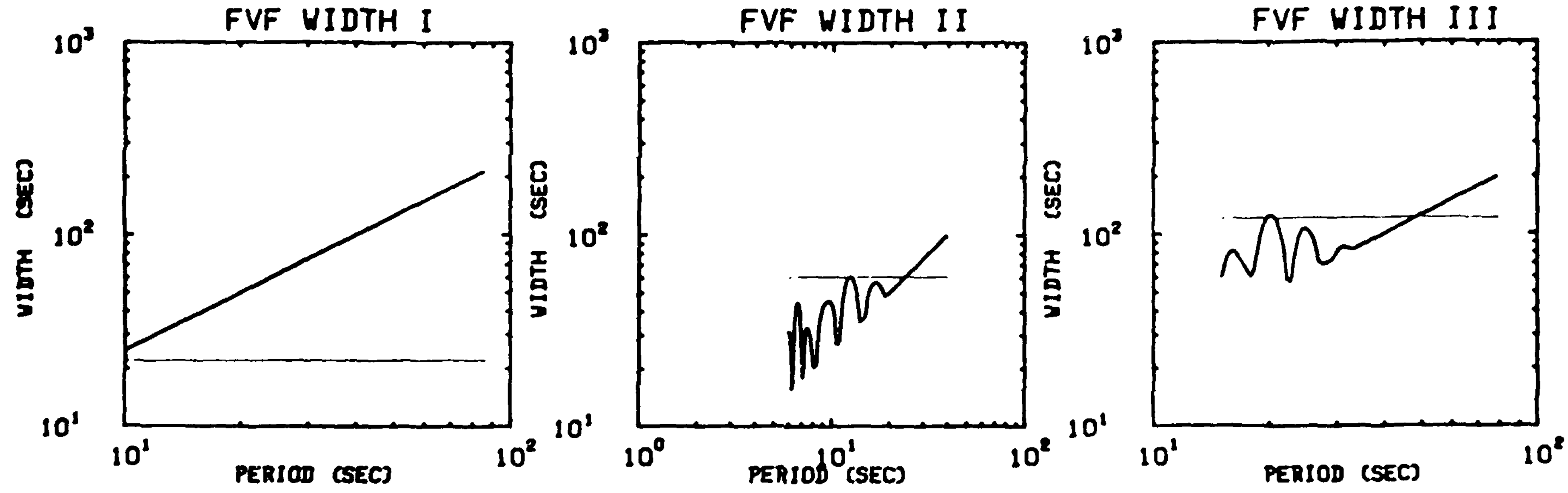

FIG. 12. FVF and PMF one-side cosine window widths calculated for events I, II, and III, respectively. HEAVY line: FVF window width. LIGHT line: PMF window width.

DISTRIBUTION LIST

Dr. Monem Abdel-Gawad
Rockwell Internat'l Science Center
1049 Camino Dos Rios
Thousand Oaks, CA 91360

Professor Keiiti Aki
Center for Earth Sciences
University of Southern California
University Park
Los Angeles, CA 90089-0741

Dr. Raplh Alewine III
DARPA/STO/GSD
1400 Wilson Boulevard
Arlington, CA 22209-2308

Professor Shelton S. Alexander
Geosciences Department
403 Deike Building
The Pennsylvania State University
University Park, PA 16802

Professor Charles B. Archambeau
Cooperative Institute for Resch
in Environmental Sciences
University of Colorado
Boulder, CO 80309

Dr. Thomas C. Bache Jr.
Science Applications Int'l Corp.
10210 Campus Point Drive
San Diego, CA 92121

Dr. Robert Blandford
DARPA/STO/GSD
1400 Wilson Boulevard
Arlington, CA 22209-2308

Dr. Lawrence Braile
Department of Geosciences
Purdue University
West Lafayette, IN 47907

Dr. James Bulau
Rockwell Int'l Science Center
1049 Camino Dos Rios
P.O. Box 1085
Thousand Oaks, CA 91360

Dr. Douglas R. Baumgardt
Signal Analysis & Systems Div.
ENSCO, Inc.
5400 Port Royal Road
Springfield, VA 22151-2388

Dr. G. Blake
US Dept of Energy/DP 331
Forrestal Building
1000 Independence Ave.
Washington, D.C. 20585

Dr. S. Bratt
Science Applications Int'l Corp.
10210 Campus Point Drive
San Diego, CA 92121

Woodward-Clyde Consultants
ATTN: Dr. Lawrence J. Burdick
Dr. Jeff Barker
P.O. Box 93245
Pasadena, CA 91109-3245 (2 copies)

Dr. Roy Burger
1221 Serry Rd.
Schenectady, NY 12309

Professor Robert W. Clayton
Seismological Laboratory/Div. of
Geological & Planetary Sciences
California Institute of Technology
Pasadena, CA 91125

Dr. Vernon F. Cormier/Earth Resources
Lab, Dept of Earth, Atmospheric and
Planetary Sciences
MIT - 42 Carleton Street
Cambridge, MA 02142

Professor Anton W. Dainty
AFGL/LWH
Hanscom AFB, MA 01731

Dr. Zoltan A. Der
ENSCO, Inc.
5400 Port Royal Road
Springfield, VA 22151-2388

Professor Adam Dziewonski
Hoffman Laboratory
Harvard University
20 Oxford St.
Cambridge, MA 02138

Professor John Ebel
Dept of Geology & Geophysics
Boston College
Chestnut Hill, MA 02167

Dr. Jack Evernden
USGS-Earthquake Studies
345 Middlefield Road
Menlo Park, CA 94025

Professor John Ferguson
Center for Lithospheric Studies
The University of Texas at Dallas
P.O. Box 830688
Richardson, TX 75083-0688

Mr. Edward Giller
Pacific Seirra Research Corp.
1401 Wilson Boulevard
Arlington, VA 22209

Dr. Jeffrey W. Given
Sierra Geophysics
11255 Kirkland Way
Kirkland, WA 98033

Professor Steven Grand
Department of Geology
245 Natural History Building
1301 West Green Street
Urbana, IL 61801

Professor Roy Greenfield
Geosciences Department
403 Deike Building
The Pennsylvania State University
University Park, PA 16802

Dr. James Hannon
Lawrence Livermore Nat'l Lab.
P.O. Box 808
Livermore, CA 94550

Professor David G. Harkrider
Seismological Laboratory
Div of Geological & Planetary Sciences
California Institute of Technology
Pasadena, CA 91125

Professor Donald V. Helmberger
Seismological Laboratory
Div of Geological & Planetary Sciences
California Institute of Technology
Pasadena, CA 91125

Professor Eugene Herrin
Institute for the Study of Earth
& Man/Geophysical Laboratory
Southern Methodist University
Dallas, TX 75275

Professor Robert B. Herrmann
Department of Earth & Atmospheric
Sciences
Saint Louis University
Saint Louis, MO 63156

U.S. Arms Control & Disarm. Agency
ATTN: Mrs. M. Hoinkes
Div. of Multilateral Affairs
Room 5499
Washington, D.C. 20451

Professor Lane R. Johnson
Seismographic Station
University of California
Berkeley, CA 94720

Professor Thomas H. Jordan
Department of Earth, Atmospheric
and Planetary Sciences
Mass Institute of Technology
Cambridge, MA 02139

Dr. Alan Kafka
Department of Geology &
Geophysics
Boston College
Chestnut Hill, MA 02167

Ms. Ann Kerr
DARPA/STO/GSD
1400 Wilson Boulevard
Arlington, VA 22209-2308

Professor Charles A. Langston
Geosciences Department
403 Deike Building
The Pennsylvania State University
University Park, PA 16802

Professor Thorne Lay
Department of Geological Sciences
1006 C.C. Little Building
University of Michigan
Ann Harbor, MI 48109-1063

Dr. Arthur Lerner-Lam
Lamont-Doherty Geological Observatory
of Columbia University
Palisades, NY 10964

Dr. George R. Mellman
Sierra Geophysics
11255 Kirkland Way
Kirkland, WA 98033

Professor Brian J. Mitchell
Department of Earth & Atmospheric
Sciences
Saint Louis University
Saint Louis, MO 63156

Professor Thomas V. McEvilly
Seismographic Station
University of California
Berkeley, CA 94720

Dr. Keith L. McLaughlin
Teledyne Geotech
314 Montgomery Street
Alexandria, VA 22314

Mr. Jack Murphy - S-CUBED
Reston Geophysics Office
11800 Sunrise Valley Drive
Suite 1212
Reston, VA 22091

Dr. Carl Newton
Los Alamos National Lab.
P.O. Box 1663
Mail Stop C335, Group E553
Los Alamos, NM 87545

Professor Otto W. Nuttli
Department of Earth &
Atmospheric Sciences
Saint Louis University
Saint Louis, MO 63156

Professor J. A. Orcutt
Geological Sciences Div.
Univ. of California at
San Diego
La Jolla, CA 92093

Dr. Frank F. Pilotte
Director of Geophysics
Headquarters Air Force Technical
Applications Center
Patrick AFB, Florida 32925-6001

Professor Keith Priestley
University of Nevada
Mackay School of Mines
Reno, Nevada 89557

Mr. Jack Raclin
USGS - Geology, Rm 3 C136
Mail Stop 928 National Center
Reston, VA 22092

Professor Paul G. Richards
Lamont-Doherty Geological
 Observatory of Columbia Univ.
Palisades, NY 10964

Dr. Norton Rimer
S-CUBED
A Division of Maxwell Lab
P.O. 1620
La Jolla, CA 92038-1620

Dr. George H. Rothe
Chief, Research Division
Geophysics Directorate
HQ Air Force Technical
 Applications Center
Patrick AFB, Florida 32925-6001

Professor Larry J. Ruff
Department of Geological Sciences
1006 C.C. Little Building
University of Michigan
Ann Arbor, MI 48109-1063

Dr. Alan S. Ryall, Jr.
Center of Seismic Studies
1300 North 17th Street
Suite 1450
Arlington, VA 22209-2308

Professor Charles G. Sammis
Center for Earth Sciences
University of Southern California
University Park
Los Angeles, CA 90089-0741

Dr. David G. Simpson
Lamont-Doherty Geological Observ.
 of Columbia University
Palisades, NY 10964

Dr. Jeffrey L. Stevens
S-CUBED,
A Division of Maxwell Laboratory
P.O. Box 1620
La Jolla, CA 92038-1620

Professor Brian Stump
Institute for the Study of Earth & Man
Geophysical Laboratory
Southern Methodist University
Dallas, TX 75275

Professor Ta-liang Teng
Center for Earth Sciences
University of Southern California
University Park
Los Angeles, CA 90089-0741

Dr. R. B. Tittmann
Rockwell International Science Ctr
1049 Camino Dos Rios
P.O. Box 1085
Thousand Oaks, CA 91360

Professor M. Nafi Toksoz/Earth Resources
Lab - Dept of Earth, Atmospheric and
Planetary Sciences
MIT - 42 Carleton Street
Cambridge, MA 02142

Dr. Lawrence Turnbull
OSWR/NED
Central Intelligence Agency
CIA, Room 5G48
Washington, D.C. 20505

Professor Terry C. Wallace
Department of Geosciences
Building #11
University of Arizona
Tucson, AZ 85721

Professor John H. Woodhouse
Hoffman Laboratory
Harvard University
20 Oxford St.
Cambridge, MA 02138

***

DARPA/PM
1400 Wilson Boulevard
Arlington, VA 22209

Defense Technical
Information Center
Cameron Station
Alexandria, VA 22314
(12 copies)

Defense Intelligence Agency
Directorate for Scientific &
Technical Intelligence
Washington, D.C. 20301

Defense Nuclear Agency/SPSS
ATTN: Dr. Michael Shore
6801 Telegraph Road
Alexandria, VA 22310

AFOSR/NPG
ATTN: Director
Bldg 410, Room C222
Bolling AFB, Wash D.C. 20332

AFTAC/CA (STINFO)
Patrick AFB, FL 32925-6001

U.S. Geological Survey
ATTN: Dr. T. Hanks
Nat'l Earthquake Resch Center
345 Middlefield Road
Menlo Park, CA 94025

SRI International
333 Ravensworth Avenue
Menlo Park, CA 94025

Center for Seismic Studies
ATTN: Dr. C. Romney
1300 North 17th St., Suite 1450
Arlington, VA 22209 (3 copies)

Science Horizons, Inc.
ATTN: Dr. Bernard Minster
Dr. Theodore Cherry
710 Encinitas Blvd., Suite 101
Encinitas, CA 92024 (2 copies)

Dr. G. A. Bollinger
Department of Geological Sciences
Virginia Polytechnical Institute
21044 Derring Hall
Blacksburg, VA 24061

Dr. L. Sykes
Lamont Doherty Geological Observ.
Columbia University
Palisades, NY 10964

Dr. S. W. Smith
Geophysics Program
University of Washington
Seattle, WA 98195

Dr. L. Timothy Long
School of Geophysical Sciences
Georgia Institute of Technology
Atlanta, GA 30332

Dr. N. Biswas
Geophysical Institute
University of Alaska
Fairbanks, AK 99701

Dr. Freeman Gilbert - Institute of
Geophysics & Planetary Physics
Univ. of California at San Diego
P.O. Box 109
La Jolla, CA 92037

Dr. Pradeep Talwani
Department of Geological Sciences
University of South Carolina
Columbia, SC 29208

Dr. Donald Forsyth
Dept. of Geological Sciences
Brown University
Providence, RI 02912

Dr. Jack Oliver
Department of Geology
Cornell University
Ithaca, NY 14850

Dr. Muawia Barazangi
Geological Sciences
Cornell University
Ithaca, NY 14853

Rondout Associates
ATTN: Dr. George Sutton,
Dr. Jerry Carter, Dr. Paul Pomeroy
P.O. Box 224
Stone Ridge, NY 12484 (3 copies)

Dr. Bob Smith
Department of Geophysics
University of Utah
1400 East 2nd South
Salt Lake City, UT 84112

Dr. Anthony Gangi
Texas A&M University
Department of Geophysics
College Station, TX 77843

Dr. Gregory B. Young
ENSCO, Inc.
5400 Port Royal Road
Springfield, CA 22151

Weidlinger Associates
ATTN: Dr. Gregory Wojcik
620 Hansen Way, Suite 100
Palo Alto, CA 94304

Dr. Leon Knopoff
University of California
Institute of Geophysics
& Planetary Physics
Los Angeles, CA 90024

Dr. Kenneth H. Olsen
Los Alamos Scientific Lab.
Post Office Box 1663
Los Alamos, NM 87545

Professor Jon F. Claerbout
Professor Amos Nur
Dept. of Geophysics
Stanford University
Stanford, CA 94305 (2 copies)

Dr. Robert Burridge
Schlumberger-Doll Resch Ctr.
Old Quarry Road
Ridgefield, CT 06877

Dr. Robert Phinney/Dr. F.A. Dahlen
Dept of Geological
Geophysical Sci. University
Princeton University
Princeton, NJ 08540 (2 copies)

New England Research, Inc.
ATTN: Dr. Randolph Martin III
P.O. Box 857
Norwich, VT 05055

Sandia National Laboratory
ATTN: Dr. H. B. Durham
Albuquerque, NM 87185

AFGL/XO
Hanscom AFB, MA 01731-5000

AFGL/LW
Hanscom AFB, MA 01731-5000

AFGL/SULL
Research Library
Hanscom AFB, MA 01731-5000 (2 copies)

Secretary of the Air Force (SAFRD)
Washington, DC 20330

Office of the Secretary Defense
DDR & E
Washington, DC 20330

HQ DNA
ATTN: Technical Library
Washington, DC 20305

Director, Technical Information
DARPA
1400 Wilson Blvd.
Arlington, VA 22209

Los Alamos Scientific Laboratory
ATTN: Report Library
Post Office Box 1663
Los Alamos, NM 87544

Dr. Thomas Weaver
Los Alamos Scientific Laboratory
Los Almos, NM 97544

Dr. Gary McCartor
Mission Research Corp.
735 State Street
P.O. Drawer 719
Santa Barbara, CA 93102

Dr. Al Florence
SRI International
333 Ravenwood Avenue
Menlo Park, CA 94025-3493

Dr. W. H. K. Lee
USGS
Office of Earthquakes, Volcanoes,
& Engineering
Branch of Seismology
345 Middlefield Rd
Menlo Park, CA 94025

***

Dr. Peter Basham/Earth Physics Branch
Department of Energy and Mines
1 Observatory Crescent
Ottawa, Ontario
CANADA K1A 0Y3

Dr. Eduard Berg
Institute of Geophysics
University of Hawaii
Honolulu, HI 96822

Dr. Michel Bouchon - Universite
Scientifique et Medicale de Grenob
Lab de Geophysique - Interne et
Tectonophysique - I.R.I.G.M-B.P.
38402 St. Martin D'Heres
Cedex FRANCE

Dr. Hilmar Bungum/NTNF/NORSAR
P.O. Box 51
Norwegian Council of Science,
Industry and Research, NORSAR
N-2007 Kjeller, NORWAY

Dr. Kin-Yip Chun
Geophysics Division
Physics Department
University of Toronto
Ontario, CANADA M5S 1A7

Dr. Alan Douglas
Ministry of Defense
Blacknest, Brimpton,
Reading RG7-4RS
UNITED KINGDOM

Professor Peter Harjes
Institute for Geophysik
Rhur University/Bochum
P.O. Box 102148, 4630 Bochum 1
FEDERAL REPUBLIC OF GERMANY

Dr. E. Husebye
NTNF/NORSAR
P.O. Box 51
N-2007 Kjeller, NORWAY

Mr. Peter Marshall, Procurement
Executive, Ministry of Defense
Blacknest, Brimpton,
Reading FG7-4RS
UNITED KINGDOM

Dr. B. Massinon
Societe Radiomana
27, Rue Claude Bernard
75005, Paris, FRANCE

Dr. Pierre Mechler
Societe Radiomana
27, Rue Claude Bernard
75005, Paris, FRANCE

Dr. Ben Menaheim
Weizman Institute of Science
Rehovot, ISRAEL 951729

Dr. Svein Mykkeltveit
NTNF/NORSAR
P.O. Box 51
N-2007 Kjeller, NORWAY

Dr. Frode Ringdal
NTNF/NORSAR
P.O. Box 51
N-2007 Kjeller, NORWAY

University of Hawaii
Institute of Geophysics
ATTN: Dr. Daniel Walker
Honolulu, HI 96822

***